

Advanced Duplex Coatings for Wear and Corrosion Resistance

by

Saddam Hossain

A thesis submitted in partial fulfillment of the requirements for the degree of

Master of Science

Department of Mechanical Engineering
University of Alberta

© Saddam Hossain, 2023

Abstract

Tribocorrosion, a synergistic impact of wear and corrosion, impacts the lifespan of machine parts in most sectors. Consequently, duplex coating has emerged as the most promising solution to address tribocorrosion. In this work, advanced noble duplex coating systems of TiAlN/WC-NiBSi/steel and TiAlN/TiC-SS/steel were developed by utilizing PVD/PTA techniques to combat the simultaneous impact of wear and corrosion. The coatings were used to assess the mechanical, wear, corrosion, and tribocorrosion properties. Indentation and scratch tests were used to investigate mechanical properties, and wear properties were investigated using a ball-on-flat tribo-system with an alumina ball. The corrosion behavior of the various coatings' architecture was studied using a three-electrode cell system, and tribocorrosion characteristics were tested by immersing the ball-on-flat tribo-system in 3.5 wt.% NaCl electrolyte. SEM and EDS analysis were done to investigate the microstructure and surface morphology of the coatings.

From indentation test results, the hardness was improved in the order of steel < TiC-SS/steel < WC-NiBSi/steel < TiAlN/TiC-SS/steel < TiAlN/steel < TiAlN/WC-NiBSi/steel. Scratch test results revealed an early disintegration of the TiAlN layer due to the brittle character of the TiAlN layer, whereas the harder intermediate layer of TiC-SS/steel and WC-NiBSi/steel coating improved the crack resistance of TiAlN.

Single-thick TiC-SS or WC-NiBSi coatings revealed good wear resistance after dry sliding testing, with the WC-NiBSi/Steel coating system exhibiting the best tribological behavior due to its high load-bearing capacity. However, the addition of a TiAlN layer didn't improve the wear resistance. This may be due to the reduced adhesion of TiAlN, the high surface roughness of thick coatings, or the brittle nature of the nitride. Nevertheless, the wear performance improved for the duplex

coatings compared to the single TiAlN coating due to the higher load-bearing capacity of the hard intermediate layer.

The TiC-SS/Steel system showed the highest corrosion resistance without serious dissolution of stainless-steel matrix and TiC; while thick WC-NiBSi/steel and thin TiAlN/steel coating showed poor corrosion behavior due to surface defects which attracted the electrolyte to infiltrate through the pores. Moreover, the addition of TiAlN on the TiC-SS/Steel coatings system did not improve corrosion since oxidation occurred on the surface of the top TiAlN layer. However, when TiAlN was added to the WC-NiBSi/Steel coating, the top TiAlN layer sealed the pores, greatly improving the corrosion performance.

From the tribocorrosion studies at OCP, TiAlN/steel and WC-NiBSi/steel coatings showed poor corrosion resistance due to the defects on the surface. The TiAlN/steel coating surface showed rupture, fractures, and layer breakdown as mechanical wear initiated the cracks, and chloride ions exacerbated the surface cracking. TiC-SS/steel coating showed excellent tribocorrosion resistance while adding a TiAlN cannot help further. However, the addition of the TiAlN layer improved the tribocorrosion performance of WC-NiBSi/steel coating at OCP. At potentiostatic polarization, all the coatings demonstrated more pronounced material deterioration than wear, corrosion, or tribocorrosion at OCP due to the applied external potential. The duplex coating of TiAlN/WC-NiBSi/steel experienced a significant material loss due to the galvanic coupling between TiAlN and WC-NiBSi.

Overall, the TiC-SS/steel system offers superior corrosion and tribocorrosion resistance due to the hard TiC, and corrosion resistance of stainless steel, while the WC-NiBSi/steel system provides

excellent wear resistance due to the wear-resistant nature of WC hard particles. Duplex coating of TiAlN/WC-NiBSi/steel showed good tribocorrosion resistance at OCP conditions.

Acknowledgments

Firstly, I would like to praise the almighty Allah for his blessings upon me and my family.

I would like to express my sincere gratitude to my supervisors Dr. Andre McDonald and Dr. Jolanta-Ewa Sapielha for their outstanding guidance and continuous support throughout my research. Having the opportunity to work at both the University of Alberta and Polytechnic Montreal, I learned immensely from the research groups under Dr. McDonald and Dr. Jolanta. I would also like to thank InnoTech Alberta for their support for PTA technology.

I am grateful to my colleagues, especially Adekunle Ogunbadejo for always being courteous and helpful, Dr. Rakesh Nair for his guidance and support, Dr. Luis Bernardo Varela Jimenez for assisting me with everything in this research, Dr. Pedro Renato Tavares Avila for PVD deposition, and Dr. Marwan Azzi for assisting with tribocorrosion investigations.

Finally, I would like to express my gratitude to my family for their support and motivation throughout my studies.

Contents

Acknowledgments.....	v
List of Tables	ix
List of Figures.....	x
Glossary of Symbols.....	xv
List of Abbreviations	xviii
1 Introduction	1
1.1 General Background.....	1
1.2 Motivation	4
1.3 Objectives	6
1.4 Thesis Organization.....	6
2 Literature Review	8
2.1 Duplex Coatings	8
2.2 Materials for Duplex Coatings	10
2.3 Wear.....	15
2.4 Corrosion	17
2.5 Tribocorrosion	20
3 Experimental Method	21
3.1 Coating Fabrication Techniques.....	21
3.1.1 Plasma Transferred Arc (PTA).....	21
3.1.2 Physical Vapor Deposition (PVD).....	22
3.1.3 Duplex Coating.....	23
3.2 Fabrication of Duplex Coatings.....	24

3.2.1	TiC-SS and WC-NiBSi Coatings using PTA.....	24
3.2.2	TiAlN Coating using PVD.....	25
3.3	Surface Characterization.....	27
3.4	Mechanical Properties Analysis	28
3.4.1	Hardness Tests	28
3.4.2	Scratch Tests	29
3.5	Tribological and Tribocorrosion Analysis.....	30
3.5.1	Tribological Characteristics	30
3.5.1.1	Assessment of Tribological Properties	32
3.5.2	Corrosion.....	33
3.5.2.1	Assessment of Corrosion Properties	35
3.5.3	Tribocorrosion.....	39
3.5.3.1	Assessment of Tribocorrosion Properties	40
4	Results and Discussions.....	43
4.1	Microstructure of the Deposited Coating Systems	43
4.2	Mechanical Characterization	45
4.2.1	Mechanical Properties	45
4.2.2	Adhesion Strength of TiAlN Coating.....	47
4.3	Tribological Testing	51
4.3.1	Coefficient of Friction.....	51
4.3.2	Wear Rate.....	58
4.4	Corrosion	63
4.4.1	Open Circuit Potential (OCP).....	63

4.4.2	Electrochemical Impedance Spectroscopy (EIS).....	65
4.4.3	Potentiodynamic Polarization.....	68
4.5	Tribocorrosion.....	71
4.5.1	Wear at OCP.....	71
4.5.2	Potensionstatic Wear.....	75
4.6	Degradation Mechanism.....	82
4.6.1	During Dry Sliding.....	82
4.6.2	During Corrosion.....	86
4.6.3	During Tribocorrosion.....	88
5	Conclusions.....	95
6	Future Works and Recommendations.....	99
7	References.....	100
	Appendix A – SEM Images and EDS analysis of Coatings.....	117
	Appendix B – Wear, corrosion, and tribocorrosion behavior.....	118

List of Tables

Table 1: Deposition parameters for WC-NiBSi and TiC-SS coatings by PTA.	24
Table 2: Critical load values for the single layer TiAlN coating and duplex TiAlN/TiC-SS/steel and TiAlN/WC-NiBSi/steel coatings after scratch test of varying load from 0 to 30 N.	48
Table 3: Wear rate of PTA and PVD deposited single and duplex coatings obtained after dry sliding tests using 5N load and 4.75 mm diameter alumina counterpart.	60
Table 4: Wear rate of PTA and PVD deposited single and duplex coatings obtained after dry sliding tests: 2N load, 4.75 mm diameter alumina counterpart.	61
Table 5: Corrosion properties obtained from electrochemical impedance spectroscopy (EIS) Nyquist plots results.....	67
Table 6: Corrosion current and corrosion potential from potentiodynamic polarization curve...	69

List of Figures

Fig. 1. General schematic of duplex coatings system.....	4
Fig. 2. Duplex coatings system showing CrN and CoCrMo(C) S-phase layers [8].	14
Fig. 3. Schematic of wear mechanisms [47].	17
Fig. 4. Schematic of different types of corrosion [53].	19
Fig. 5. Schematic diagram for tribocorrosion [55].	20
Fig. 6. Schematic of PTA coating [60].	22
Fig. 7. PVD sputtering process [65].	23
Fig. 8. Experimental set-up for PVD deposition.	26
Fig. 9. Schematic representation of the coating's architecture with (a) TiAlN/Ti/Steel, (b) TiC-SS /Steel, (c) WC-NiBSi/Steel, and duplex coatings (d) TiAlN/Ti/TiC-SS/Steel (e) TiAlN/Ti/ WC-NiBSi/Steel.	27
Fig. 10. Illustration of wear tests under dry sliding conditions [69].	31
Fig. 11. Typical wear profile after wear tests [70].	31
Fig. 12. Experimental set-up for corrosion experiments under 3.5 wt.% NaCl.	34
Fig. 13. The open circuit potential (OCP) [73].	35
Fig. 14. Nyquist plot for an electrochemical system [47].	37

Fig. 15. Illustration of Tafel plot [73].....	38
Fig. 16. (a) Tribocorrosion system where sliding contact immersed in NaCl aqueous solution and (b) position of the immersed sample at the end of the tribocorrosion tests.	40
Fig. 17. The sequence of operations for tribocorrosion tests with OCP evolution [75].	42
Fig. 18. SEM images on the surfaces of single and duplex coatings on steel: a) TiC-SS/steel coating by PTA, b) WC-NiBSi/steel coating by PTA, c) TiAlN/steel coating by PVD, d) TiAlN/TiC-SS/steel coating by PVD/PTA, and e) TiAlN/WC-NiBSi/steel coating by PVD/PTA.	44
Fig. 19. Hardness, H, and reduced modulus of elasticity, E^* for the substrate and coatings.....	46
Fig. 20. Elastic strain to failure, H/E^* , and Resistance to plastic deformation, H^3/E^{*2} , for the substrate and coatings.	46
Fig. 21. SEM micrographs (a) for the scratch track of steel, TiC-SS/steel, WC-NiBSi/steel, TiAlN/steel, TiAlN/TiC-SS/steel, and TiAlN/WC-NiBSi/steel after the scratch tests and (b) represents the higher magnified images toward the end of the track with the EDS analysis.	50
Fig. 22. Coefficient of friction as a function of sliding cycles from the dry sliding tests at 5N load against alumina ball for bare steel, a single layer of TiAlN and TiC- and WC-based coatings, and their duplex coatings systems on steel under different sliding cycles of (a) 1000 cycles/s, (b) 2000 cycles/s, and (c) 4000 cycles/s.	53

Fig. 23. Optical microscopy images for TiAlN/steel, TiAlN/TiC-SS/steel (partial and full removal of TiAlN top layer), and TiAlN/WC-NiBSi/steel coatings architecture after reciprocating sliding wear experiments at 5N and 1000 cycles (20m of total sliding distance). 54

Fig. 24. Optical microscopy images for TiAlN/steel, TiAlN/TiC-SS/steel, and TiAlN/WC-NiBSi/steel coatings after reciprocating sliding wear experiments at 5N and 2000 cycles (40m of total sliding distance). 55

Fig. 25. Optical microscopy images for TiAlN/steel, TiAlN/TiC-SS/steel, and TiAlN/WC-NiBSi/steel coatings after reciprocating sliding wear experiments at 5N and 4000 cycles (80m of total sliding distance). 55

Fig. 26. Coefficient of friction as a function of sliding cycles from the dry sliding tests at 2N load against alumina ball for bare steel, single layer of TiAlN/steel, TiC-SS/steel, WC-NiBSi/steel, TiAlN/TiC-SS/steel, and TiAlN/WC-NiBSi/steel duplex coatings systems under different sliding cycles of (a) 1000 cycles/s, (b) 2000 cycles/s, and (c) 4000 cycles/s. 57

Fig. 27. Wear rates of the fabricated coatings and the steel substrate as a reference, under 5N load. 61

Fig. 28. Wear rates of the fabricated coatings and the substrate as reference under 2N load. 62

Fig. 29. Volume loss during sliding wear for 5N load. 62

Fig. 30. Volume loss during sliding wear for 2N load. 63

Fig. 31. The evolution of OCP during corrosion test. 65

Fig. 32. Nyquist plots for bare steel, single layer coatings, and duplex coatings.....	67
Fig. 33. Potentiodynamic polarization curve for bare steel and single layer, and duplex coatings.	70
Fig. 34. OCP measurements during tribocorrosion tests at 2N, 2000 cycles/s.....	72
Fig. 35. Coefficient of friction obtained during tribocorrosion tests at OCP for 2N, 2000 cycles/s.	73
Fig. 36. Wear rates of different coatings during tribocorrosion tests at OCP for 2N, 2000 cycles/s.	74
Fig. 37. OCP measurements during tribocorrosion tests under potentiostatic polarization at 2N, 2000 cycles/s.....	75
Fig. 38. Corrosion current measurements after the tribocorrosion at potentiostatic polarization for (a) steel, TiC-SS/steel coating, WC-NiBSi/coating, TiAlN/steel coating, TiAlN/TiC-SS/steel duplex coating, and TiAlN/WC-NiBSi/steel duplex coatings and (b) zoomed-in image for TiC- SS/steel coating and TiAlN/TiC-SS/steel duplex coating with 2N, 2000 cycles/s load and 0.2V external applied potential.....	79
Fig. 39. Coefficient of friction obtained during tribocorrosion tests at potentiostatic polarization.	80
Fig. 40. Wear rate during tribocorrosion tests under potentiostatic polarization for 2N load for 2000 cycles and 3.5 wt.% NaCl solution.....	81

Fig. 41. Worn surfaces of (a) steel, (b) TiC-SS/steel coating, (c) WC-NiBSi/steel coating, (d) TiAlN/steel coating, (e) TiAlN/TiC-SS/steel duplex coating, and (f) TiAlN/WC-NiBSi/steel duplex coating under reciprocating sliding motion of 2N and 2000 cycles/s against alumina ball.
 85

Fig. 42. SEM micrographs for corrosion behaviour of different single-layer and duplex coatings under 3.5 wt.% NaCl solution: (a) steel, (b) TiC-SS/steel coating, (c) WC-NiBSi/steel coating, (d) TiAlN/steel coating, (e) TiAlN/TiC-SS/steel duplex coating, and (f) TiAlN/WC-NiBSi/steel duplex coating. 88

Fig. 43. SEM micrographs for tribocorrosion under OCP conditions at 2N, 2000 cycles load, and 3.5 wt.% NaCl: (a) steel, (b) TiC-SS/steel coating, (c) WC-NiBSi/steel coating, (d) TiAlN/steel coating, (e) TiAlN/TiC-SS/steel duplex coating, and (f) TiAlN/WC-NiBSi/steel duplex coating.
 91

Fig. 44. SEM micrographs for tribocorrosion under potentiostatic polarization at 2N, 2000 cycles load, and 3.5 wt.% NaCl: (a) steel, (b) TiC-SS/steel coating, (c) WC-NiBSi/steel coating, (d) TiAlN/steel coating, (e) TiAlN/TiC-SS/steel duplex coating, and (f) TiAlN/WC-NiBSi/steel coating. 94

Fig. A1. SEM micrographs for (a) steel, (b) TiC-SS/steel coatings, and (c) WC-NiBSi/steel coating under dry sliding tests at 2N and 1000 sliding cycles. 117

Fig. B1. Line profile from profilometer for showing positive wear depth or positive volume region for steel under the dry sliding wear tests conditions against alumina at 5 N load and 1000 sliding cycles. 118

Glossary of Symbols

H	Hardness [GPa]
E	Elastic Modulus [GPa]
S	Stiffness [Pa]
A	Area [m ²]
K	wear rate [mm ³ N ⁻¹ m ⁻¹]
F	Normal Force [N]
P	Load [N]
V	Volume [mm ³]
s	sliding distance [m]
E	Potential [V]
I	Current [A]
R	Resistance [Ω]

C	Capacitance [F/cm ²]
W	Warbug Impedence [Ω cm ²]
Z	Impedance [Ω]
t	Time [s]

Greek symbols

μ	Coefficient of Friction
Ω	Resistance [Ohm]
Δ	Delta
ω	Radial frequency [rad/s]
φ	Phase shift [Degrees]
η	Overpotential [V]
β	Tafel constant

Subscripts

upper upper bound

* Reduced

lower lower bound

s solution

p polarization

corr Corrosion

t Tangential

a Anodic

c Cathodic

max Maximum

List of Abbreviations

PTA	Plasma Transferred Arc
PVD	Physical Vapor Deposition
HiPIMS	High-Power Impulse Magnetron Sputtering
RF	Radio Frequency
pDC	Pulsed Direct Current
MMC	Metal Matrix Composite
WE	Working Electrode
SCE	Standard Calomel Electrode
CE	Counter Electrode
OCP	Open Circuit Potential
EIS	Electrochemical Impedance Spectroscopy
FESEM	Field Emission Scanning Electron Microscopy
EDS	Energy Dispersive X-Ray Spectroscopy

1 Introduction

1.1 General Background

Typically, the performance of engineering materials is reduced due to materials degradation, leading to the early breakdown of components. Material deterioration such as wear, corrosion, and tribocorrosion can have a substantial economic impact on sectors that rely on equipment and machinery. The overall efficiency of production in the industries decreases, and the total cost of corrosion rises which is equivalent to 3 or 4% of the gross national product (GNP) [1].

Wear occurs whenever two solid objects are in motion relative to one another and is directly related to the nature of their contact. Wear is the removal of material from a surface caused by mechanical action such as friction or abrasion [1]. Corrosion, on the other hand, is the process by which a material deteriorates because of its contact with its surroundings. This interaction is fundamentally chemical and electrochemical, and it takes place between a solid surface and its surrounding environment [1]. Tribocorrosion is a synergistic interaction of these two processes that occur when mechanical wear and chemical corrosion combine [2]. Importantly, the combined effect of wear and corrosion can cause more detrimental effects on steel. Even though most of the mechanical components are made of steel, they cannot serve their purpose properly to resist the simultaneous effect of wear and corrosion under very severe conditions. For example, in oil and gas industries, both wear and corrosion properties must be considered while transporting solid-liquid mixtures because of their exposure to chloride (Cl^-) environment in addition to abrasive wear [3]. Once a metal part is damaged by corrosion or wear, there is an urgent issue to replace the part, and this

replacement needs to be done regularly if no protective measures are taken. The replacement increases the total cost and decreases the overall efficiency of production in the industries.

Degradation of materials, such as wear and corrosion, usually occurs at the component's surface. Consequently, the degradation of the material may be avoided by shielding the surface of the component from its potentially destructive surroundings. This is something that can be accomplished by engineering the surface of the component. The engineered surface may attain desirable surface features above the essential characteristics, which might enhance the materials from being deteriorated [4].

Recently, protective coatings have been utilized by many researchers to improve the surface properties of a component [5,6]. The duplex coatings system normally has two layers: a thick hard layer that acts as a barrier towards the applied load, and a top layer that resists the outside environment. Although the top layer guards against chemical corrosion, the thick layer provides mechanical support and acts as a bond layer. **Fig. 1.** illustrates the general schematic of the duplex coating system. Duplex coatings, as opposed to conventional coatings, can offer better tribocorrosion protection. When compared to single-layer coatings, duplex coatings give higher corrosion protection. The combination of two layers forms a barrier that prevents corrosive materials from accessing the underlying substrate. Duplex coatings also improve the underlying material's adhesive strength. When the combined effect of wear and corrosion is evaluated, it exhibits improved performance [7,8].

Due to the unique features of duplex coatings, deploying these advanced duplex systems can alleviate the tribocorrosion problem in the oil and gas industries. The duplex coatings system can

also be used in other industries such as automotive, aerospace, marine, and others that include wear, corrosion, or tribocorrosion processes. Due to the superior mechanical, wear, and corrosion resistance features of duplex coating, it helps to extend the life of the material, decrease maintenance costs, and increase durability.

In this study, a noble duplex coating system has been designed to mitigate tribocorrosion under aggressive environments. Because of the superior hardness and load-bearing capacity, TiC-SS and WC-NiBSi were chosen as the thick layer. TiAlN was chosen for the topcoat due to its high hardness and excellent corrosion resistance when interacting with the outside environment. TiC-SS and WC-NiBSi metal matrix composites (MMCs) coatings were fabricated using plasma transferred arc (PTA) coating technology, while the top TiAlN layer was deposited by sputtering using physical vapour deposition (PVD). The wear, corrosion, and tribocorrosion properties of a single PTA layer on low carbon steel and duplex coatings PVD coating deposited on PTA were evaluated. The mechanical properties such as hardness and modulus of elasticity were evaluated. Mechanical characteristics are assessed and correlated to the performance and behaviour of materials under a variety of tribological and tribocorrosion conditions. The performance of any system can be optimized for any specific application by understanding the mechanical qualities and making the right material choices.

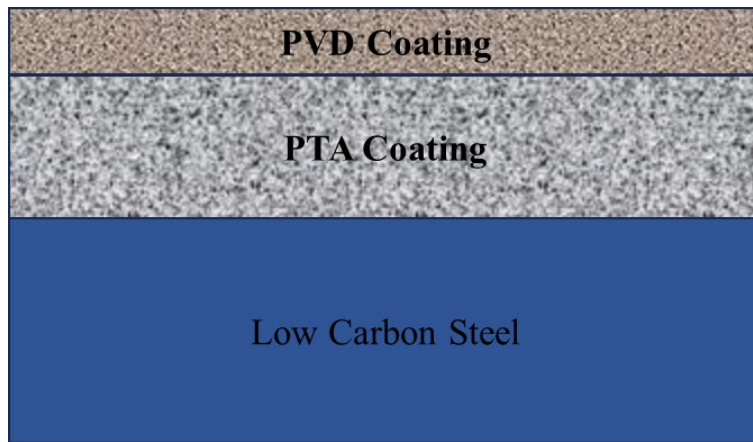


Fig. 1. General schematic of duplex coatings system.

1.2 Motivation

As mentioned in the preceding section, wear, corrosion, and tribocorrosion can have a significant economic impact on sectors including automotive, aerospace, and biomedical engineering that depend on equipment and machinery, leading to equipment failure, delays, and maintenance costs. In particular, tribocorrosion may pose a serious problem when machinery is subjected to corrosive environments in addition to mechanical wear. Pipelines, valves, and pumps, as well as waste incinerators, mining machinery, and medical implants, can all experience a reduction in life due to tribocorrosion [9].

Tribocorrosion involves complicated interactions between tribological and electrochemical mechanisms that are not yet fully understood. The study of duplex coatings for tribocorrosion mitigation can bring new insights into the underlying processes involved in the synergistic interactions of wear and corrosion.

Coatings made from hard-faced materials provide high hardness and a low coefficient of friction. Diamond-like carbon (DLC), for instance, exhibits high hardness but low corrosion resistance. High hardness, excellent wear resistance, and corrosion resistance are all features of ceramic materials. Ceramic materials, however, might have great hardness but limited toughness. On the other hand, composite coatings can incorporate both toughness and hardness qualities. Hardness and toughness might be balanced, for instance, by inserting tough TiC particles within a softer stainless-steel matrix. These days, nanoparticles are used to enhance the mechanical, tribological, and corrosion properties of materials.

Duplex coatings can minimise the need for replacement components by enhancing the durability and lifetime of materials, contributing to a more sustainable and environmentally responsible approach to manufacturing and engineering. These coatings can improve the lifespan of components and minimize maintenance costs by enhancing the wear and corrosion resistance of materials. Single-layer coatings may not have all the qualities necessary to counteract the combined effect of wear and corrosion. It may be wear-resistant but not corrosion-resistant, or vice versa. Duplex coatings, on the other hand, can provide effective protection against tribocorrosion. The properties of the duplex coatings can be engineered by employing both layers.

Overall, this research on duplex coatings for wear, corrosion, and tribocorrosion resistance has the potential to significantly contribute to scientific knowledge as well as practical applications in a variety of sectors, with considerable economic, environmental, and societal advantages.

1.3 Objectives

The objectives of this study on duplex coatings for the mitigation of wear, corrosion, and tribocorrosion are as follows:

1. Develop an optimized duplex coating system for wear, corrosion, and tribocorrosion protection for oil and gas industries.
2. Investigate the effectiveness of TiAlN/TiC-SS/steel and TiAlN/WC-NiBSi/steel duplex coatings fabricated by PVD/PTA techniques in improving wear, corrosion, and tribocorrosion resistance.
3. Evaluate the performance of duplex coatings under applied sliding load and aqueous solution of sodium chloride conditions.
4. Investigate the microstructure and mechanical properties of the duplex coatings and establish a correlation between the properties and the coating's performance.

1.4 Thesis Organization

Chapter 1, The "Introduction" chapter provides a summary of the research conducted in this study. This chapter also provides the motivation (why it is being done, what problems exist in the selected sectors, and how to address them) and objectives of this study.

Chapter 2, The "Literature Review" chapter includes a brief overview of wear, corrosion, and tribocorrosion. This chapter describes materials used to create protective coatings using various coating manufacturing procedures. Duplex coatings system is introduced as well. The chapter

focuses on the gaps in this research and suggests ways to address them in order to enhance tribocorrosion characteristics.

Chapter 3, The “Experimental Method” section describes the detailed fabrication method of duplex coatings by plasma transferred arc (PTA) and physical vapor deposition (PVD) method. The analysis of microstructure and mechanical properties is also explained. The procedures of tribological, electrochemical, and tribocorrosion tests are also presented.

Chapter 4, The "Results and Discussions" section discusses the experimental findings for all work done on the characterization of the duplex coatings' structural and mechanical characteristics, as well as their tribological, electrochemical, and tribocorrosion behaviour. At the end of this chapter, a detailed explanation of the deterioration mechanism throughout each experiment of corrosion, wear, and tribocorrosion using SEM micrographs and EDS analysis is provided.

Chapter 5, The section "Conclusions and Suggestions for Future Work" provides the key conclusions and new results from experiments in this study.

Chapter 6, The section "Future Works and Recommendations" gives suggestions and recommendations for future work and how to improve corrosion, wear, and tribocorrosion resistance by choosing suitable materials in future studies.

2 Literature Review

Tribocorrosion is a complex process caused by the simultaneous action of wear and corrosion. The combined effect of these two processes can cause materials to deteriorate quickly in a wide range of engineering applications. Duplex coatings, which combine a hard coating with a corrosion-resistant coating, have been studied as a potential solution to the tribocorrosion problem [8,10]. In this literature review, we will review the current state of research on duplex coatings for tribocorrosion.

2.1 Duplex Coatings

By integrating various materials, coatings can give special properties that would not be achievable when utilizing such materials in bulk form, and as a result, offer improved mechanical, tribological, corrosion, and tribocorrosion characteristics. Using a range of materials, the fabrication of coatings can be possible in a number of shapes and architectures. Coatings may be single layer, bilayer or duplex layer, or multi-layers (more than two layers). In terms of the coatings' microstructure, it can be anything from a straightforward, homogenous single structure to more intricate systems including alloyed, composite, and gradient structures. Duplex coatings are among the most appealing coating design ideas since they provide a greater opportunity to tailor surface properties [11].

During the fabrication process of thick coatings by plasma spray, PTA, high velocity Oxygen fuel (HVOF), or different spray processes, imperfections could appear. Due to some porosity in the coatings, direct infiltration of the electrolyte through the flaws may result in the formation of a galvanic cell between the coating and the substrate, which results in more harmful damage than

corrosion on a bare substrate [12]. Pores are a typical feature in spray or fused coatings. For example, F. Pougoum et al. [13] reported that the surface degradation of Fe₃Al-based HVOF coatings was caused by crack development and propagation via the imperfections on the surface. W.-M. Zhao et al. [14] investigated the corrosion mechanism of NiCrBSi coatings deposited by HVOF and found that the corrosion started around defects like pores, inclusions, and microcracks in the NiCrBSi coating and followed paths formed by pores, microcracks, and the lamellar structure, leading to exfoliation or laminar peeling off. These flaws allow liquid electrolytes to penetrate the coatings. To limit the material degradation process, various approaches have been taken for example by sealing the pores or adding a top layer [7,14].

In recent years, extensive studies have been conducted on duplex coatings for wear, corrosion, and tribocorrosion [15–17]. For example, F. Pougoum et al. [13] investigated the sliding wear behaviour of Fe₃Al-based duplex coatings deposited by PVD and HVOF methods to protect stainless steel against alumina balls. The duplex coating, also known as thin-on-thick coating, the system was designed with the HVOF interlayer supporting the applied load and the top PVD diamond like carbon, DLC layer interacting with the hostile outside environment. They then demonstrated that the addition of CrN or DLC top layers considerably improved the wear resistance of the SS304 substrate and the HVOF/SS304 systems. This enhanced performance was due to the outstanding tribological and friction characteristics of these PVD top layers, as well as the improved interlayer hardness, demonstrating the greater load-bearing capability of the thick and hard HVOF interlayer that helps to avoid localized plastic deformations of the substrate when the surface of the top thin film is subjected to repeated conditions of loading and unloading during sliding wear experiments. In another study, F. Pougoum et al. [7] examined the corrosion and tribo-

corrosion performance of HVOF Fe₃Al coatings with CrN and DLC PVD topcoats in NaCl aqueous solution using electrochemical impedance spectroscopy (EIS) method. The synergistic effect of corrosion and wear was investigated and the influence of topcoats on the interlayer in this synergy was discussed. They reported that the HVOF Fe₃Al layer had poor corrosion and tribocorrosion resistance due to the existence of defects that enable the electrolyte to infiltrate into the coating. The duplex coating, on the other hand, demonstrated good corrosion resistance by establishing a protective barrier against the corrosive chloride solution; as a result, the DLC and CrN films improved the pitting resistance of the underlying coating.

2.2 Materials for Duplex Coatings

Typically, steel is used to make the components in industries. Amongst all types of steels, stainless steel (SS) is popular because of its excellent corrosion resistance as a passive oxide layer, especially Cr-oxide is formed naturally on the surface and is responsible to have excellent corrosion properties [18,19]. Nevertheless, stainless steels suffer from pitting, a severe form of localized corrosion. In addition, stainless steels may only be used in applications absent from tribological processes due to their generally poor hardness and wear resistance [20,21]. Consequently, engineered coatings have been developed to achieve all the material attributes for applications where severe wear, corrosion, and tribocorrosion are involved. As previously stated, duplex coatings are commonly employed because they exhibit more resilience than individual coatings. The architecture of duplex coating consists of a thick interlayer to withstand the applied load and a corrosion resistant thin layer to interact with the outside harsh environment [13].

2.2.1 Thick Intermediate Coatings

Numerous materials have been chosen by different groups of researchers for making duplex coatings for the mitigation of material degradation [22,23]. Ceramics materials are extensively used to make coatings for mechanical, wear, corrosion, and tribocorrosion properties compared to metals [24]. TiC has great surface hardness, strong corrosion resistance, low friction coefficient, and high electrical conductivity. Due to its great chemical and thermal stability, TiC coatings are widely employed as wear-resistant materials in a variety of applications [25]. The corrosion and tribological properties of the metal matrix composite can be improved by adding ceramic particles. M. Yasir et al. [26] doped Al₂O₃ particles to enhance the tribological characteristics of coatings and demonstrated that the composite coating had better hardness and a lower friction coefficient than the coating without any inclusion when subjected to tribological environments. They reported that as the inclusion of the second phase may significantly improve the tribological performances of the coatings, the presence of hard Al₂O₃ particles may be related to the superior qualities of the composite coatings. Another study [27] explained that the inclusion of hard ceramic particles greatly enhances the tribological behaviour of Fe-based amorphous coatings due to the greater hardness and potential lubricating effect of the additives.

Titanium carbide (TiC), out of all ceramic materials, has been recognized as a promising reinforcing phase to increase the mechanical characteristics of the matrix due to its superior mechanical, chemical, and thermal properties [28]. Chen et al. [29] reported that Fe-Al intermetallic reinforced with TiC exhibits good wear resistance against dry sliding. Najmeh et al [28] studied corrosion behaviour of TiC incorporated Fe₃Al matrix prepared by high-velocity oxy-fuel spraying and showed that the incorporation of TiC particles increases the corrosion resistance

of composite coating in NaCl solution. Rokanopoulou and Papadimitriou [30] investigated the microstructure and tribological properties of TiC incorporated SS matrix and found that MMCs exhibited improved wear rate and friction coefficient which is attributed to the higher hardness by the addition of hard TiC particles. Similar studies were done by other researchers where they used TiC as reinforcing particles to improve the microstructure and wear properties [31,32].

Tungsten carbide (WC) has been used as a prominent hard material in many industrial applications due to its outstanding wear-resistant qualities, high hardness, and low coefficient of thermal expansion. The primary drawbacks of WC are its low heat of production, which allows it to be quickly dissolved by molten metals, and its brittleness, which frequently restricts its applicability in specific applications [3]. Several attempts have been made to improve the toughness of WC by including ductile elements such as Ni-based and Co-based alloys [33,34]. Nickel and nickel-based coatings are of interest to many researchers for improving plasticity, fracture toughness, and corrosion resistance [35]. Particularly, NiBSi and NiCrBSi are considered the binding materials with the tungsten carbide [36–38]. Boron is added to the matrix to lower the melting temperature of the metal and increase the coating's hardness due to the formation of a hard Ni₃B phase. The hardness is also slightly increased when Si is added. Cr is further added to improve the corrosion and wear resistance. However, the wear resistance of NiCrBSi-WC cannot be improved compared with NiBSi-WC coatings. In one study, P. Niranatlumpong and H. Koiprasert [37] investigated the microstructure of the NiCrBSi-WC and NiBSi-WC coatings deposited by electric arc spraying and studied the sliding wear behaviour of the coatings. Although the microhardness of NiBSi-WC is lower than that of NiCrBSi-WC coatings, the wear resistance is higher for NiBSi-WC coatings due to more dissolution of WC/W₂C into the matrix in NiBSi-WC that results in good metallurgical

bonding between the matrix and carbide. The larger frequency of craters from WC/W₂C detachments caused NiCrBSi-WC coatings to demonstrate reduced wear resistance. The dissolution of W has a significant impact on the microstructure and wear behaviour of NiCrBSi-WC and NiBSi-WC coatings which is reported by P. Sheppard and H. Koiprasert [38]. They observed that because NiBSi contained more W than NiCrBSi, it had less thermal expansion mismatch, resulting in less thermal stress throughout the coating production process. Thermal stress in coatings can induce intergranular fractures, which can spread throughout the coating. More carbides separated from the NiCrBSi coatings during the dry sliding test, however, less carbides detached during the three-body abrasion. NiBSi, on the other hand, consistently provides greater performance.

2.2.2 Thin Top Coatings

Choosing the proper materials for the topcoat is critical since it will interact with the outside environment. Among the materials used for the topcoat, diamond-like carbon (DLC) is of much interest because of its excellent tribological properties. However, delamination of DLC film may result from the high stresses of the coating and high modulus of elasticity compared to the substrate [39]. Nitride films produced by PVD have received the most attention among possible materials for the top layer in terms of their ability to resist corrosion in chloride-containing solutions because of their high hardness, outstanding tribological characteristics, and good corrosion properties [7]. For instance, titanium nitride (TiN) has excellent corrosion resistance in most conditions because of its stability in aqueous solutions. Azzi et al. [40] utilized the PVD technique to produce TiN hard coatings for corrosion studies and showed improved corrosion properties. The ability of TiN

to resist corrosion, however, differs depending on the substrate and deposition conditions. AlN, on the other hand, is gaining much interest from many researchers because it is thermally stable and chemically inert. The exceptional properties of these two binary coatings have attracted the attention of researchers to study ternary titanium-aluminum nitride (TiAlN) coatings since it is a potential candidate for tribological and corrosion applications [12,41]. Finally, **Fig. 2.** shows an example of duplex coatings with the thin top CrN coating and thick intermediate CoCrMo(C) S-phase coating.

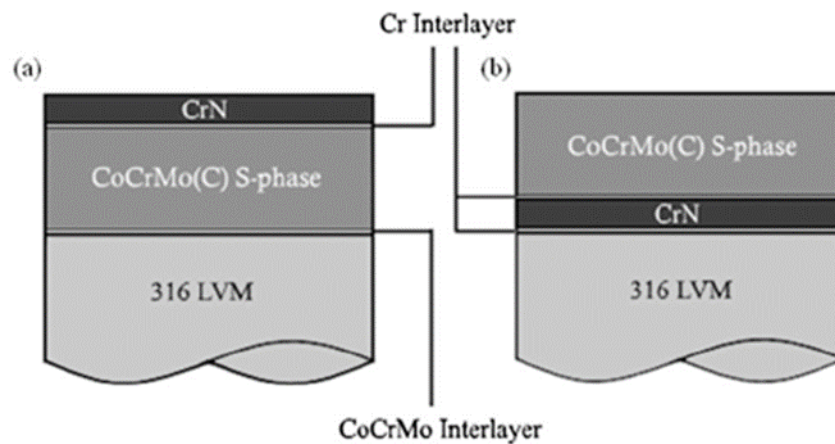


Fig. 2. Duplex coatings system showing CrN and CoCrMo(C) S-phase layers [8].

Among all the materials discussed in the literature, TiC-stainless steel (SS), WC-NiBSi composites, and TiAlN were chosen. To create duplex coatings, the composite materials were deposited on steel using the plasma transferred arc (PTA) method, and TiAlN was deposited as the top layer using the physical vapour deposition (PVD) method.

2.3 Wear

Wear refers to the gradual removal of material from a solid surface as a result of mechanical action or other physical processes. It can occur due to a variety of factors such as abrasion, adhesion, erosion, or corrosion. Wear can lead to a reduction in the functional performance or lifespan of the affected component and can also result in the generation of debris or particles that can cause further damage or contamination in the surrounding environment. Wear is a common phenomenon in many engineering and industrial applications, and understanding and controlling wear behavior is important for optimizing performance, minimizing maintenance costs, and ensuring safety and reliability. The following are the different types of wear and **Fig. 3.** shows the wear mechanisms of different types of wear.

- **Abrasive wear:** Abrasive wear occurs when hard particles or protuberances are pressed against and moving over a solid surface. The hard particles cause severe degradation of material by micro-cutting, micro-fracture, pull-out of individual grains accelerated fatigue by repeated deformations. The severity of abrasive wear in any system is determined by the size, shape, and hardness of the abrasive particle, the magnitude of the stress applied by the particle, and the frequency of contact of the abrasive particle [42].
- **Erosive wear:** Erosion is the mechanical interaction between a solid surface and an impinging liquid or solid particles which causes progressive loss of original material from that surface. The wear mechanisms involved in erosive wear mainly depend on the physical and mechanical characteristics of the erosive particles for instance, particle size, shape, hardness, impact velocity, and impingement angle of the particle to the solid surface [43].

- **Adhesive wear:** A very serious type of wear known as adhesive wear is characterised by high wear rates and a significant unstable friction coefficient. Adhesive wear can quickly destroy sliding contacts, and in extreme situations, very high coefficients of friction or seizures may stop sliding motion. Adhesion causes high coefficients of friction and severe damage to the contacting surfaces [44].
- **Corrosive and Oxidative wear:** These types of wear are primarily caused by chemical reactions between the worn material and a corroding medium, which can be air, a chemical reagent, or a reactive lubricant. While oxidative wear refers to wear brought on by atmospheric oxygen, corrosive wear is a general term for any form of wear involving a chemical or corrosive process [45].
- **Fatigue wear:** Cycling loading during friction causes fatigue wear of a material. When a material is subjected to cyclic loading, it causes progressive and localised structural damage. Fatigue occurs when the applied load exceeds the material's fatigue strength. The term fatigue wear refers to the repeated high local stress contacts between asperities that occur during sliding or rolling. Wear particles are produced by fatigue propagated cracks. The mechanics of crack initiation, crack growth, and fracture determine wear under these circumstances. Compared to unworn surfaces, worn surfaces have extremely high levels of plastic strain [46].

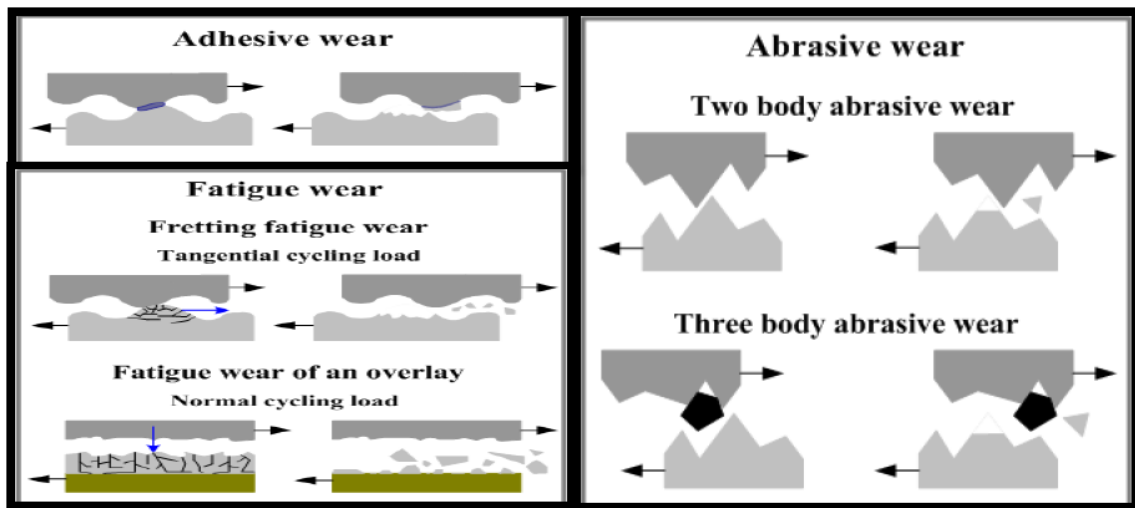


Fig. 3. Schematic of wear mechanisms [47].

2.4 Corrosion

Corrosion is a natural process that involves the deterioration or destruction of a material, usually a metal. While wear is induced by physical processes, corrosion is caused by chemical or electrochemical reactions of a material with its environment. This process can occur due to a variety of factors such as exposure to moisture, oxygen, acids, salts, or other corrosive substances. Corrosion can lead to changes in the physical and chemical properties of the material, including loss of strength, changes in surface finish, and reduction in performance or functionality. Corrosion can occur on any surface, but is particularly common in metals and alloys, and can be accelerated by factors such as high temperature, pressure, or mechanical stress. Corrosion is a significant problem in many industries, including construction, transportation, and manufacturing, and controlling corrosion is important for maintaining the structural integrity and safety of materials and components. Corrosion reactions are mostly electrochemical which involves an anodic

oxidation reaction and a cathodic reduction reaction where electrons are being transported [48]. There are different types of corrosion that a metal can suffer when exposed to corrosive environments. The schematic representation of different types of corrosion is shown in **Fig. 4**.

They are:

- **Uniform corrosion:** The most common type of corrosion is a general or uniform attack. General or uniform corrosion affects the entire surface or over a large area of the material with equivalent intensity by a chemical or electrochemical reaction [49].
- **Pitting corrosion:** Pitting is regarded as one of the most destructive types of corrosion because failure happens so abruptly as it is sometimes challenging to find pits due to their small size and because they are usually covered by corrosion products. Pitting corrosion is a type of localised corrosion that causes the creation of microscopic cavities on the metal's surface. The oxidation reaction in the pit lowers the pH and causes chloride ions to migrate to balance the charge of the metal ions. This generates a more aggressive environment locally and accelerates corrosion, allowing it to penetrate at a rapid rate [50].
- **Galvanic corrosion:** When dissimilar materials come into contact and are exposed to a conducting fluid, galvanic corrosion can occur. Typically, when two dissimilar metals are submerged in a corrosive or conductive solution, a potential difference exists between them. Because of their differing potentials, the more active material corrodes faster [1].
- **Crevice corrosion:** Crevice corrosion is a type of localised corrosion that happens when a metal surface is partially shielded from the environment, such as through small gaps, joints, or deep cracks. Because of the difference in aeration with the bulk environment, anodic reactions occur preferentially in the crevice. Crevice corrosion typically arises from

variations in the concentration of metal ions and oxygen between the crevice and its surroundings [51].

- **Fretting corrosion:** Fretting corrosion occurs at the interface of contacting surfaces with modest relative motion. Fretting damage can erode the oxide layer of passive metals, promoting corrosion [52].

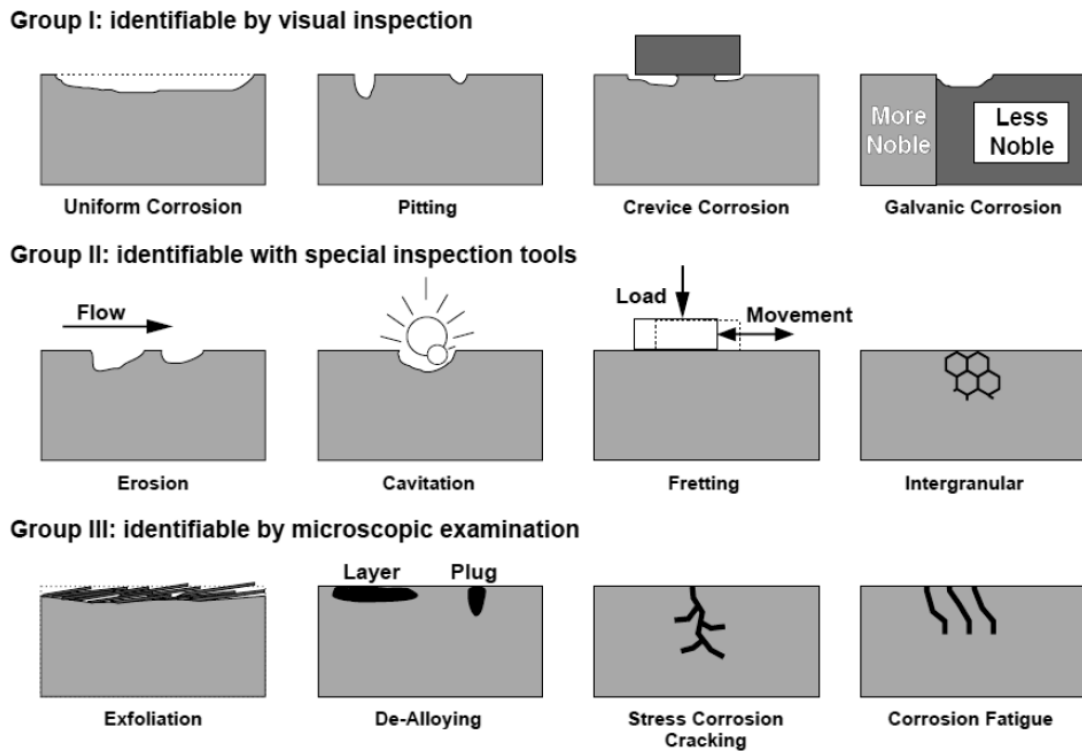


Fig. 4. Schematic of different types of corrosion [53].

2.5 Tribocorrosion

Tribocorrosion is a complex process that occurs when a material is subjected to both mechanical and chemical degradation in a corrosive environment. It is the combination of mechanical wear and corrosion that results in damage to the surface of a material shown in **Fig. 5**. Tribocorrosion is a phenomenon that occurs when both mechanical wear and corrosion processes occur simultaneously in a material or component that is exposed to a corrosive environment while undergoing friction or sliding [10,15]. It typically occurs in machinery and equipment that operate in harsh environments, such as marine vessels, pipelines, and automotive engines.

When tribocorrosion occurs, the corrosion process can accelerate the wear process, and the wear process can accelerate the corrosion process. This mutual interaction can lead to accelerated material loss, increased friction, and ultimately, premature failure of the component.

Tribocorrosion can be caused by a variety of factors, including the type and concentration of corrosive species in the environment, the type and properties of the material involved, the applied load and speed, and the surface roughness and topography. Managing tribocorrosion requires a comprehensive approach that includes proper material selection, surface modification, lubrication, and corrosion protection [54].

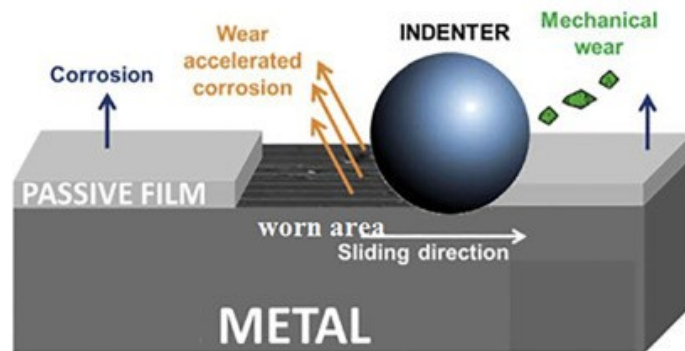


Fig. 5. Schematic diagram for tribocorrosion [55].

3 Experimental Method

3.1 Coating Fabrication Techniques

3.1.1 Plasma Transferred Arc (PTA)

Numerous coating techniques are used to deposit protective coatings for applications involving wear, corrosion, and tribocorrosion [56–59]. The plasma transferred arc (PTA) hard-facing technology has been used to create a thick protective layer by welding. This process is used for the fabrication of the coating in this study. The metallurgical connection between the injected material and the substrate can produce very pure and high-quality deposits. **Fig. 6.** illustrates the schematic of a PTA coating system. The powder form of filler material is introduced into the plasma arc in the shielding gas in order to prevent oxidation of melting particles. The outcome is a high-quality deposit with strong metallurgical bonding of the coating with the substrate. In comparison to other conventional arc methods, PTA has many benefits, including high melting efficiency, high flux stability, and enhanced bonding to the substrate [60]. Because of the high adhesion strength, high hardness, and excellent wear resistance, PTA deposited coatings are of interest in applications where high load-bearing capacity is important [61,62].

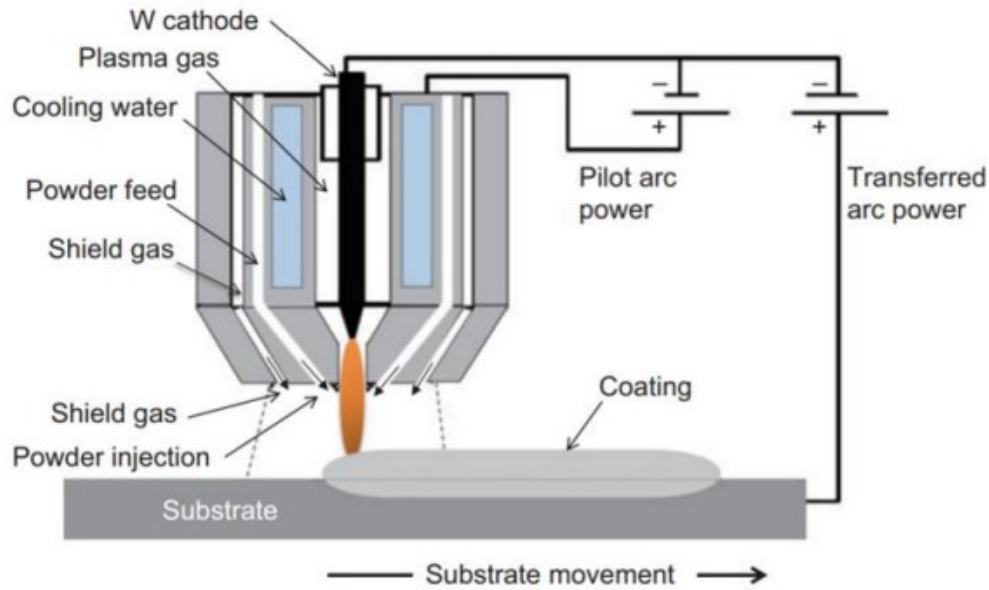


Fig. 6. Schematic of PTA coating [60].

3.1.2 Physical Vapor Deposition (PVD)

Physical vapour deposition (PVD) hard coatings have been extensively utilized for the fabrication of a thin protective coating. This method is well-known to provide excellent wear and corrosion resistant hard protective coatings [12,63]. For the purpose of this work, the sputtering process is primarily considered. In reactive sputtering, the substrate is coated by films using metallic targets and a reactive gas, mixed with an inert working gas (e.g., Ar). The resulting coating can be a solid solution of the target metals doped with the reactive element, a compound, or a mixture of the two [64]. Sputtered coatings vary from nanometers to many microns in thickness and generally have a columnar structure and a smooth coating surface without the presence of macroparticles. **Fig. 7.** illustrates the typical PVD process.

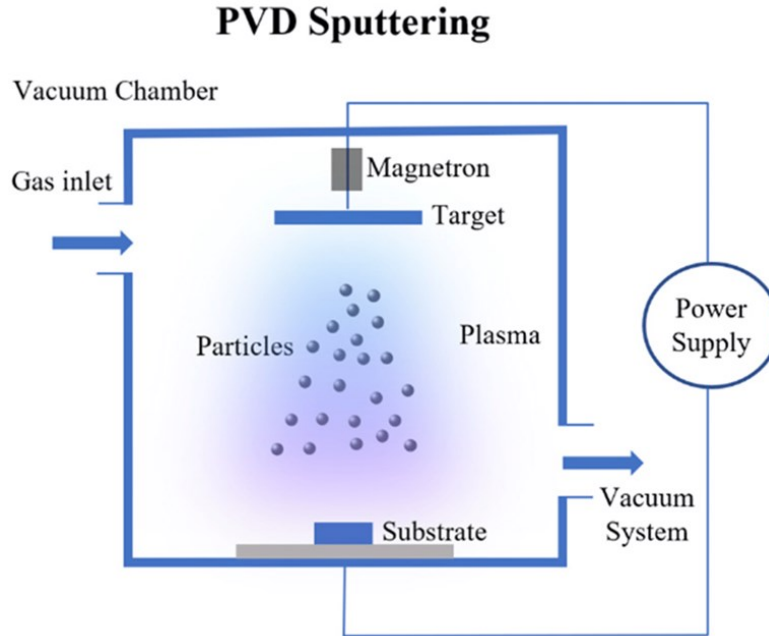


Fig. 7. PVD sputtering process [65].

3.1.3 Duplex Coating

As can be seen from the preceding literature, no substantial research has yet been conducted to investigate the simultaneous effect of wear and corrosion utilizing PTA deposited TiC- and WC-based coatings and PVD deposited TiAlN coatings and their duplex coatings. In this regard, detailed investigations have been carried out with PTA/PVD deposited duplex coatings of TiAlN/TiC-SS/steel and TiAlN/WC-NiBSi/steel to determine the corrosion, wear, and tribocorrosion properties and to compare them to the single layer TiAlN/steel coating and the steel substrate. SEM, indentation, and scratch tests were used to determine microstructural and mechanical characteristics. Tribocorrosion properties were obtained by a sliding wear test under 3.5 wt.% NaCl solution.

3.2 Fabrication of Duplex Coatings

3.2.1 TiC-SS and WC-NiBSi Coatings using PTA

Plasma transferred arc (PTA) method (Kennametal Starweld PTA system with a Kennametal Excalibur welding torch) from InnoTech Alberta, Edmonton, Alberta, Canada was utilized to fabricate thick layer of TiC-based and WC-based coatings. Two groups of coatings namely TiC-316L grade stainless steel (SS) and WC-NiBSi were deposited on low carbon steel by PTA technique. Prior to the deposition, 30 wt.% of TiC (from Pacific Particulate Materials) with 70 wt.% of SS (from Kennametal Delchrome), and 60 wt.% of WC (from Kennametal) with 40 wt.% of NiBSi (from Hoganas 1535-30) were mechanically blended. Commercial-grade argon was used as the shielding, arc, and powder gas. The powder size for the carbide and alloys was from 45 μm to 180 μm . The parameters for the preparation of TiC-SS and WC-NiBSi are summarized in **Table 1**.

Table 1: Deposition parameters for WC-NiBSi and TiC-SS coatings by PTA.

Process Parameter	WC-NiBSi	TiC-SS
Current (A)	200	200
Carriage Speed (in/min)	2.5	2.5
Powder feed rate (g/min)	25	25
Arc Voltage (V)	26	27.5

3.2.2 TiAlN Coating using PVD

A 2-micron thin layer of TiAlN was sputtered deposited on the top of a previously coated steel substrate with WC-NiBSi and TiC-stainless steel by PTA to make the duplex coatings. The “Amod” system for physical vapor deposition (PVD) method from Angstrom Engineering was used. **Fig. 8.** shows how the samples were mounted on the substrate holder for TiAlN deposition. Prior to the deposition of TiAlN films on steel substrate or PTA deposited TiC-SS/steel or WC-NiBSi coatings, the surfaces were sputtered cleaned for a total time of 20 minutes in radio frequency (RF) plasma with a pressure of 10 mTorr and substrate biasing of -450 V. The cleaning process was done in a gas mixture of N₂ and Ar (5 sccm and 30 sccm flow rate, respectively) at a temperature of 300 °C. A Ti interlayer of about 375 nm was added before the TiAlN deposition to enhance the adhesion of TiAlN with the substrate. Pulsed direct current (pDC) sputtered (300 W) from a pure Ti target under Ar atmosphere of 3 mTorr and 75 V of substrate biasing was used for interlayer. Reactive magnetron sputtering using a mixed N₂ and Ar environment and 19 sccm and 30 sccm flow rates, respectively, resulted in the deposition of a 2-micron thin TiAlN film at 300 °C substrate temperature. The base pressure was 10⁻⁶ Torr, while the operating pressure was 3 mTorr. The film was produced by co-sputtering two 3” diameter pure Ti and pure Al targets. Both targets (Ti and Al) were supplied by Kurt J. Lesker and the purity levels are 99.97 at. % (Ti) and 99.995 at. % (Al). A pulsed DC discharge was applied to the Ti target (average power of 300W, 30 kHz) and a high-power impulse magnetron sputtering (HiPIMS) discharge was applied to the Al target (average power of 660 W, frequency of 400 Hz and duty cycle of 8%). The substrate was subjected to a DC bias tension of -75 V. The distance of the targets from the substrates was 10 cm and the substrates were rotated at a speed of 3 RPM. Finally, a single layer coating of TiAlN on steel and two sets of duplex coatings were obtained by the PVD method. The two sets of duplex

coatings are namely, (i) TiAlN/WC-NiBSi/Steel coating, and (ii) TiAlN/TiC-316L grade stainless steel (SS)/Steel coating. In addition, the single layer coatings deposited by PTA and by PVD on low carbon steel were prepared. The coatings' architecture is shown in **Fig. 9**.

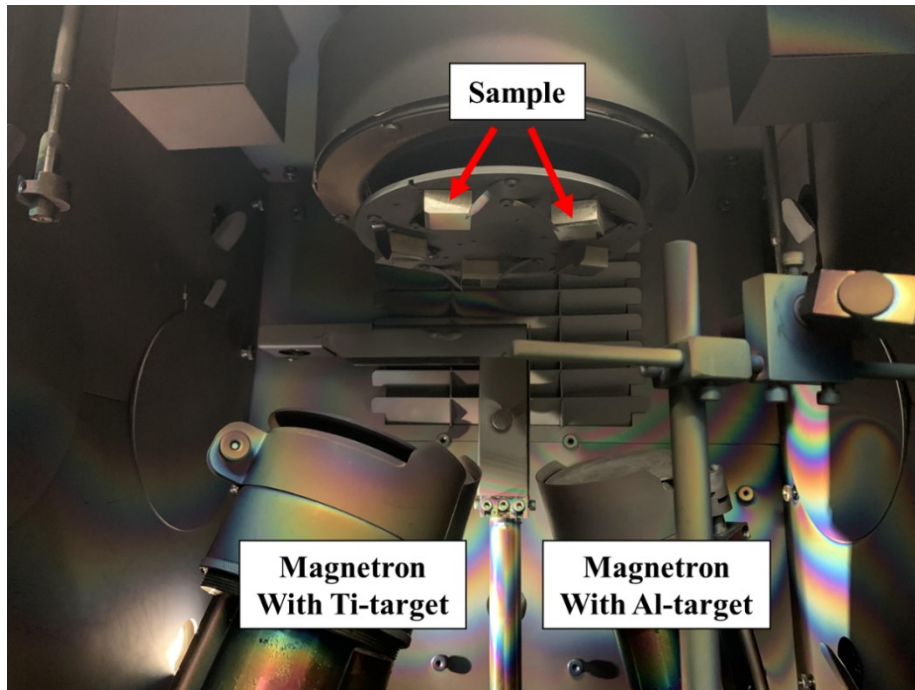


Fig. 8. Experimental set-up for PVD deposition.

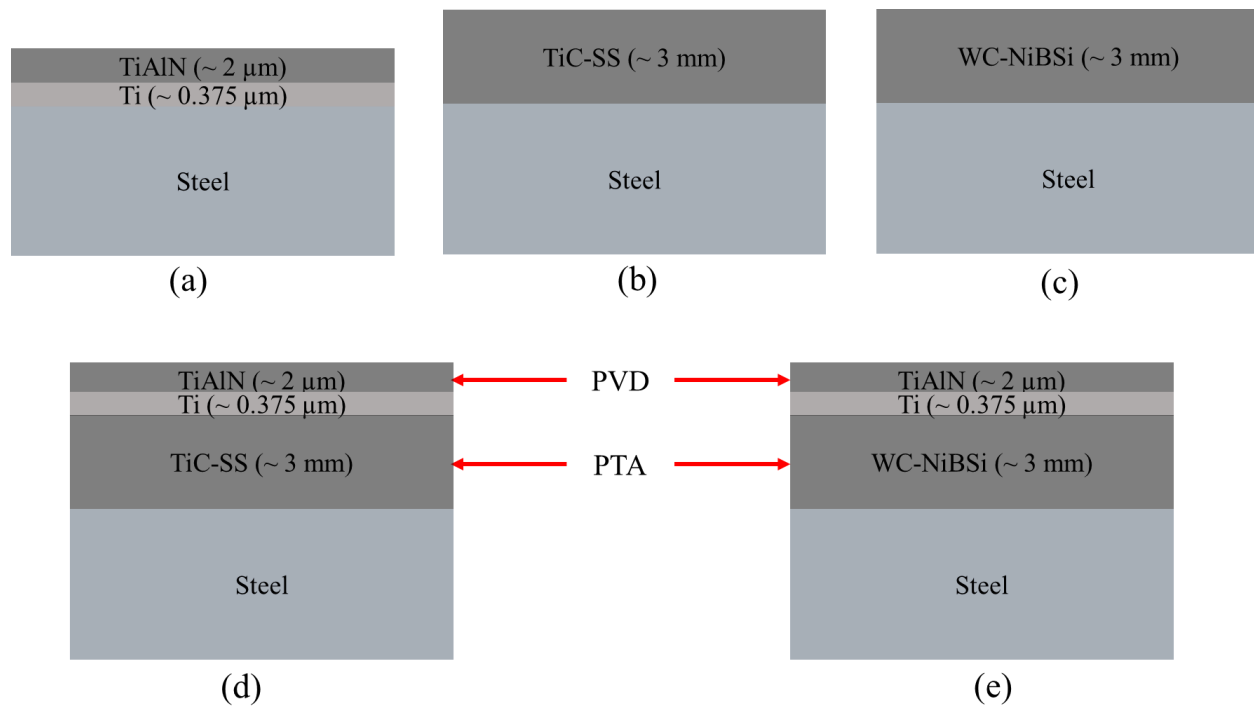


Fig. 9. Schematic representation of the coating's architecture with (a) TiAlN/Ti/Steel, (b) TiC-SS /Steel, (c) WC-NiBSi/Steel, and duplex coatings (d) TiAlN/Ti/TiC-SS/Steel (e) TiAlN/Ti/ WC-NiBSi/Steel.

3.3 Surface Characterization

The surface morphology and chemical composition of coatings were analyzed using a Zeiss Sigma 300 VP scanning electron microscope (SEM) facility from the University of Alberta. The SEM is equipped with secondary and backscattered electron detectors, an in-lens electron detector, a cathodoluminescence (CL) detector, and a Bruker energy dispersive X-ray spectroscopy (EDS) system. The EDS system includes dual silicon drift detectors, each with an area of 60 mm² and a resolution of 123 eV. This equipment was used to examine the coatings both before and after exposure to the wear, corrosion, and tribocorrosion system. Before the SEM analysis, the samples

were ultrasonically cleaned for 15 minutes with ethanol and finally air cleaned for any loosely attached particles. Scratch software by CSM Instruments was used to evaluate the surface after scratch testing.

3.4 Mechanical Properties Analysis

3.4.1 Hardness Tests

Indentation tests (ASTM E2546-15(2015)) were performed to determine the mechanical characteristics such as hardness (H) and elastic modulus (E) of the substrate, PTA coatings, and PVD coatings. The microhardness and elastic properties of the steel substrate, thick TiC-SS/steel and WC-NiBSi/steel coatings were measured during the instrumented micro-indentation tests using a Micro Combi Tester (MCT3) with a Berkovich diamond pyramidal tip. Four indentations on four different areas with three repetitions per sample were completed. The applied load was gradually increased from 10 mN at a rate of 500 mN/min to a maximum load of 20 N, kept constant for 5s before linearly decreasing the load. For nano-indentation, a depth-sensing Hysitron TI 950 TriboIndenter with a Berkovich diamond tip was utilized and the tip was calibrated using a fused silica standard. For each coating, a 25-cycle partial-unload and load function was applied to a 5 by 5 indentation array with a 100 μm spacing between indentations. For each load cycle, the load increased from 10 mN to the maximum load of 600 mN for 5s followed by a 2s holding region, and then linearly decreased for 5s to the 80% of the maximum load. The average hardness and reduced modulus of elasticity were measured by the widely used approach given by Oliver and Pharr [66]. According to this method, the hardness is measured by

$$H = \frac{P_{max}}{A}$$

The reduced modulus of elasticity is measured by

$$E^* = S \frac{\sqrt{P_{max}}}{2\sqrt{A}}$$

Where P_{max} is the peak load, S is the stiffness, and A is the contact area. The area of contact at peak load is influenced by the depth of contact and the geometry of the indenter.

More information on micro- and nano-indentation techniques for hardness and elasticity can be obtained from [67] and [68], respectively.

3.4.2 Scratch Tests

A scratch test (ASTM C1624-05) was performed at the Polytechnique Montreal, Canada using a CSM Micro-Combi scratch tester equipped with a Rockwell C diamond indenter (AV-233) of 200 μm radius to evaluate the adhesion strength of PVD deposited TiAlN thin films on low carbon steel, PTA deposited TiC-SS and WC-NiBSi coatings. A progressive liner force ranging from 0 to 30 N was applied at a speed of 10 mm/min across a 3 mm scratch length. The findings from the scratch test experiments were used to assess how the adhesion strength of the TiAlN thin films was influenced by the underlying layers of low carbon steel substrate, PTA fabricated TiC-SS, and WC-NiBSi thick coatings. SEM analysis was done to examine the scratch surface and determine the shape of the cracks.

3.5 Tribological and Tribocorrosion Analysis

3.5.1 Tribological Characteristics

The tribological behavior of various samples, including uncoated steel, single-layered, and duplex-layered coatings on steel, was studied using a ball-on-flat tribo-system (ASTM G133-05(2016)) from Tricomat at normal ambient conditions, as shown in **Fig. 10**. Wear tests can be performed in either dry or wet conditions. While the contact ball or test specimen is fully submerged in the test solution for wet wear (tribocorrosion) tests, the cell is not filled with electrolytes for dry wear tests. Only a sliding contact motion is introduced with applied load without any electrolyte. An alumina (Al_2O_3) ball of 4.75 mm was used as a counterpart and a new alumina ball was used in each test. Two different normal loads of 2N and 5N were applied on the alumina counter body to study the wear properties and load-bearing capacity of the PTA coatings on the duplex coatings system. The wear tests were performed under dry conditions using a sliding frequency of 1 Hz and a sliding length of 10 mm with a sliding velocity of 20 mm/s. The total sliding distances are 20 m, 40 m, and 80 m for 1000, 2000, and 4000 loading cycles respectively. In this configuration, the surface of the sample was placed horizontally. During the wear tests, the tangential force was recorded continuously, and the coefficient of friction, μ was obtained from $\mu = F_t/F$, where F_t is the tangential force and F is the normal force. The average value of the friction coefficient for each of the tests was obtained from the stable segment (preferably at the end) of the friction coefficient curves. After the wear tests, each of the wear tracks was investigated with a DektakXT contact profilometer to get the wear profile, wear depth, and area of the worn surfaces of the wear track. The total volume of the worn surfaces in mm^3 was then calculated from the area and the total length of the wear track. A typical wear profile is shown in **Fig. 11**.

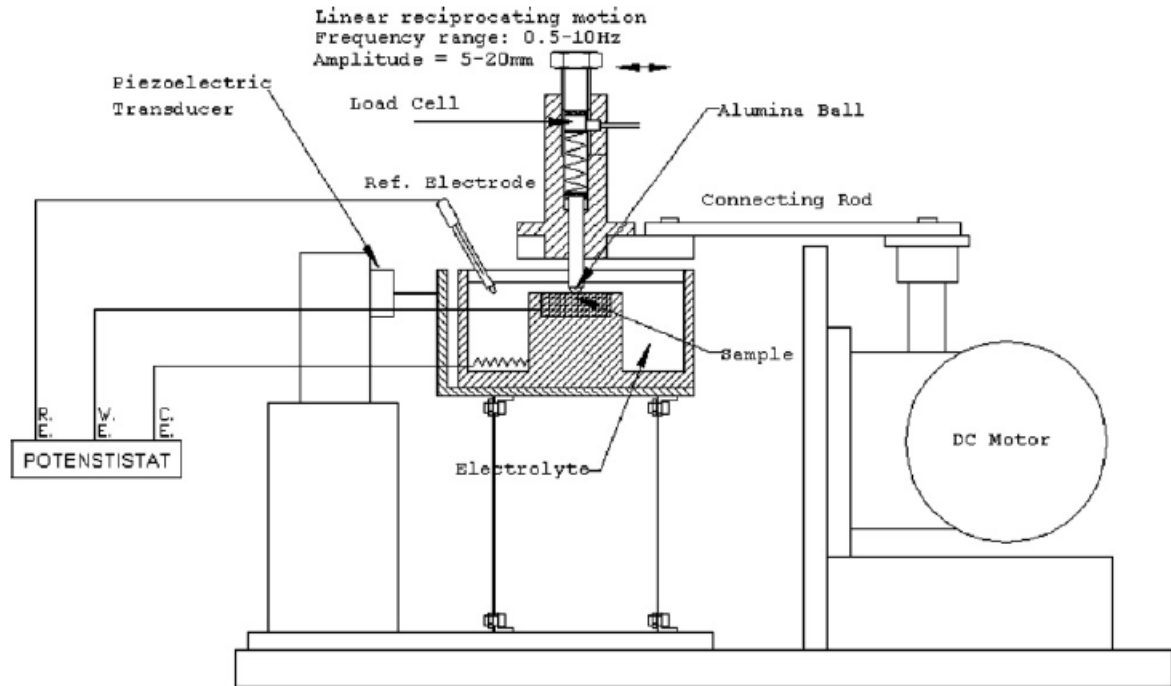


Fig. 10. Illustration of wear tests under dry sliding conditions [69].

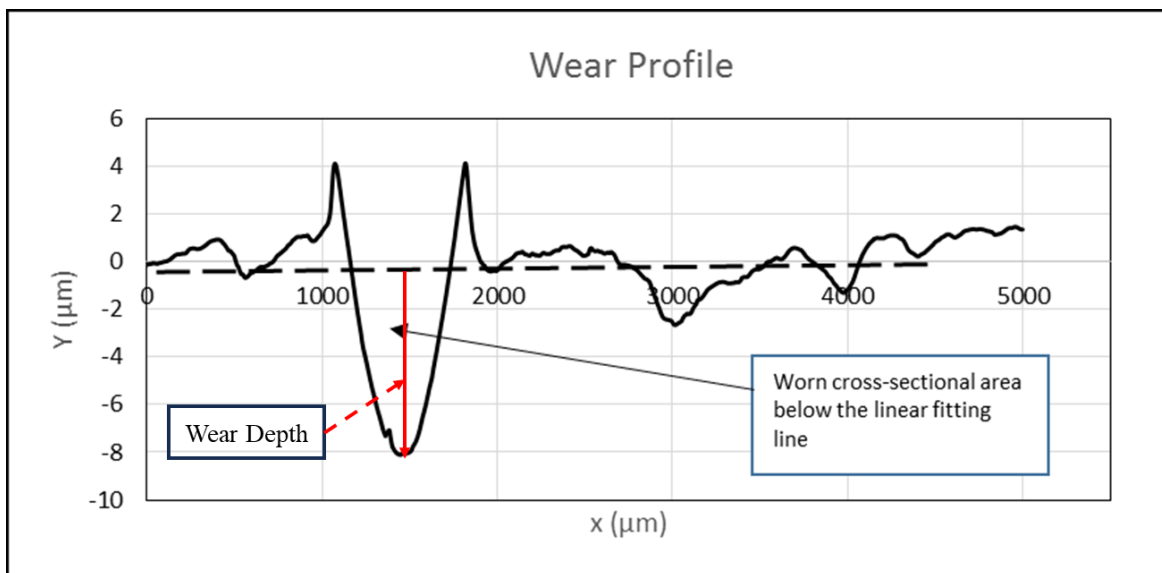


Fig. 11. Typical wear profile after wear tests [70].

3.5.1.1 Assessment of Tribological Properties

The wear experiments are conducted by sliding or rotating a counter body in contact with a specimen. During the wear tests, the tangential force was continually recorded throughout the wear tests, and the coefficient of friction is calculated using the formula below:

$$\mu = \frac{F_t}{F}$$

Where F_t is the tangential force and F is the normal force.

After the wear tests, each of the wear tracks was investigated to get area of the worn surfaces of the wear track. The total volume of the worn surfaces is calculated from the area and the total length of the wear track.

$$V = A \times L$$

Where V is the volume of the worn surfaces, A is the area of worn surfaces, and L is length of the wear track.

The wear rate is measured from the following equation:

$$K = \frac{V}{F \times s}$$

where F is the applied load and s is the total sliding distance.

3.5.2 Corrosion

The performance of the PTA and PVD deposited single layer and duplex coatings as well as the bare steel was analyzed under the corrosion attack using a three-electrode electrochemical cell (ASTM G5-14(2021) and ASTM G61-86(2018)) in a 3.5 wt.% NaCl aqueous solution. The corrosion cell was modified from these standards to accommodate coated samples. The sodium chloride salt concentration of 3.5 wt.% was chosen because the typical salinity of ocean water is on average around 3.5 wt.% [71]. The sample which was pressed against a 10 mm inner diameter O-ring with a conducting plate for electrical connection served as the working electrode (WE). A copper plate was used for the electrical connection. The total exposure area of the sample inside the O-ring to the electrolyte solution was 0.79 cm². In this configuration, the surface of the coating was vertically positioned. A standard calomel electrode (SCE) was used as the reference electrode and a graphite rod was used as the counter electrode (CE). The experimental set-up for corrosion is presented in **Fig. 12**, where the sample acted as an anode and graphite acted as a cathode. An Autolab PGSTAT302 Echochemie potentiostat equipped with a frequency response analyzer (FRA) was utilized for the electrochemical measurements including open circuit potential (OCP), electrochemical impedance spectroscopy (EIS) and polarization.

To begin with the corrosion experiments, the surface of the examined coating was exposed to the electrolyte solution for 3600s until the stabilization of open circuit potential (OCP) was reached. After the OCP measurements, the electrochemical impedance spectroscopy was performed at OCP with a frequency varying between 10⁵ Hz and 10⁻² Hz using an AutoLab frequency response analyzer program (FRA, Eco Chemie B.V. Utrecht). Afterward, potentiodynamic polarization test was carried out starting from a potential of 0.2 V below the OCP from the cathodic region up to 2

V in the anodic region at a scan rate of 0.001 V/s. The corrosion potential (E_{corr}) and corrosion current (i_{corr}) were obtained from potentiodynamic polarization curve.

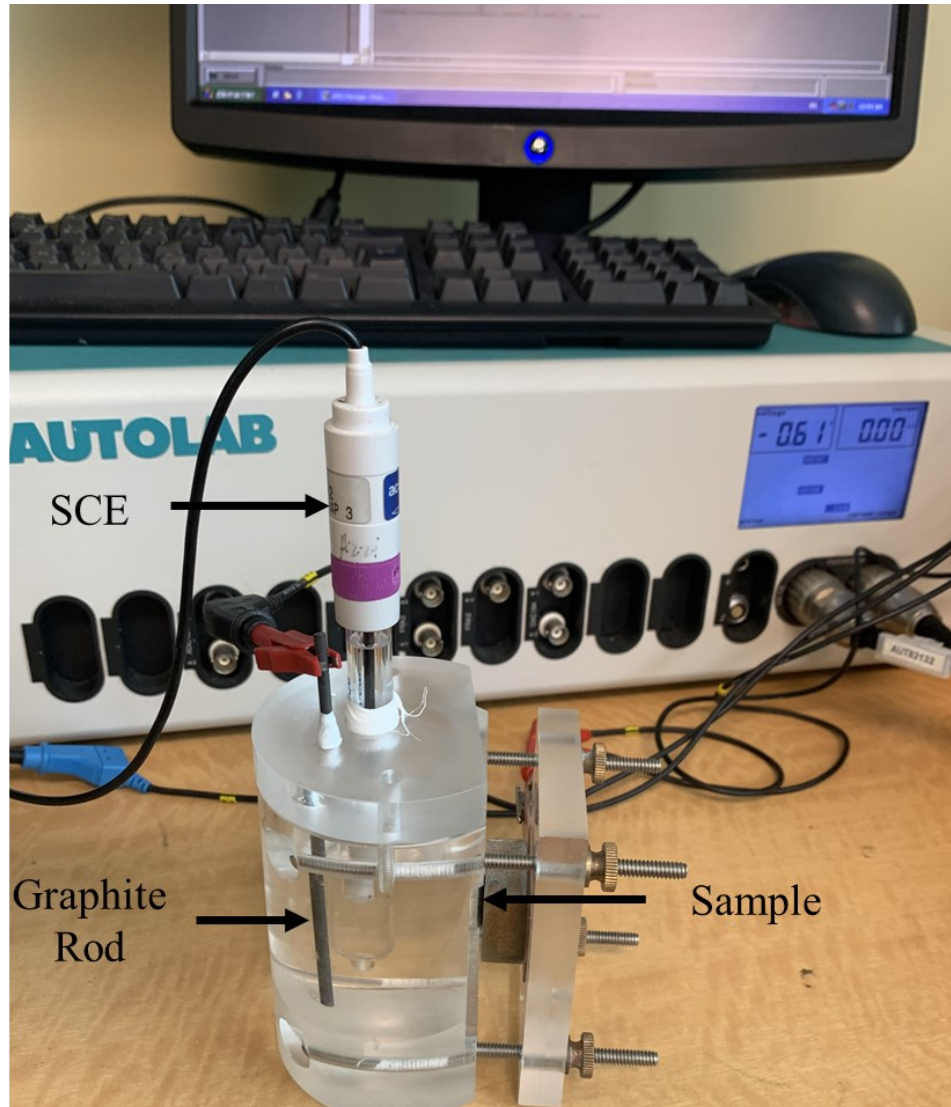


Fig. 12. Experimental set-up for corrosion experiments under 3.5 wt.% NaCl.

3.5.2.1 Assessment of Corrosion Properties

For corrosion studies, typically open circuit potential (OCP), electrochemical impedance spectroscopy (EIS), and polarization tests are conducted to understand the corrosion behaviour of the coatings. The open circuit potential (OCP) is one of the important techniques to study corrosion. In OCP, the corrosion potential is recorded as a function of time as shown in **Fig. 13**. Over time, the corrosion potential approaches to a stable value. Metal has a noble corrosion potential when it moves towards more positive potential. Noble corrosion potential is the electrochemical potential in a corrosive environment where a metal exhibits the least degree of electrochemical activity and where the potential typically approaches the potential of the noble element in the electromotive series. Noble metals often have high corrosion and oxidation resistance [72].

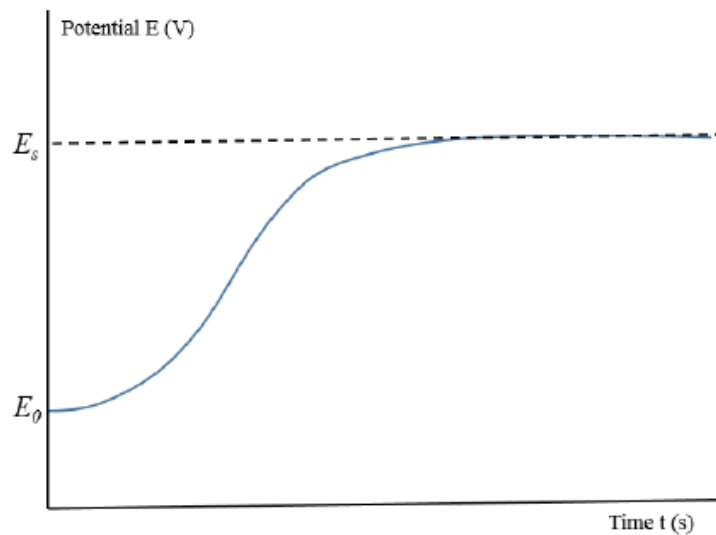


Fig. 13. The open circuit potential (OCP) [73].

Electrochemical Impedance Spectroscopy (EIS) is a widely used electrochemical technique to understand the electrochemical reaction involved. Electrochemical impedance spectroscopy (EIS) measurements of impedance are represented graphically in the Nyquist plot. The Nyquist plot is generated by displaying the imaginary (Y-axis) part of the measured impedance versus the real (X-axis). A typical Nyquist plot is presented in **Fig. 14**. The equations [74] for the impedance analysis are presented below:

The ratio of the applied sinusoidal voltage to the resulting current is the system's impedance Z .

$$Z = \frac{\Delta E}{\Delta I} = \frac{E_0 \sin(\omega t)}{I_0 \sin(\omega t - \varphi)}$$

The impedance, Z with magnitude Z_0 can be written as a complex function.

$$Z = \frac{\Delta E}{\Delta I} = \frac{E_0 \sin(\omega t)}{I_0 \sin(\omega t - \varphi)} = \frac{E_0}{I_0} \exp(j\varphi) = Z_0 \exp(j\varphi) = Z_0 \cos(\varphi) + j Z_0 \sin(\varphi)$$

Where E_0 is the imposed potential, ω is the radial frequency, I_0 is the amplitude of current, and φ is the phase angle with respect to potential.

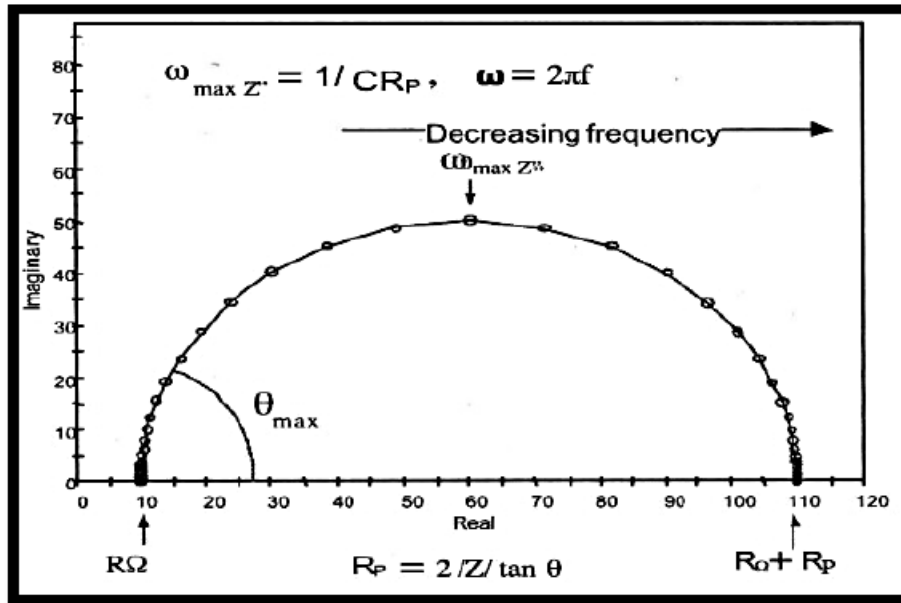


Fig. 14. Nyquist plot for an electrochemical system [47].

The polarization test is also extensively studied in corrosion studies. In this technique, the corrosion current is observed under applied potential. The relationship between corrosion current and corrosion potential is presented by the Butler-Volmer equation [74].

$$I = I_0 \exp\left(\frac{2.303\eta}{\beta_a}\right) - I_0 \exp\left(\frac{-2.303\eta}{\beta_c}\right)$$

Where η is the overpotential on working electrode ($= E - E_{oc}$), I_0 ($= I_{corr}$) is the corrosion current density, β_a is the Tafel constant at anodic, and β_c is the Tafel constant at cathodic.

For the large anodic potential, the equation can be rewritten as

$$I = I_0 \exp\left(\frac{2.303\eta}{\beta_a}\right)$$

Taking the logarithm of both terms,

$$\eta_a = \beta_a \log(I_a - I_0)$$

Similarly, for large cathodic potential,

$$\eta_c = -\beta_c \log(-I_c - I_0)$$

This relationship is presented as Tafel plot in **Fig. 15**. The linear portions of the anodic and cathodic graphs can be extrapolated to determine the corrosion current (I_0) and corrosion potential (E_0). If a line is drawn from the intersecting point, the corrosion current and corrosion potential are represented by the intercepts to the X and Y axes, respectively.

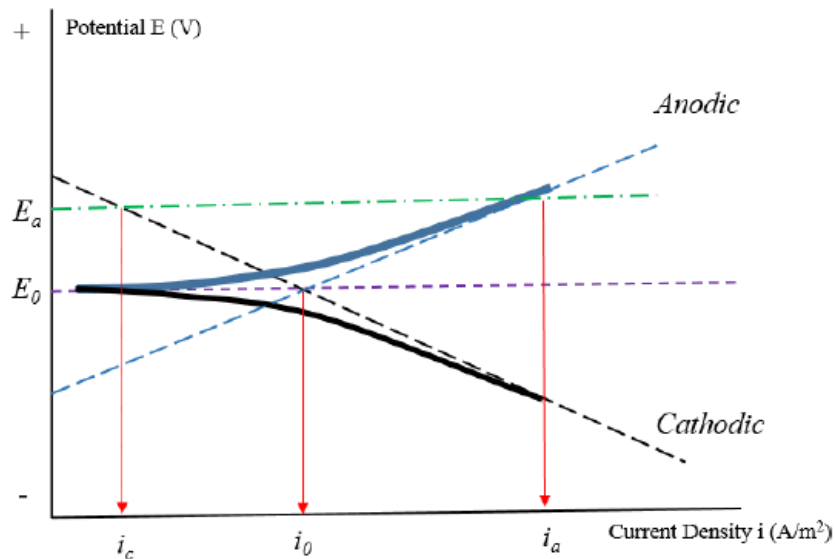


Fig. 15. Illustration of Tafel plot [73].

3.5.3 Tribocorrosion

To understand the synergistic effect of wear and corrosion, a series of tribocorrosion (ASTM G119-09(2021)) experiments were performed using the same linear reciprocating ball-on-flat tribometer system which was used for the dry wear analysis. However, the sliding contact was fully immersed in a 3.5 wt.% NaCl corrosive medium for the tribocorrosion tests as shown in **Fig. 16**. A three-electrode cell electrochemical system was used where the coating served as the working electrode, a standard calomel electrode was used as reference electrode, and a platinum wire was used as the counter electrode. As with the wear tests, the coatings' surface was immersed in the electrolyte solution in a horizontal position. An alumina ball (4.75 mm in diameter) was used to continuously rub the surface of the specimen immersed in the test solution until the sliding cycle ends. The alumina ball was chosen due to its high hardness and chemical inertness. A 2N load was applied with 2000 cycles for all the tribocorrosion experiments and with a stroke length of 10mm.

Two different tests for tribocorrosion studies were done namely (i) wear at OCP where no potential was applied, (ii) wear at potentiostatic polarization where a fixed potential was applied relative to the OCP of individual coatings. Each of these tests was done in several steps. Firstly, the sample was immersed in the electrolyte solution for 60min to reach the stability of the potential. Next, the sliding action was initiated with the pre-applied loaded condition (2N) for 2000 cycles on the surface of the sample which was immersed in the NaCl solution. After finishing the sliding wet wear, the sample was kept in the aqueous solution for another 60 min to allow the repassivation of the surface of the sample. Before, during, and after the sliding wear tests, the OCP was continuously monitored. Also, the frictional behavior was monitored during the wear tests. For the

potentiostat tests, first, the sample was immersed and kept in the solution for 1h to reach in a stable OCP, followed by the potentiostatic tribocorrosion tests where 0.2V potential was applied below the OCP. The current was monitored before, during, and after the sliding motion for 1000 seconds, 2000 cycles, and 1000 seconds, respectively. The coefficient of friction was recorded during the rubbing action under wet conditions. After the potentiostatic tribocorrosion tests, the OCP was recorded for another 600 seconds without the applied potential.



Fig. 16. (a) Tribocorrosion system where sliding contact immersed in NaCl aqueous solution and (b) position of the immersed sample at the end of the tribocorrosion tests.

3.5.3.1 Assessment of Tribocorrosion Properties

A series of experiments have been conducted to assess the tribocorrosion properties of different coating systems. In tribocorrosion experiments, the samples are immersed in the electrolyte solution where the tribological system is utilized to investigate the synergistic effect of wear and corrosion. M. Azzi et al. [75] investigated the tribocorrosion behaviour of DLC film on the

stainless-steel substrate. During assessing the tribocorrosion properties, they systematically described the sequence of tribocorrosion which is shown in **Fig. 17**. Firstly, the sample was immersed in the corrosive solution for 60 minutes, during which time the potential began to stabilize (Region I). Then the sliding wear test was started. The alumina ball was used to initiate the rubbing with the applied load on the surface of the sample. The electrochemical behaviour was observed during the sliding wear using EIS techniques which is shown in Region II. During this period, the OCP was continuously monitored (Region III). The sliding wear test was stopped after 1800 sliding wear cycles. The OCP was also measured after finishing the wear tests (Region IV). The electrochemical behavior of the surface after sliding wear was then investigated using EIS (Region V). To further understand the tribological and corrosion characteristics of a-SiC:H coatings created by PECVD, S. Guruvenket et al. [76] conducted tribocorrosion tests using a linear reciprocating ball-on-plate tribometer. The equipment for reciprocating wear tests was submerged entirely in a sodium chloride solution. Before, during, and following the sliding wear experiments, the free corrosion potential (FCP) was measured. During the tribo-corrosive experiment, electrochemical impedance spectroscopy (EIS) was also used to assess how wear affected the coatings' ability to resist corrosion. The EIS data was represented using a Nyquist diagram. The friction behaviour and wear rate were studied during the tribocorrosion experiments. Y. Sun, V. Rana [10] explained the wear-induced corrosion and corrosion-induced wear behaviour during tribocorrosion tests on AISI 304 stainless steel in 0.5 M NaCl solution. Potentiostatic experiments at constant potential were done where transient current and coefficient of friction were continuously measured. Following each test, the measurement of the surface profile across the wear track enabled for the evaluation of the total wear volume resulting from the combined effect of wear and corrosion.

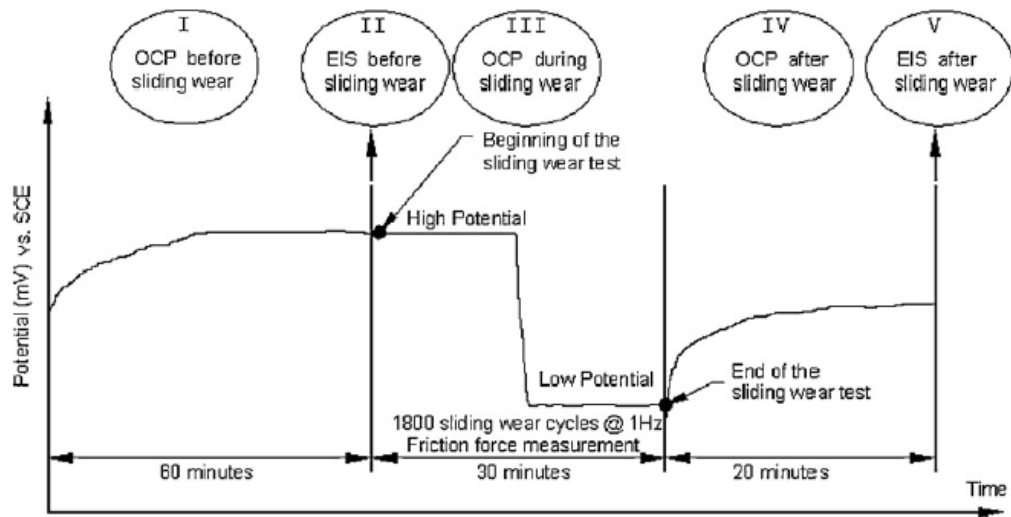


Fig. 17. The sequence of operations for tribocorrosion tests with OCP evolution [75].

In this study, similar techniques were adopted to analyze wear, corrosion, and tribocorrosion properties. For wear analysis, a tribological system with ball-on-flat slid through the coating. The friction behaviour was monitored, and the wear rate was measured. For corrosion analysis, a three-electrode cell electrochemical system was employed to conduct the tests for open circuit potential (OCP), electrochemical impedance spectroscopy (EIS), and Potentiodynamic polarization. For tribocorrosion analysis, the tribological system in contact with the specimen was immersed in the electrolyte. The synergistic effect of wear and corrosion can be realized by this method. The tribocorrosion analysis was done in two different experiments; i) at OCP where no external potential was applied and ii) at potentiostatic polarization where external potential was applied. For OCP conditions, the friction behaviour and OCP were obtained during the tests, and wear rate was measured. For tribocorrosion at potentiostatic polarization, the friction coefficient and corrosion currents were obtained, and the wear rate was measured. SEM and EDS were employed to analyze the surface of the coatings after and before the tests.

4 Results and Discussions

4.1 Microstructure of the Deposited Coating Systems

Scanning electron microscopy (SEM) was used to perform a microstructural examination of 3 mm thick PTA single layer and about 2-micron thick PVD single layer deposited coating (TiC-SS/steel, and WC-NiBSi/steel), (TiAlN/steel), and duplex coatings (TiAlN/TiC-SS/steel and TiAlN/WC-NiBSi/steel). The results are shown in **Fig. 18**. It can be seen from **Fig. 18(a)** for the PTA thick TiC-stainless steel composite coating that after the PTA melting process small-sized and some large TiC particles are embedded in the stainless-steel matrix. Particularly, there are no undissolved or unmelted TiC particles in the matrix. However, the surface of the TiC-SS coating is uneven, and some small pores are visible on the surface. On the other hand, a tree-like structure of WC particles can be observed all over the surface of WC-NiBSi coating shown in **Fig. 18(b)**. In addition, large WC particles are grouped together in different areas on the surface and connected with the tree-like structure. There are some lateral cracks both on the NiBSi and WC phases. The thermal stress resulting from quick solidification and the mismatch in thermal expansion between the WC and NiBSi phases lead to cracks [38]. Besides the cracks, the surface also has some globular and intergranular pores due to insufficient contact between the subsequent splats. It is known that a continuous coating layer is formed when many overlapping splats solidify and stick to one another [77]. The surface of the TiAlN coatings on steel deposited by PVD in **Fig. 18(c)** displays quite a smooth and compact structure with 2-micron thickness with few numbers of defects [41]. **Fig. 18(d)** for TiAlN/TiC-SS/steel and **Fig. 18(e)** for TiAlN/WC-NiBSi/steel duplex display relatively uniform surfaces with numerous defects. Interestingly, the TiAlN coating sealed

the pores of the TiC-SS/steel and WC-NiBSi/steel coatings. As a result, no pores are observed in the duplex coatings systems.

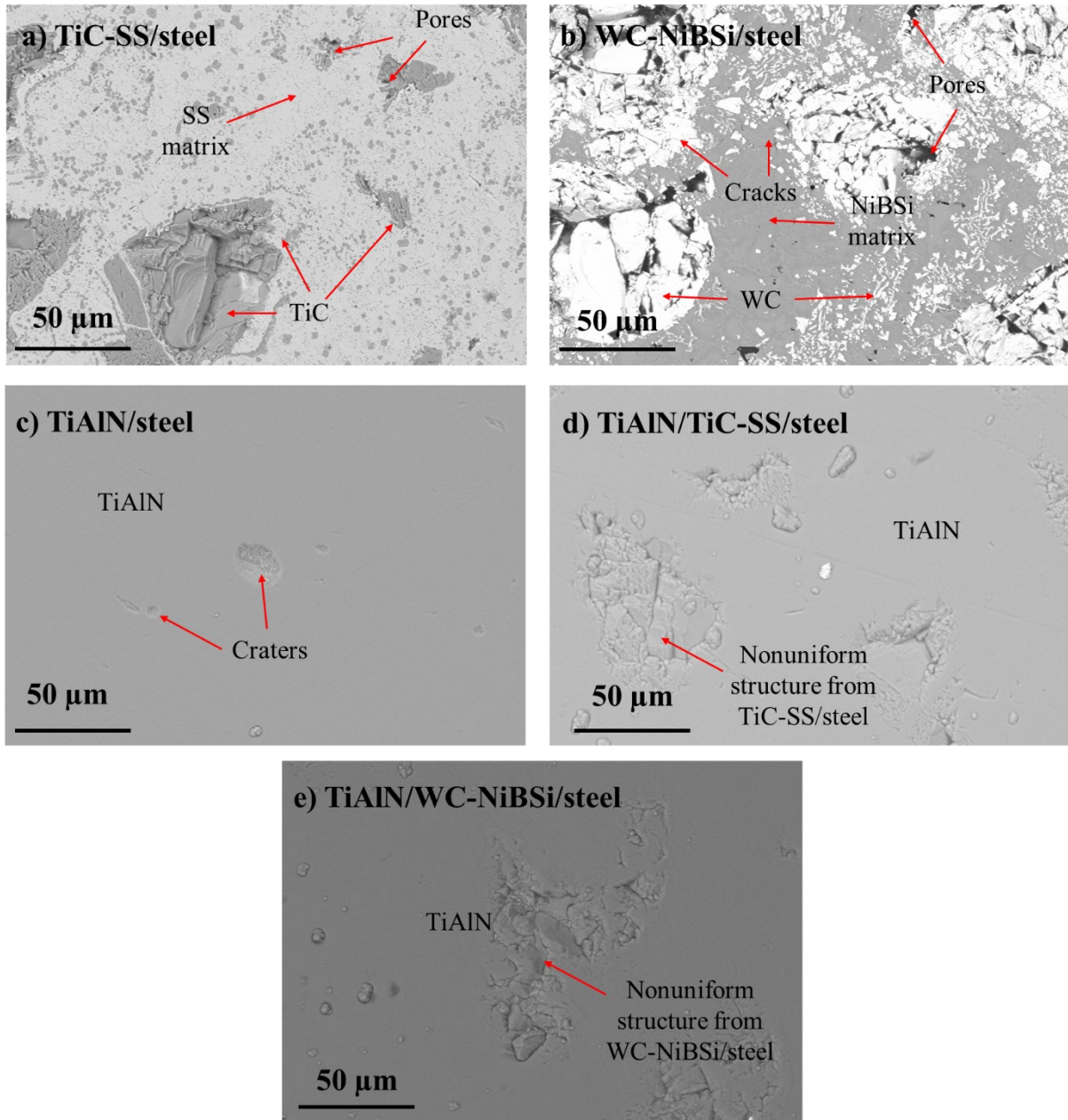


Fig. 18. SEM images on the surfaces of single and duplex coatings on steel: a) TiC-SS/steel coating by PTA, b) WC-NiBSi/steel coating by PTA, c) TiAlN/steel coating by PVD, d) TiAlN/TiC-SS/steel coating by PVD/PTA, and e) TiAlN/WC-NiBSi/steel coating by PVD/PTA.

4.2 Mechanical Characterization

4.2.1 Mechanical Properties

The mechanical properties obtained from the micro- and nano-indentation testes are presented in **Fig. 19.** for hardness (H) and reduced Young's modulus of elasticity (E^*), and in **Fig. 20.** for elastic strain to failure (H/E^*) and resistance to plastic deformation (H^3/E^{*2}). The ratio of hardness and elasticity H/E is the resistance of elastic strain to failure. Toughness is defined as the ability to absorb energy to fracture [78,79]. The H^3/E^{*2} indicates the coating's capacity to withstand a load [80]. As a result, these are the important factors to access the toughness of the film. The bare substrate had the lowest hardness while the coating on steel improved hardness in the following order: TiAlN/WC-NiBSi/steel > TiAlN/steel > TiAlN/TiC-SS/steel > WC-NiBSi/steel > TiC-SS/steel > steel. However, E, H/E, and H^3/E^{*2} do not follow the same trend. Duplex TiAlN/WC-NiBSi/steel coating showed the highest H and E value due to the harder interlayer of WC-NiBSi than steel. E value for TiAlN is comparatively lower which results in the highest H/E and H^3/E^{*2} value. J. Musil [81] explained that the higher H/E helps to lower the coefficient of friction and wear rate due to enhanced resistance to cracking. E. Bousser et al. [82] showed that the erosion behaviour of Cr-Si-N coating system improved with increasing H^3/E^{*2} . However, in order to increase deformation resistance because hard coatings are prone to brittle fracture, H/E and H^3/E^{*2} should be maximized by decreasing E value with optimal hardness [83]. The lowest values were found for steel, whereas the H/E and H^3/E^{*2} values for duplex coatings are substantially lower than TiAlN.

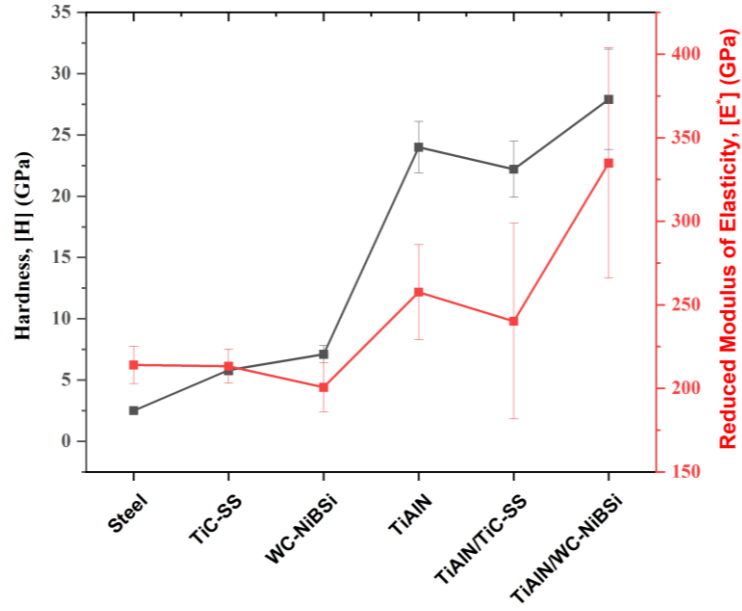


Fig. 19. Hardness, H , and reduced modulus of elasticity, E^* for the substrate and coatings.

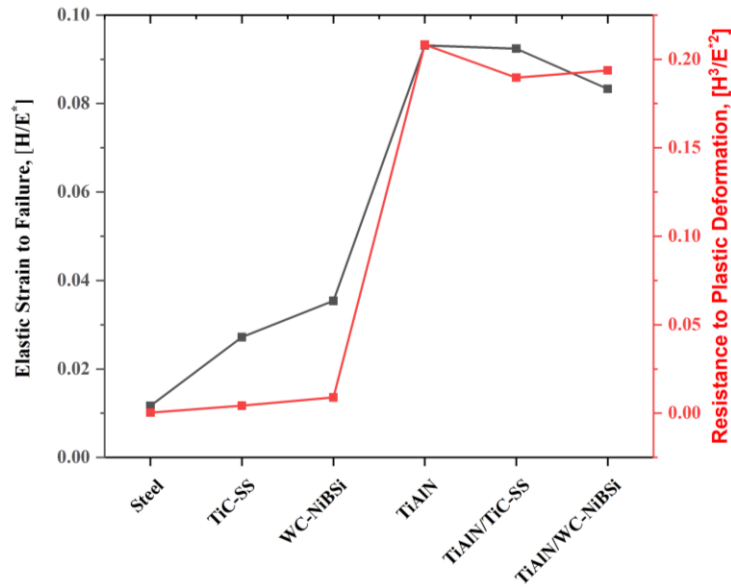


Fig. 20. Elastic strain to failure, H/E^* , and Resistance to plastic deformation, H^3/E^{*2} , for the substrate and coatings.

4.2.2 Adhesion Strength of TiAlN Coating

The micro-scratch test measurement was used to assess the adhesion strength of TiAlN with the steel substrate, TiC-SS/steel coating, and WC-NiBSi/steel coating with increasing load from 0 to 30 N. **Fig. 21(a)** shows the scratch tracks with or without a TiAlN layer and **Fig. 21(b)** represents the higher magnified images toward the end of the track with the EDS analysis. To determine if the TiAlN for the duplex coatings has completely delaminated, image analysis was conducted towards the end of the track. The critical load values, L_c , are consisted of three load values (L_{c1} , L_{c2} , and L_{c3}), where L_{c1} represents the load at which the first crack emerges, L_{c2} represents the load at which there are consistent cracks over the scratch track, and L_{c3} represents the load at which the coating completely delaminates [84]. **Table 2** displays the critical load values (L_{c1} , L_{c2} , and L_{c3}) that correlate to the coatings' surface cracking. At very low loads (less than 1 N), TiAlN/steel experienced the first crack. The value of L_{c1} increased to 2.4 N and 4.9 N when PTA coated TiC-SS and WC-NiBSi layers, respectively were added. TiAlN layer was completely removed at $L_{c3} = 14.7$ N where no removal of TiAlN could be seen for the TiAlN on PTA-coated coatings. The L_{c2} values for TiAlN/TiC-SS/steel and TiAlN/WC-NiBSi/steel are 11.4 N and 15.5 N, respectively demonstrating the improvement of adhesion strength in the order of TiAlN/WC-NiBSi/steel > TiAlN/TiC-SS/steel > TiAlN/steel.

The top surfaces after the scratch test were investigated by SEM micrographs in **Fig. 21**. Steel, TiC-SS/steel coating, and WC-NiBSi/steel coating all show ploughing of the material with some cracks; however, as hardness increases, the width of the scratch tracks decreases. For TiAlN/steel coating, adhesion failures occurred for TiAlN hard coating on ductile steel substrate due to compressive stress developed as the applied load increased [84]. The TiAlN coating-substrate

interface was plastically deformed due to the applied load, and with the increasing load, the coatings failed due to the increased plastic deformation as shown in **Fig. 21**. in region 4. EDS confirmed the delamination of the TiAlN coating from steel. In **Fig. 21(b)**, in regions 5 and 6, EDS showed large peaks of Ti, Al, and N elements indicating TiAlN layer sustained on the coatings. This indicates good adhesion strength of PVD coating with the PTA coatings. Nevertheless, cracks of TiAlN coating towards the end of the scratch track and some delamination could be observed. TiAlN/WC-NiBSi/steel coating exhibited greater resistance to plastic deformation with increased hardness (H) and H^3/E^{*2} ratio. Thus, the relatively higher tribological performance of hard TiAlN/WC-NiBSi/steel is because of the higher load-bearing capacity of the intermediate WC-NiBSi layer.

Table 2: Critical load values for the single layer TiAlN coating and duplex TiAlN/TiC-SS/steel and TiAlN/WC-NiBSi/steel coatings after scratch test of varying load from 0 to 30 N.

Samples	Lc1 (N)	Lc2 (N)	Lc3 (N)
TiAlN/steel	0.9	5.4	14.7
TiAlN/TiC-SS/steel	2.4	11.4	–
TiAlN/WC-NiBSi/steel	4.9	15.5	–

(a)

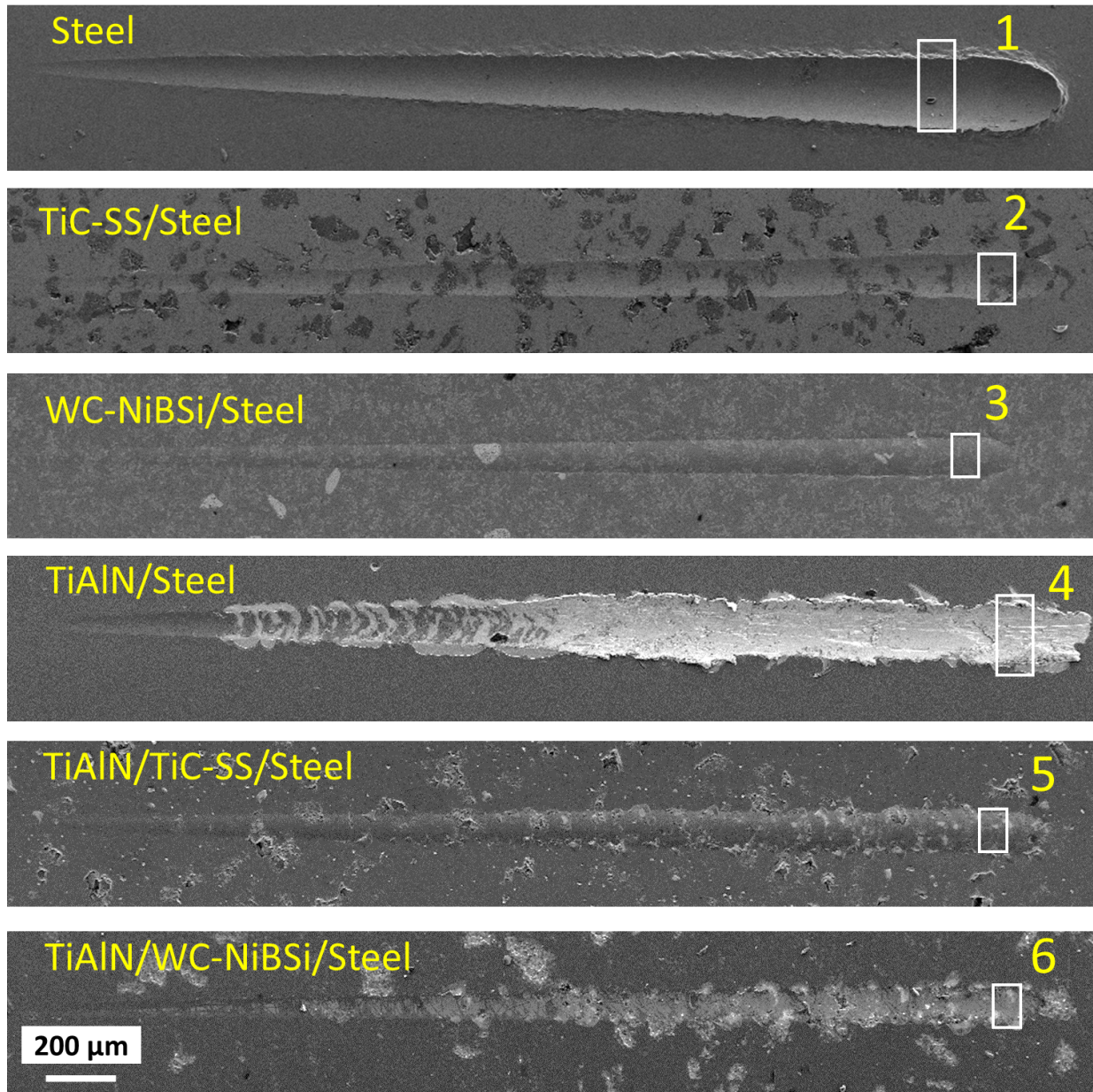


Fig. 21. (a)

(b)

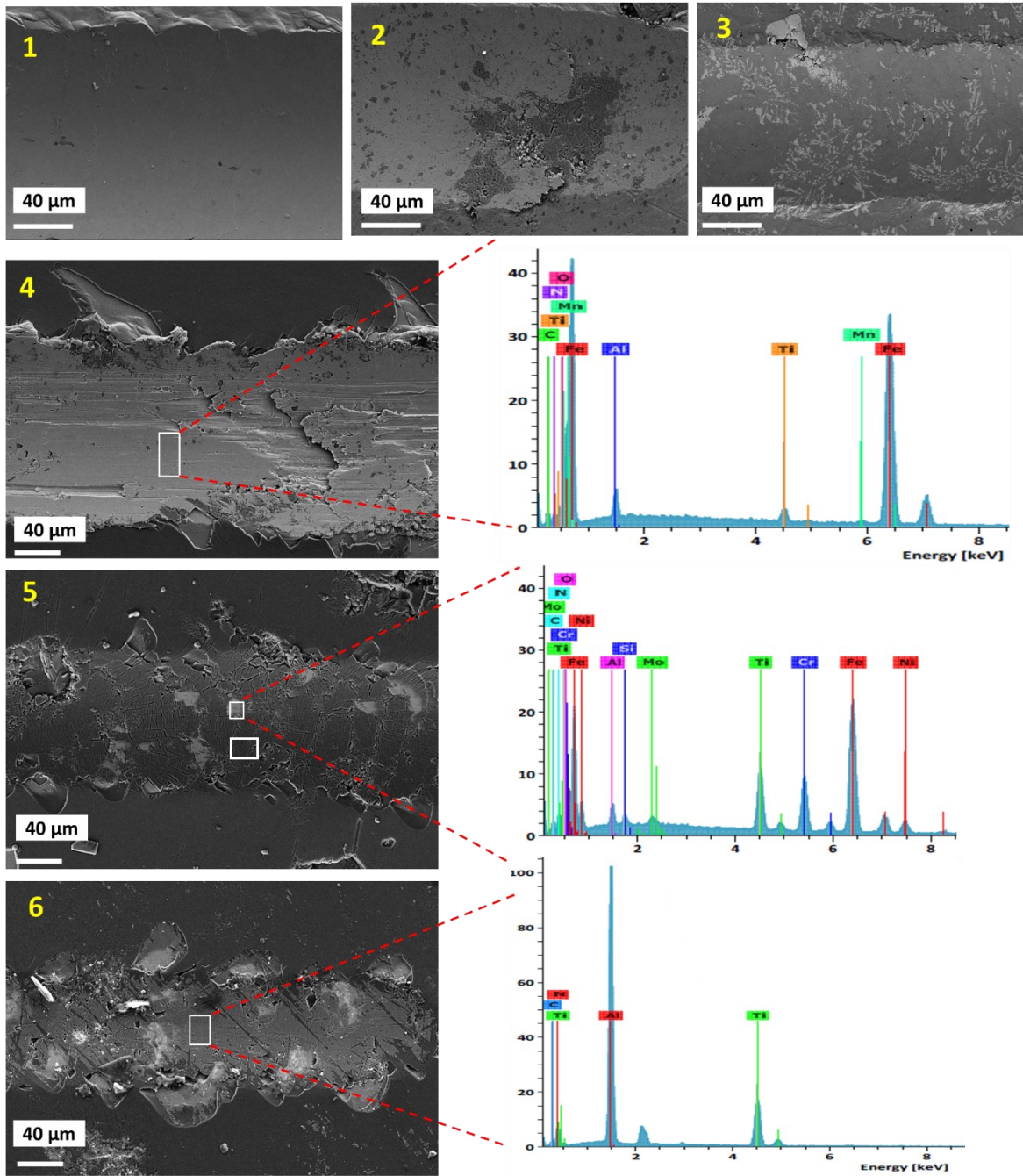


Fig. 21. SEM micrographs (a) for the scratch track of steel, TiC-SS/steel, WC-NiBSi/steel, TiAlN/steel, TiAlN/TiC-SS/steel, and TiAlN/WC-NiBSi/steel after the scratch tests and (b) represents the higher magnified images toward the end of the track with the EDS analysis.

4.3 Tribological Testing

4.3.1 Coefficient of Friction

The evolution of the coefficient of friction under reciprocating sliding load at 5N load for 1000, 2000, and 4000 cycles/s against alumina ball is presented in **Fig. 22**. For all the coatings systems, the coefficient of friction rises very quickly before stabilizing. This rapid rise is due to the transition from smaller to larger contact between the mating surfaces (the substrate/coating and counter body). Firstly, sliding wear experiments were done with the bare substrate to observe the friction and wear behaviour. There was an instability in the coefficient of friction value for steel before reaching a stable value of ~ 0.5 which may be due to the ferrous oxide. The instability caused by iron and iron oxides was well investigated by H.J. Noh and H. Jang [85] and they have demonstrated that ferrous particles exacerbated friction stability. They reported that the static coefficient of friction increased because of the stick-slip phenomena and the magnitude of stick-slip depends on the types of ferrous oxide. PTA deposited TiC-SS/steel coating showed a rise in μ value to ~ 0.8 during the initial stage of the rubbing and then a gradual reduction can be observed. The formation of TiO_2 oxide layer, which acts as a lubricant to help reduce friction, may have contributed to the progressive decline in the friction coefficient value to 0.6 [86]. However, the value climbed to roughly 0.75 again, which is believed to be caused by the breakdown of TiO_2 film and the dominance of the Fe_2O_3 layer, which raises the coefficient of friction by the stick-slip phenomena [85]. A similar trend in friction coefficient value was observed for WC-NiBSi/steel coating. For the case of TiAlN/steel coating, the maximal coefficient of friction for TiAlN layer on steel was ~ 0.94 . TiAlN typically has a high coefficient of friction (0.9-1.0 at room temperature), especially in dry environments [87]. After sliding cycles of 50, 27, and 22 for the

total sliding cycles of 1000, 2000, and 4000 respectively at 5N load, the friction coefficient decreased suddenly from ~0.94 to a quite stable value. This sudden decrease in the coefficient of friction is due to the removal of the top TiAlN layer from the steel. It is evident from the optical microscope photographs in **Fig. 23**, that the TiAlN has been fully removed, exposing the fresh steel substrate. TiAlN/steel coating has an average coefficient of friction of 0.72. This suggests that increasing the sliding time accelerates the deterioration of the coating. The TiAlN/steel coating's average coefficient of friction is roughly 0.72 up to about 1800 sliding cycles in **Fig. 22(b)**. The surface of the coatings usually has surface asperities and roughness. Because the rough portions typically smooth out when the surfaces interact and slide against each other, the coefficient of friction value becomes stable [88,89]. After 1800 cycles, the value began to fall further and eventually reached around 0.6, indicating that the interaction of the alumina counter body is primarily with the base material because of the removal of TiAlN layer.

The friction coefficient of TiAlN/TiC-SS/steel duplex coating rapidly declined from 0.9 after roughly 266 cycles, 1494 cycles, and 490 cycles for total sliding cycles of 1000, 2000, and 4000, respectively, then plateaued at 0.7, comparable to TiC-SS/steel coating at 5N load. TiAlN was partially or entirely removed from the TiC-SS surface for 1000 cycles in **Fig. 23**., while TiAlN was fully removed for 2000 and 4000 cycles of loading and unloading which is shown in **Fig. 24** and **Fig. 25**. In the case of TiAlN/WC-NiBSi/steel duplex coating, the friction value suddenly dropped from 0.8 to 0.6 and stabilized at ~ 0.55 for 5N load and 1000 running cycles in **Fig. 22(a)**. This abrupt decline is generally caused by the removal of the top TiAlN layer. However, detailed optical microscope observation of the TiAlN/WC-NiBSi/steel duplex coating revealed that no removal of TiAlN had taken place after 1000 sliding cycles at 5N load in **Fig. 23**. The friction

value in this case in **Fig. 22(a)** towards the end (~ 0.55) is much lower than that of thick WC-NiBSi/steel coating (~ 0.7). This may be due to the alumina film formation that significantly lowers the coefficient of friction. When the sliding cycles are extended to 2000 and 4000, the friction value stabilises at 0.7, identical to the WC-NiBSi/steel coating, due to the complete elimination of TiAlN from the wear track, as seen by optical images (**Fig. 24.** and **Fig. 25.**). When compared to a TiAlN coating on steel with no interlayer, the better performance of the duplex coatings was due to the addition of the thick, hard intermediate layers.

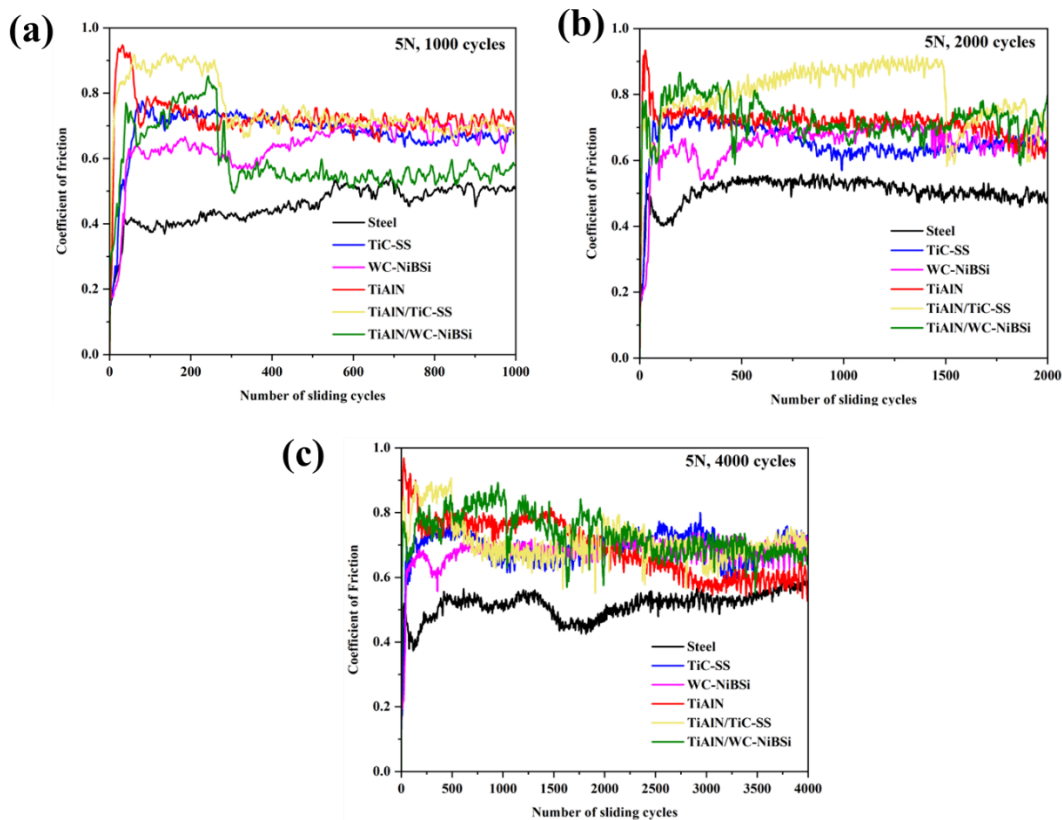


Fig. 22. Coefficient of friction as a function of sliding cycles from the dry sliding tests at 5N load against alumina ball for bare steel, a single layer of TiAlN and TiC- and WC-based coatings, and

their duplex coatings systems on steel under different sliding cycles of (a) 1000 cycles/s, (b) 2000 cycles/s, and (c) 4000 cycles/s.

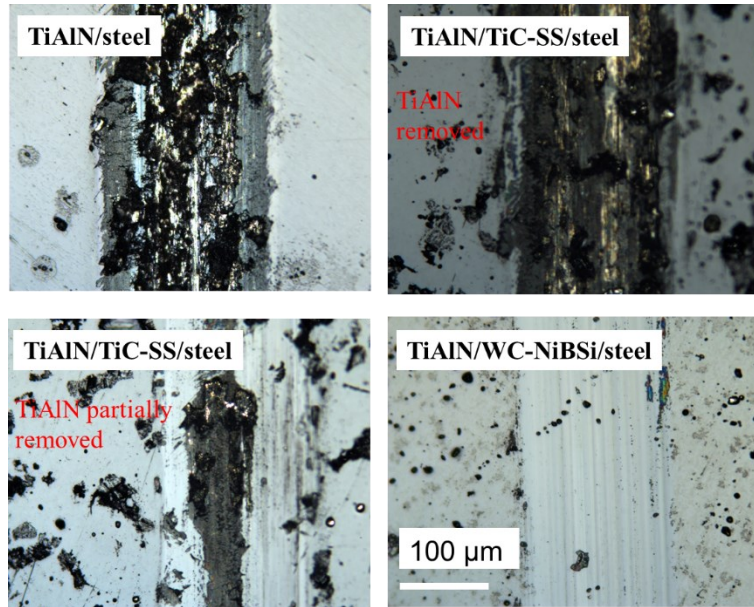


Fig. 23. Optical microscopy images for TiAlN/steel, TiAlN/TiC-SS/steel (partial and full removal of TiAlN top layer), and TiAlN/WC-NiBSi/steel coatings architecture after reciprocating sliding wear experiments at 5N and 1000 cycles (20m of total sliding distance).

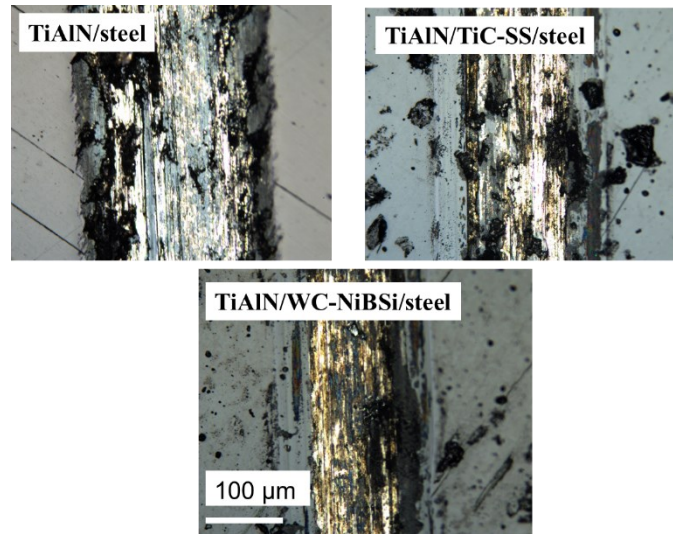


Fig. 24. Optical microscopy images for TiAlN/steel, TiAlN/TiC-SS/steel, and TiAlN/WC-NiBSi/steel coatings after reciprocating sliding wear experiments at 5N and 2000 cycles (40m of total sliding distance).

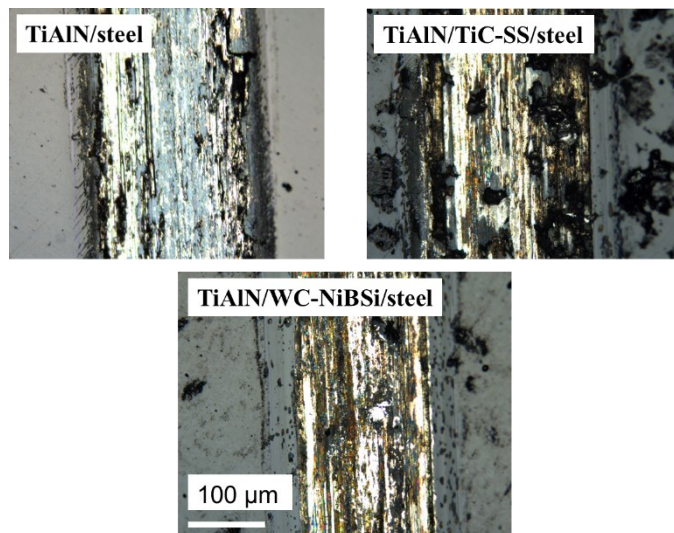


Fig. 25. Optical microscopy images for TiAlN/steel, TiAlN/TiC-SS/steel, and TiAlN/WC-NiBSi/steel coatings after reciprocating sliding wear experiments at 5N and 4000 cycles (80m of total sliding distance).

Another set of sliding wear studies was carried out with a 2N applied force and sliding cycles of 1000, 2000, and 4000, with the results displayed in **Fig. 26**. Because all TiAlN coatings were destroyed with all coating systems and conditions at 5N except TiAlN/WC-NiBSi/steel duplex coating at 5N, 1000 cycles, we chose 2N load at this time to further analyze the wear and tribocorrosion properties. Our goal in this thesis is to apply duplex coatings to more severe tribocorrosion situations than only wear or corrosion. We cannot utilize the coatings for tribocorrosion investigations if the complete removal of TiAlN coating occurs so early in the wear stage since doing so would result in inaccurate tribocorrosion results. In **Fig. 26(a)**, the friction coefficient for pure steel substrate is ~ 0.5 for all 2N conditions. Due to the oxide film formation as described before, the friction behaviour of TiC-SS/steel and WC-NiBSi/steel duplex coating at low load is comparable to that at 5N load. EDS analysis of steel (see **Fig. A1 in Appendix A.**) from inside and outside of the wear track showed the oxygen enrich region inside the wear track while no oxygen outside the track. For TiAlN/steel coating, the friction is flat at ~ 0.9 for 1000 cycles in **Fig. 26(a)** and gradual decrease to a value of ~ 0.8 until 4000 cycles in **Fig. 26(b)** and **Fig. 26(c)**, which may be due to the broken TiAlN films, as seen in the SEM images for 2N, 2000 cycles.

For TiAlN/TiC-SS/steel duplex coating, the coefficient of friction remains at ~ 0.9 for 1000 in **Fig. 26(a)** and 2000 cycles/s in **Fig. 26(b)**, but a rapid drop was found at around 1925 cycles for 4000 cycles/s in **Fig. 26(c)**, indicating TiAlN layer failure owing to repeated loading and unloading, followed by an increasing-decreasing pattern due to the oxide films formed on the surface of the coating. TiAlN/WC-NiBSi/steel coating exhibits a stable value of μ until ~ 2600 cycles and after that, the value suddenly dropped due to the damage of TiAlN layer. For TiC-SS/steel (see **Fig. A1**

in appendix A.), EDS analysis revealed that area 1 inside the wear track had high O and Ti content, whereas region 2 had high O and Fe content. Some regions were rich in O and Fe content for WC-NiBSi/steel. This explains the formation of the tribofilm.

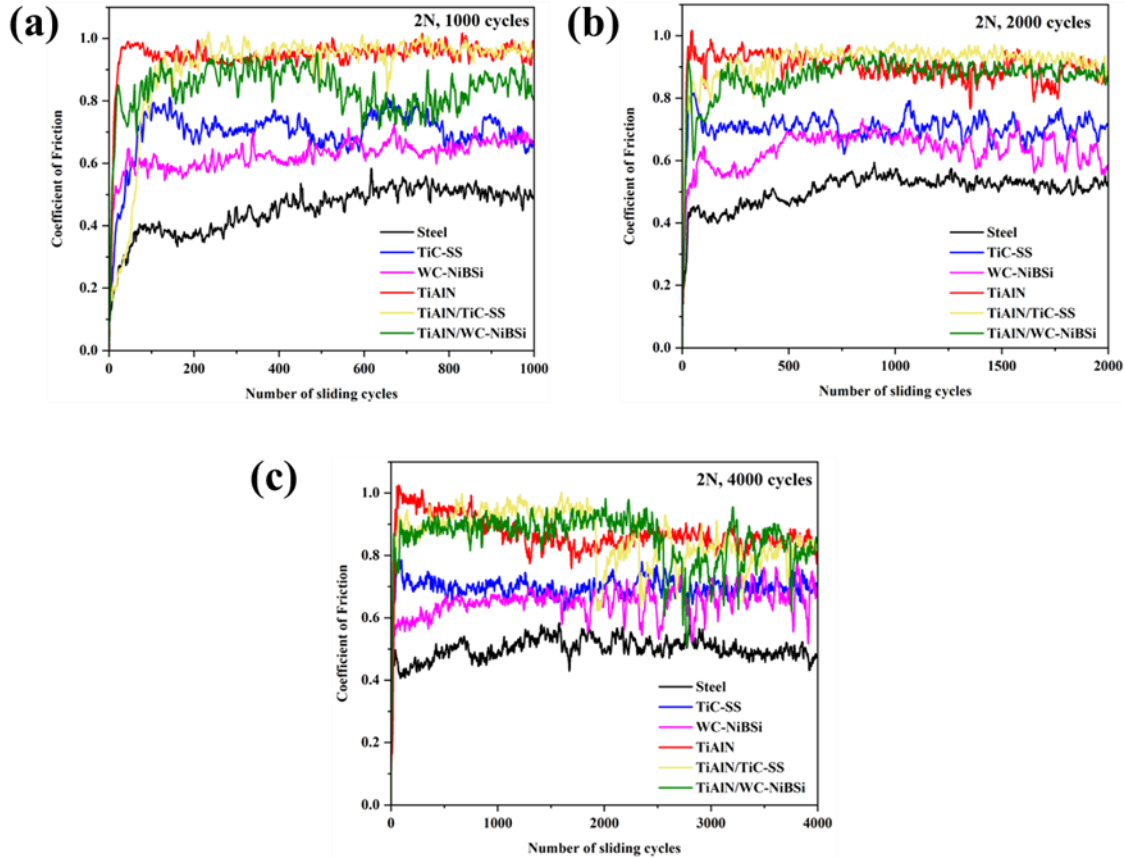


Fig. 26. Coefficient of friction as a function of sliding cycles from the dry sliding tests at 2N load against alumina ball for bare steel, single layer of TiAlN/steel, TiC-SS/steel, WC-NiBSi/steel, TiAlN/TiC-SS/steel, and TiAlN/WC-NiBSi/steel duplex coatings systems under different sliding cycles of (a) 1000 cycles/s, (b) 2000 cycles/s, and (c) 4000 cycles/s.

4.3.2 Wear Rate

Fig. 27. and **Fig. 28.** depict the wear rate, K , of PTA-coated metal matrix composite single-layer coatings and PVD/PTA coated duplex coatings under different sliding cycles (1000, 2000, 4000 cycles) at 5N and 2N applied load, respectively, and corresponding wear properties are shown in **Table 3** and **Table 4**. In the beginning, reciprocating sliding wear experiments were performed for bare steel to compare the wear rate with the coatings. Under 5N load, steel shows good wear resistance even after 1000, 2000, and 4000 sliding cycles despite having a low hardness, which might be attributed to the high toughness of hot rolled steel. In addition, because the worn materials were piling up on the wear track, it was difficult for the profilometer to measure the volume loss from the wear track, resulting in a low value of wear rate. In some of the regions of the wear track, positive wear depth or positive volume was obtained (see **Fig. B1. in Appendix B**). The TiC-SS/steel coating and WC-NiBSi coating showed a very low rate of wear under all the load conditions until 4000 sliding cycles where WC-NiBSi coating exhibited superior performance which is attributed to the high hardness and high wear resistance of WC. L. Du et al. [90] showed that the inclusion of hard particles into the composite coating can significantly improve wear resistance and reduce the coefficient of friction. So, the hard phase WC particles with the NiBSi improved wear resistance significantly in this study. In the case of TiAlN/steel coating, the wear rate increases from $59.18 \pm 10.06 \times 10^{-6} \text{ mm}^3\text{N}^{-1}\text{m}^{-1}$ to $71.1 \pm 6.33 \times 10^{-6} \text{ mm}^3\text{N}^{-1}\text{m}^{-1}$ when the sliding time is increased from 1000 to 2000 cycles under 5N load in **Table 3**, but it decreases when the sliding time is increased further. This decrease in wear rate after 4000 cycles for both load conditions is believed to be because of the complete removal of the TiAlN layer. Under 5N load, the TiAlN layer is broken down early in less than 50 cycles and removed completely after 1000

cycles from steel as evident from optical micrographs (see **Fig. 23.**) and the average material removal of $5910 \mu\text{m}^3$ in **Fig. 29.** with a wear track depth of $\sim 4 \mu\text{m}$ which is higher than the TiAlN coating's thickness ($2 \mu\text{m}$). A large amount of material ($\sim 8300 \mu\text{m}^3$) in **Fig. 29.** was removed at 1000 to 2000 cycles. This significant material loss occurs in the case of TiAlN/steel coatings as a result of third-body abrasion, with TiAlN particles acting as the third body. When TiAlN particles encounter steel and counter body, it accelerates wear rate by removing more material. However, material removal slowed at 2000 cycles to 4000 cycles (from $14210 \mu\text{m}^3$ to $16650 \mu\text{m}^3$ volume loss), which is approximately 3.5 times less than material removal at 1000 cycles to 2000 cycles. As a result, the wear rate for 4000 cycles was lower than 1000 or 2000 cycles as the alumina interacts with the steel substrate with little or no TiAlN particles interacting as a third body because of the complete removal of TiAlN. Nonetheless, the TiAlN/steel coating performed worst under high-stress situations. The poor wear resistance of TiAlN/steel coating, especially under high load is related to the brittle failure of TiAlN and poor adhesion. The volume loss for steel, TiAlN/steel coating, TiC-SS/steel coating, WC-NiBSi/steel coating, TiAlN/TiC-SS/steel duplex coating, and TiAlN/WC-NiBSi/steel duplex coating is shown in **Fig. 29.**

In this study, TiAlN was added on top of steel, TiC-SS/steel coating, and WC-NiBSi/steel coating to improve the wear resistance of the intermediate layer. In general, the addition of the top layer increases the wear resistance of the substrate and of the intermediate coatings [13]. However, for TiAlN/TiC-SS/steel and TiAlN/WC-NiBSi/steel duplex coatings, the wear resistance of both coatings was lower than that of single layer coatings of TiC-SS/steel and WC-NiBSi/steel coatings. Hence, the addition of top TiAlN cannot improve the wear resistance further. This may be because of the poor adhesion of TiAlN with the TiC-SS/steel and WC-NiBSi/steel coatings. Although the duplex coatings exhibit lower wear resistance, they improve the fracture strength of TiAlN as no

brittle failure was seen from SEM micrographs (see **Fig. 21.**) of the duplex coatings when an interlayer was added demonstrating the duplex system improves the load-bearing capacity of the top TiAlN layer when compared to TiAlN/steel coating.

Under 2N load in **Fig. 28.**, PTA WC-NiBSi/steel coating outperformed all the coatings in wear resistance under all the sliding cycles. TiC-SS/steel coating also showed good wear resistance against alumina balls under sliding loading and unloading. However, TiAlN/TiC-SS/steel showed a slightly higher wear rate compared to TiAlN/steel as the hardness of TiAlN/TiC-SS/steel coating is lower than TiAlN/steel. The volume loss at 2N load in **Fig. 30.** is quite similar except 4000 cycles for TiAlN/steel regardless of the interlayer used.

Table 3: Wear rate of PTA and PVD deposited single and duplex coatings obtained after dry sliding tests using 5N load and 4.75 mm diameter alumina counterpart.

Sample	Wear rate, K ($\times 10^{-6} \text{ mm}^3\text{N}^{-1}\text{m}^{-1}$)		
	1000 cycles/s	2000 cycles/s	4000 cycles/s
Steel	0.48 ± 0.14	4.67 ± 1.96	4.38 ± 0.51
TiC-SS/steel	5.56 ± 0.43	5.69 ± 0.12	5.75 ± 0.36
WC-NiBSi/steel	0.31 ± 0.15	2.6 ± 0.54	3.94 ± 0.35
TiAlN/steel	59.18 ± 10.06	71.1 ± 6.33	41.64 ± 1.09
TiAlN/TiC-SS/steel	29.29 ± 13.01	30.98 ± 3.24	31.05 ± 1.69
TiAlN/WC-NiBSi/steel	15.32 ± 0.93	20.35 ± 4.56	22.14 ± 1.03

Table 4: Wear rate of PTA and PVD deposited single and duplex coatings obtained after dry sliding tests: 2N load, 4.75 mm diameter alumina counterpart.

Sample	Wear rate, K ($\times 10^{-6} \text{ mm}^3\text{N}^{-1}\text{m}^{-1}$)		
	1000 cycles/s	2000 cycles/s	4000 cycles/s
Steel	0.48 ± 0.1	1.74 ± 0.32	5.48 ± 1.53
TiC-SS/steel	3.55 ± 0.24	5.05 ± 0.15	5.71 ± 0.29
WC-NiBSi/steel	0.2 ± 0.03	1.81 ± 0.58	4.34 ± 0.28
TiAlN/steel	38.96 ± 2.43	38.47 ± 0.7	26.77 ± 0.89
TiAlN/TiC-SS/steel	45.45 ± 1.25	49.3 ± 0.8	44.15 ± 2
TiAlN/WC-NiBSi/steel	32.59 ± 0.78	38.22 ± 1.09	42.39 ± 0.52

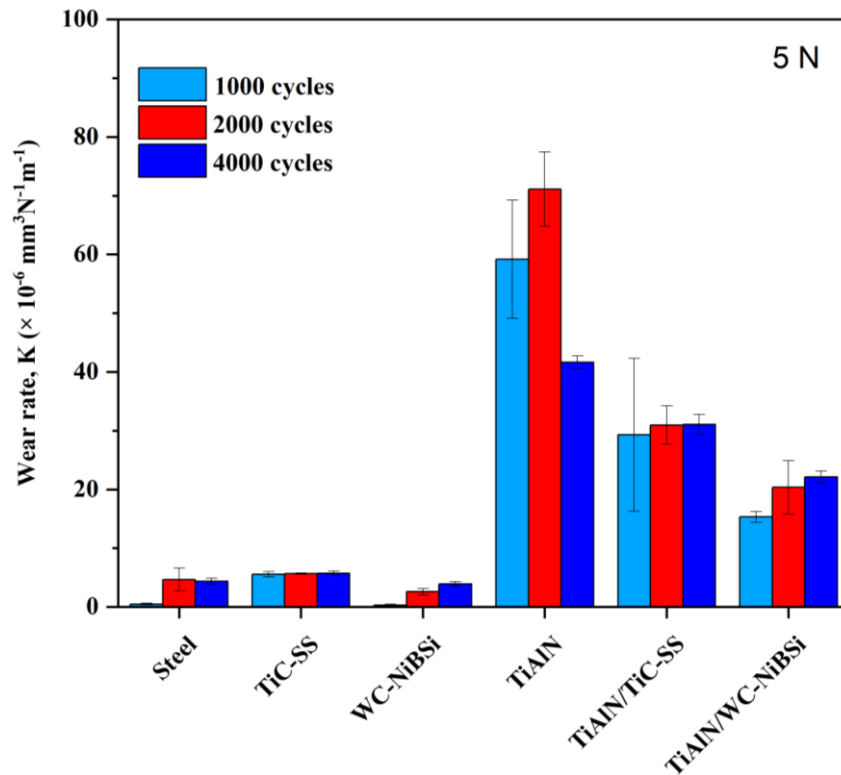


Fig. 27. Wear rates of the fabricated coatings and the steel substrate as a reference, under 5N load.

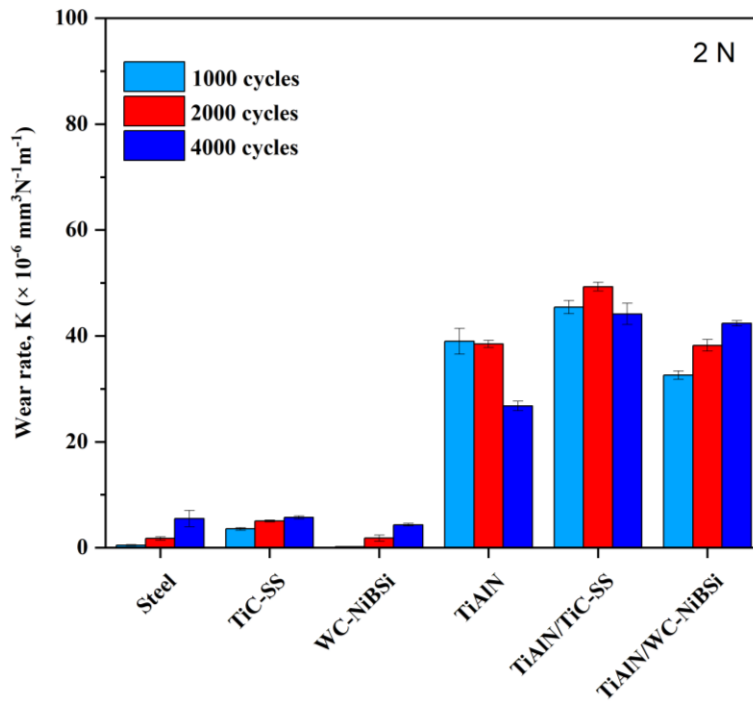


Fig. 28. Wear rates of the fabricated coatings and the substrate as reference under 2N load.

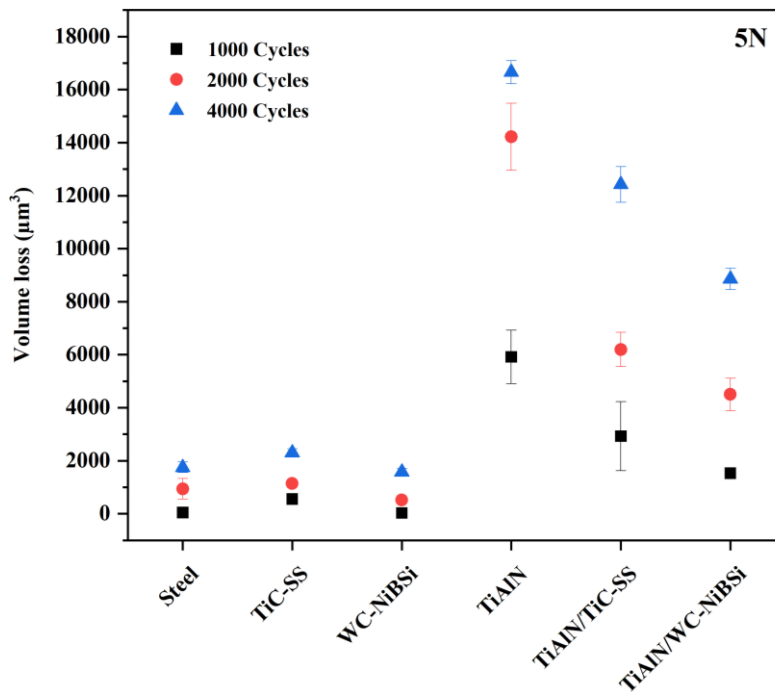


Fig. 29. Volume loss during sliding wear for 5N load.

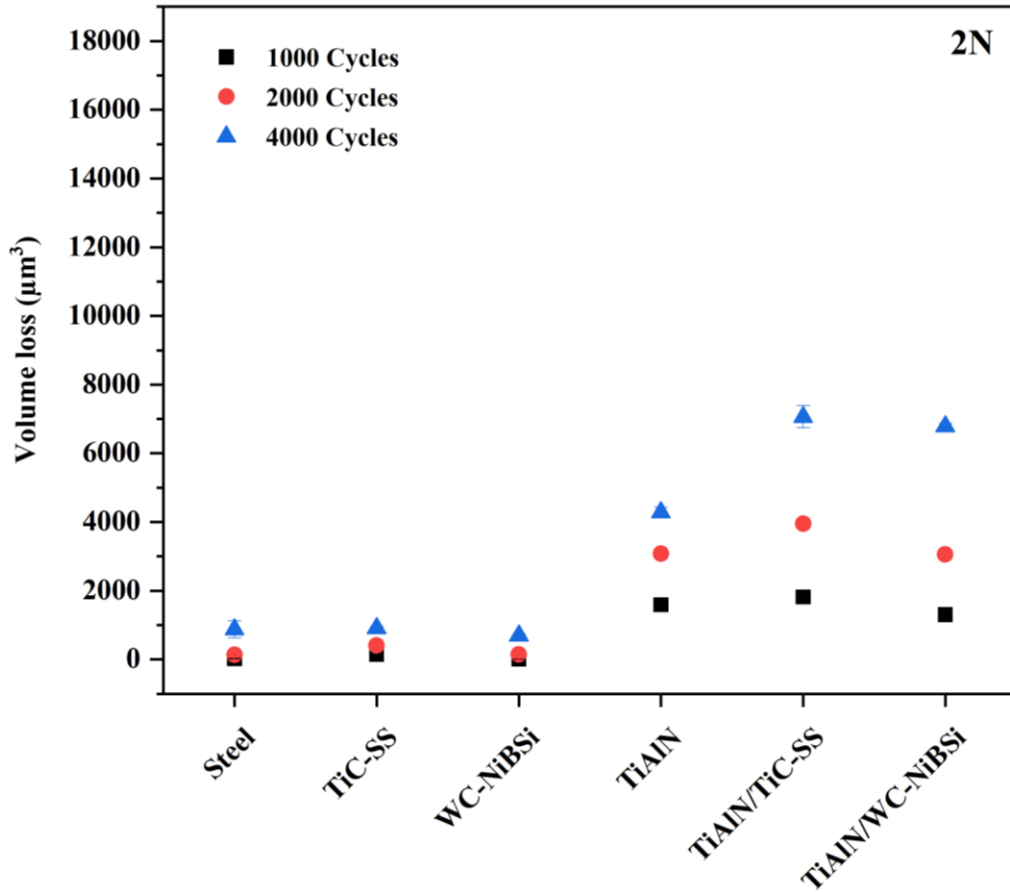


Fig. 30. Volume loss during sliding wear for 2N load.

4.4 Corrosion

4.4.1 Open Circuit Potential (OCP)

The electrochemical potential state of a material using electrolytes over time can be understood effectively through OCP measurements. OCP is the equilibrium potential between the working electrode and the electrolyte which is measured by using a reference electrode. When this equilibrium potential is recorded, the circuit is open, so there is no current flowing and no external voltage is applied. As a result, when a component is in a corrosive environment, the OCP

accurately portrays the real corrosion behavior. The evolution of the OCP of the steel substrate, a single layer of TiC-based and WC-based coatings, and their duplex coatings with the top TiAlN layer exposed to a 3.5% NaCl aqueous solution as a function of time during the corrosion test is presented in **Fig. 31**. The value of the OCP for the coatings stabilized at the end of the 3600s OCP measurements indicating a steady state condition of the surface of the coating has been reached during the electrochemical evolution. However, a gradual decrease of potential from -0.42 V to -0.72 V was observed for the case of the bare substrate which indicates the poor corrosion behavior of fresh steel. This behavior may be related to the early breakdown of the oxide layer which was formed to protect the surface during the attack of Cl^- ions. The OCP for TiAlN coating on steel and WC-NiBSi on steel slightly decreased because of the presence of surface defects and has a marginal difference in the corrosion resistance of TiAlN/Steel and WC-NiBSi/Steel coatings. However, when TiAlN is added on top of WC-NiBSi as a duplex layer coating, the potential is stabilized though it has initial instability (potential dropped from -0.22 V to -0.33 V) until about 300s due to the presence of the defects on the surface. Then it was stabilized at a potential -0.34 V meaning duplex TiAlN/WC-NiBSi can protect steel under a chloride environment that led to significant improvement of its corrosion resistance in compared to the TiAlN or WC-NiBSi coatings alone. On the other hand, TiC-stainless steel composite coating showed a noble behavior under corrosive attack maintaining a stable open circuit potential at -0.04 V. But the addition of TiAlN on top of TiC-SS could not improve corrosion resistance further rather decreased the corrosion resistance compared to TiC-SS coating because of the poor corrosion behavior of TiAlN. However, in comparison with the TiAlN/steel coating, TiAlN/TiC-SS/steel coating exhibited better performance which is attributed to the superior performance of TiC-SS interlayer.

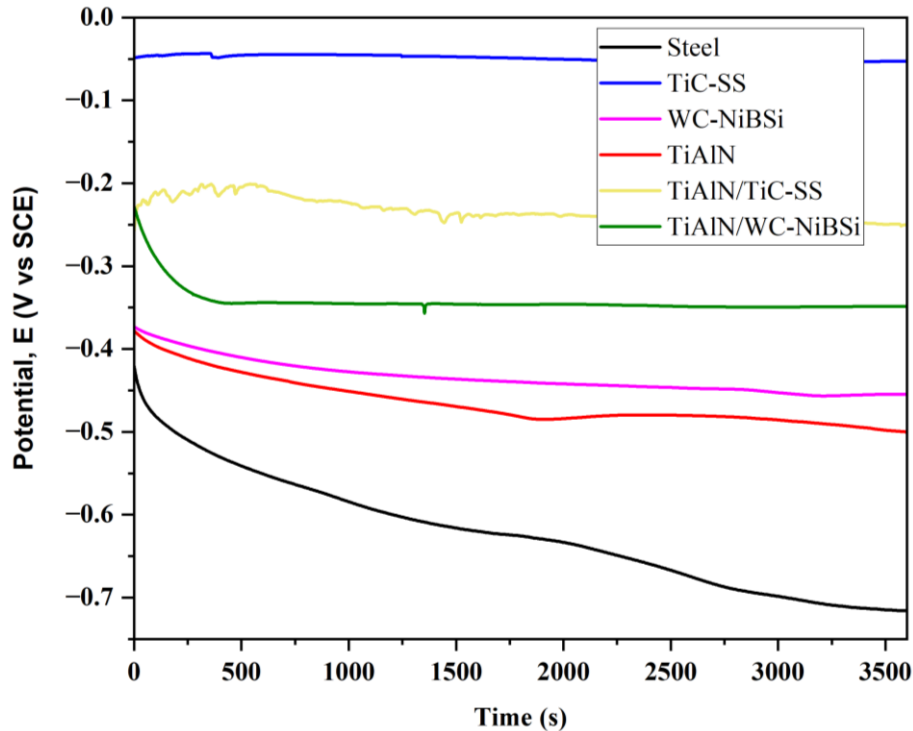


Fig. 31. The evolution of OCP during corrosion test.

4.4.2 Electrochemical Impedance Spectroscopy (EIS)

The Nyquist plots for bare substrate, single layer coatings, and duplex coatings are shown in **Fig. 32.** and corresponding corrosion properties from Nyquist plots are presented in **Table 5.** Nyquist plot for each coating revealed a distinct capacitive loop. The greater the radius of the loop, the higher the corrosion resistance. The radius of the semi-circular arc is very low in Nyquist plots meaning steel is very susceptible to corrosion. The preferential absorption of chloride ions causes the passive layer to rupture, which increases steel corrosion [20]. The higher corrosion resistance of TiC-SS was demonstrated by the fact that the radius capacitive loop is extremely large, in fact,

a straight line in this coordinate which is due to the high corrosion resistance of both TiC and SS. The properties obtained from Nyquist plot are presented in **Table 5**. The TiC-SS/steel coating has a high polarization resistance due to the fewer active sites. The incorporation of the TiC decreases the active site by decreasing the pore resistance and hence increasing the corrosion resistance. It can be deduced that the inclusion of TiC into the SS matrix exhibited enhanced corrosion resistance by reducing active sites in the SS matrix due to the inertness of TiC, inhibiting the pores, and limiting the migration of Cl^- ions toward the substrate [91]. The polarization resistance increased 3.5 times than steel when TiAlN was added on the top of steel. However, the surface defects with the increased surface-active sites allowed more Cl^- ions to infiltrate which increased the corrosion process. SEM images showed rupture and cracks after corrosion. For duplex TiAlN/TiC-SS/steel, polarization resistance is lower than the TiC-SS/steel coating. On the other hand, the polarization resistance for TiAlN/WC-NiBSi/steel was more than 4 times higher than WC-NiBSi/steel coating.

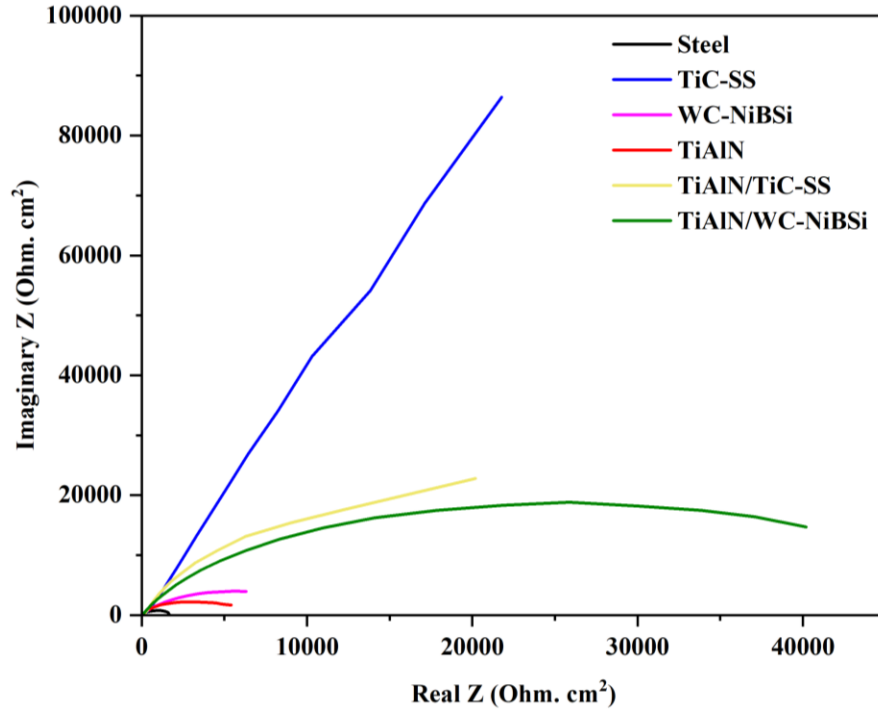


Fig. 32. Nyquist plots for bare steel, single layer coatings, and duplex coatings.

Table 5: Corrosion properties obtained from electrochemical impedance spectroscopy (EIS)

Nyquist plots results.

Samples	R_s (Ω cm^2)	R_p (Ω cm^2)	C (F/cm^2)	n	W (Ω cm^2)
Steel	35	1814	3.8×10^{-4}	0.85	
TiAlN/steel	35	6300	3×10^{-4}	0.8	
TiC-SS/steel	47	2123000	1.4×10^{-4}	0.89	7×10^{-4}
WC-NiBSi/steel	49	11400	5.8×10^{-4}	0.78	
TiAlN/TiC-SS/steel	44	35800	3.9×10^{-4}	0.99	1×10^{-3}
TiAlN/WC-NiBSi/steel	43	48700	7.3×10^{-5}	0.83	

4.4.3 Potentiodynamic Polarization

Potentiodynamic polarization curves for the bare substrate, PTA-coated single thick layer coatings, and PVD/PTA-coated duplex layer coatings are presented in **Fig. 33**. The electrochemical parameters obtained from the Potentiodynamic polarization curve are in **Table 6**. While comparing the corrosion potential and corrosion current of uncoated steel and coated steel (single and duplex coatings), it is clear that the coated steels have a nobler corrosion potential than the uncoated steel. The corrosion potential for steel is -0.71 V while TiC-SS has a corrosion potential of -0.16 V. This indicates that the corrosion potential of steel has moved towards positive corrosion potentials as a result of the addition of layer(s), implying that coatings can shield steel from corrosion. However, various coatings provide varying amounts of corrosion protection in a NaCl environment. Duplex coatings on steel have been created to improve the corrosion resistance of steel. Initially, thick PTA-coated single TiC-SS and WC-NiBSi composite coatings were fabricated on steel, followed by a PVD layer of TiAlN for duplex coatings. Furthermore, thin TiAlN layers were deposited on steel to assess corrosion characteristics. However, Thin TiAlN cannot provide much corrosion protection, since SEM micrographs (see **Fig. 18.**) for TiAlN show that they have some number of flaws on the surface through which chloride ions may permeate and rapidly destroy the steel. The corrosion current of TiAlN coating is comparable to that of steel (2.4×10^{-6} A/cm² for TiAlN and 2.8×10^{-6} A/cm² for steel). Single TiC-SS layer, on the other hand, shows the highest corrosion resistance with the lowest corrosion current (2×10^{-8} A/cm²) due to the good corrosion resistance of stainless steel and TiC. The corrosion resistance of TiC-SS coating is two order of magnitude or 140 times higher than bare steel substrate. However, the addition of the top TiAlN layer on TiC-SS coating does not increase the corrosion resistance of

TiC-SS and instead worsens it. The corrosion resistance of TiAlN/TiC-SS/steel duplex coating exhibits approximately 13 times higher increase in terms of corrosion current when compared with TiAlN/steel single layer coating alone, despite the fact that the enhancement cannot be achieved for TiAlN on TiC-SS duplex systems. Here, it can be stated that the intermediate thick TiC-SS coating has a significant influence on the corrosion of the top TiAlN layer since a single layer of TiAlN on bare steel showed poor corrosion behaviour. Though TiC-SS/steel single layer coating displayed excellent corrosion resistance, WC-NiBSi/steel single layer coating revealed comparably low corrosion resistance due to probable galvanic cell formation between the WC and NiBSi phases. Interestingly, the addition of the TiAlN layer increased the performance of the WC-NiBSi coating by breaking the galvanic cell while shifting the corrosion potential from -0.49 V for WC-NiBSi/steel coating to -0.37 V for TiAlN/WC-NiBSi/steel coating and lowering the corrosion current roughly 4.5 times compared with WC-NiBSi coating, and 14 times compared with steel.

Table 6: Corrosion current and corrosion potential from potentiodynamic polarization curve.

Samples	E_{corr} (V)	$I_{\text{corr}} (\times 10^{-6} \text{ A/cm}^2)$
Steel	- 0.71	2.8
TiAlN/steel	- 0.54	2.4
TiC-SS/steel	- 0.16	0.02
WC-NiBSi/steel	- 0.49	0.93
TiAlN/TiC-SS/steel	- 0.28	0.18
TiAlN/WC-NiBSi/steel	- 0.37	0.2

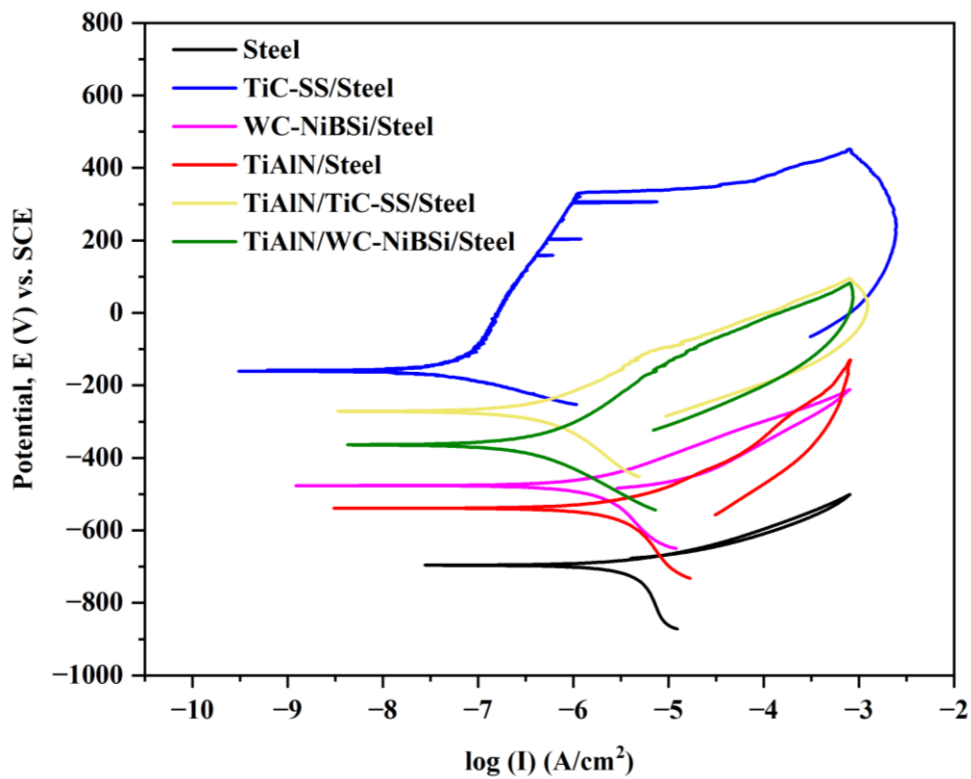


Fig. 33. Potentiodynamic polarization curve for bare steel and single layer, and duplex coatings.

Finally, the corrosion resistance of the coatings in aqueous sodium chloride solution is as follows, based on the OCP, EIS, and Potentiodynamic polarisation for corrosion results: TiC-SS/steel single layer coating > TiAlN/WC-NiBSi/steel duplex coating > TiAlN/TiC-SS/steel duplex coating > WC-NiBSi/steel single layer coating > TiAlN/steel thin single layer coating > steel substrate.

4.5 Tribocorrosion

4.5.1 Wear at OCP

Sliding tests and OCP measurements are done concurrently for tribocorrosion testing to analyze the tribocorrosion performance of the substrate and coatings. First, a steady OCP is achieved before sliding against an alumina counterpart to quantify tribocorrosion at OCP for 3600s. A change in OCP may be noticed during sliding to determine if the mechanism is active or passive.

Fig. 34. depicts the evolution of the OCP before, during, and after sliding wear in the NaCl environment for bare steel and coatings. For bare steel, OCP decreased gradually for the first hour before sliding wear started, then suddenly increased when rubbing began, which may have been brought on by the development of a tribo-film on the surface. The continued rubbing on the surface, however, is causing the tribo-layer to deteriorate as evident by the reduction in OCP once more, and repassivation cannot happen once rubbing is stopped since the steel surface will have completely degraded owing to the simultaneous action of wear and corrosion. In the case of TiAlN/steel, the Al_2O_3 is formed on the surface and the friction decreases after 4700s (see **Fig. 35.**), with stable potential. However, after 5475s, this thin Al_2O_3 started to be removed and TiAlN was broken down due to the continuous rubbing action and the friction is increasing and repassivation was not possible when the rubbing was stopped. Interestingly, WC-NiBSi/steel coatings showed a very similar pattern in their potential behaviour. On the other hand, when the reciprocating motion was stopped, all other coatings, including the two duplex coatings, showed repassivation. The potential was very stable during the rubbing action, indicating that the TiC-SS/steel coating has good corrosion resistance. However, when the TiAlN layer was removed through repeated loading and unloading, the chloride ions attempted to reach the TiC-SS layer, as

evidenced by the sudden decrease in potential value. However, once the absorption of chloride ions was equilibrated, no more ions could infiltrate, causing the potential to rise again and then re-passivated during the last hour when there was no sliding action.

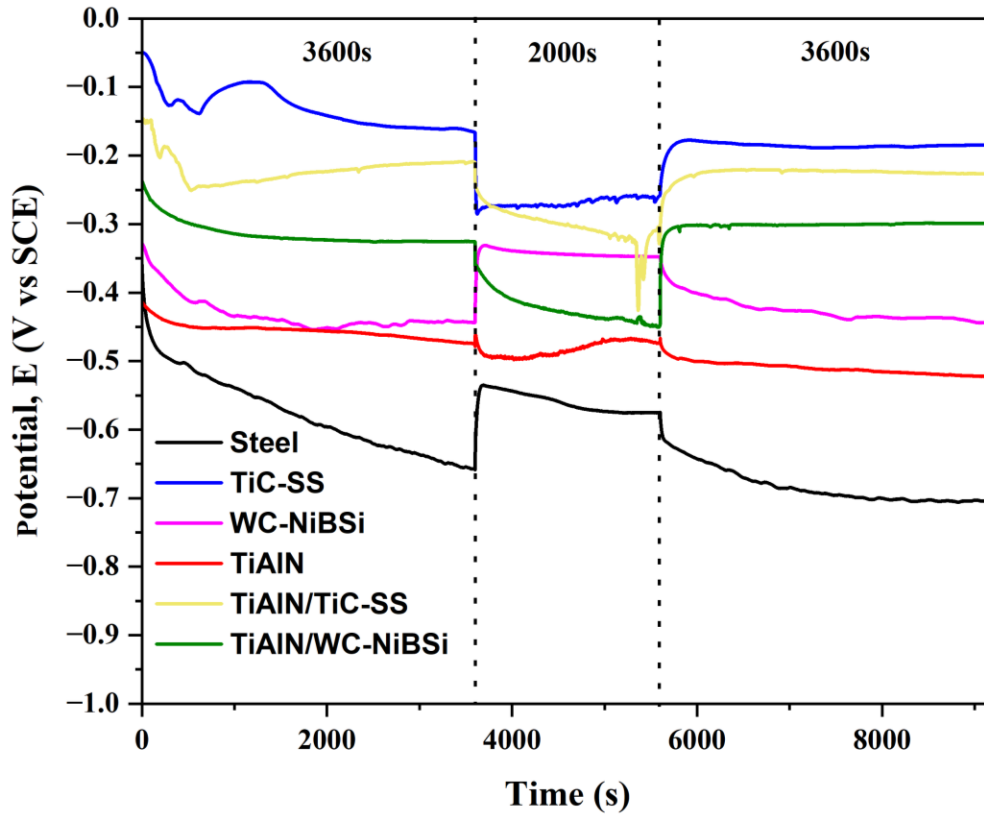


Fig. 34. OCP measurements during tribocorrosion tests at 2N, 2000 cycles/s.

The corresponding coefficient of friction after the tribocorrosion tests at OCP is shown in **Fig. 35**. As sliding movement stopped in the first and last 3600s, no friction values were recorded during those times. In wet sliding, the values of μ for steel, TiC-SS/steel coating, and WC-NiBSi/steel coating were much lower than in dry sliding. This is due to the lubricant action of NaCl aqueous

solution. However, TiAlN-based coatings had no lubrication effect in duplex coating because the μ value was similar to that of dry conditions.

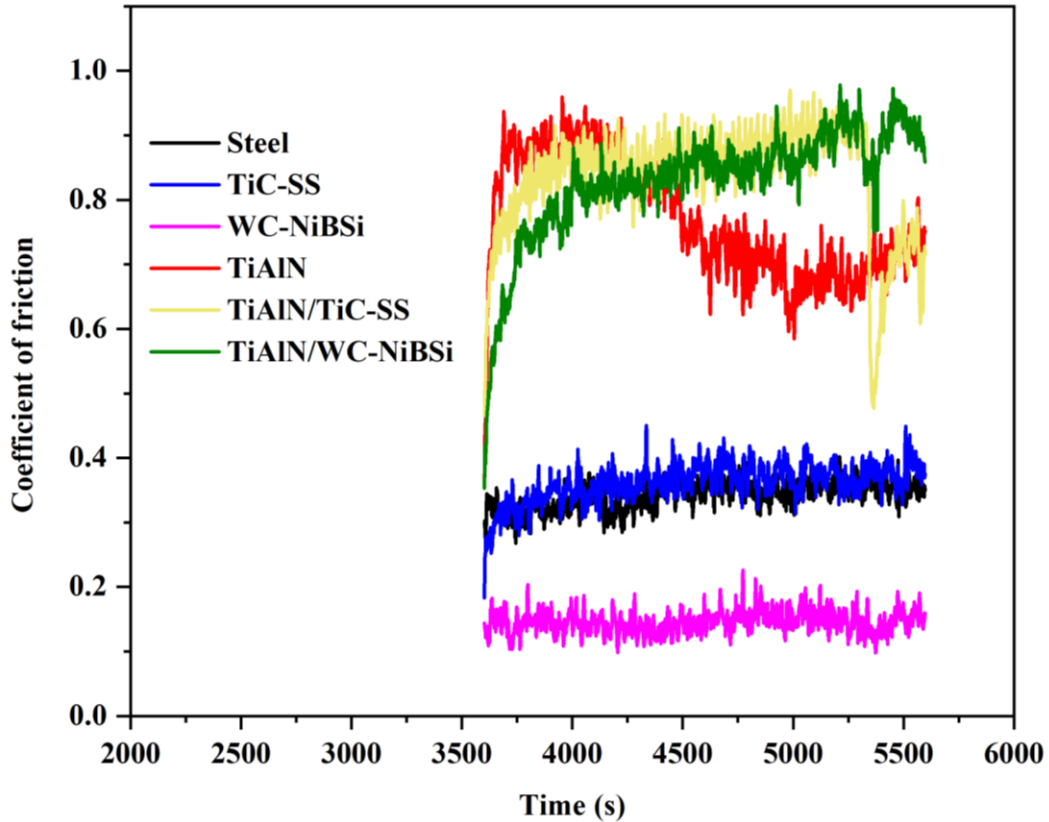


Fig. 35. Coefficient of friction obtained during tribocorrosion tests at OCP for 2N, 2000 cycles/s.

The wear rate obtained from the tribocorrosion experiments under OCP is displayed in **Fig. 36**. Thick single layer TiC-SS/steel and WC-NiBSi/steel coatings showed low wear rates, indicating that wear has less of an impact on tribocorrosion. Furthermore, TiC-SS/steel demonstrated superior tribocorrosion resistance. The WC-NiBSi/steel coating, on the other hand, is susceptible to

corrosion. The addition of TiAlN degraded the surface further, possibly due to the abrasion of TiAlN particles, resulting in increased wear rates.

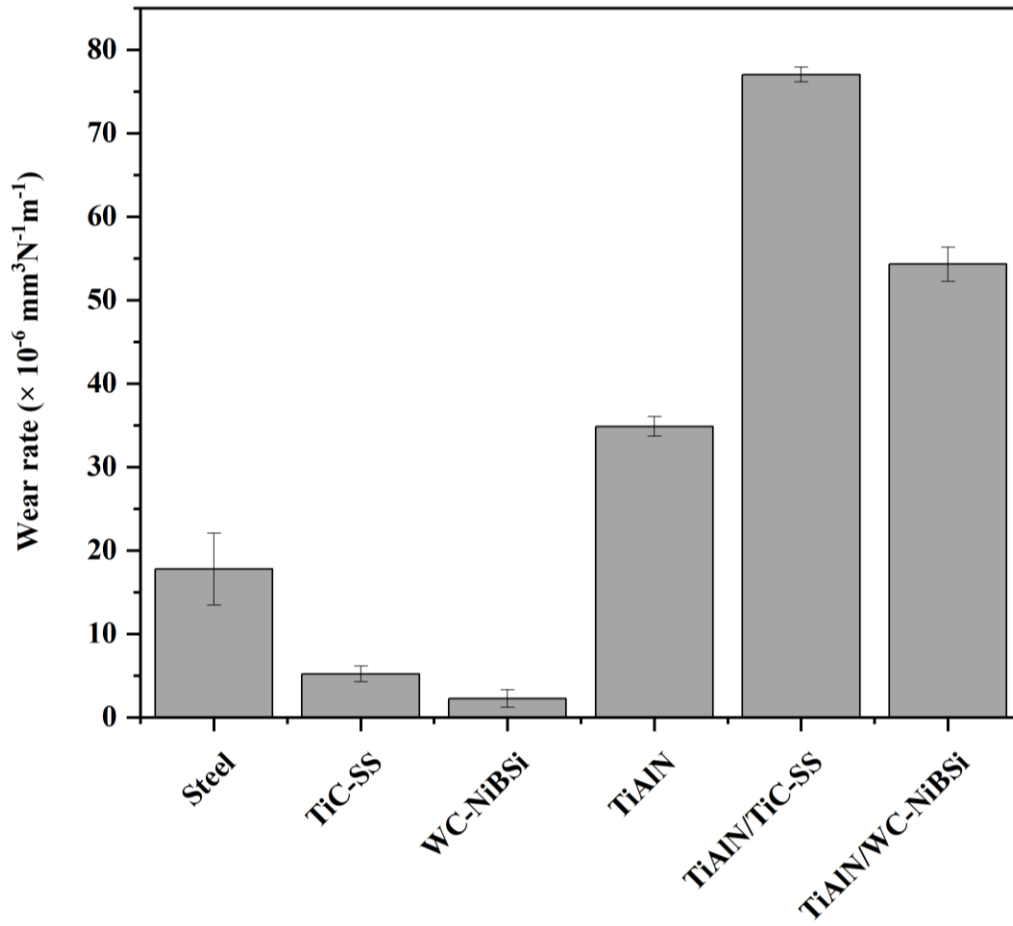


Fig. 36. Wear rates of different coatings during tribocorrosion tests at OCP for 2N, 2000 cycles/s.

4.5.2 Potentionstatic Wear

Fig. 37. depicts the OCP for the bare steel and coatings during tribocorrosion under potentiostatic polarization. The OCP stabilized for 3600s, followed by a 2000s region with a 2N load and a 0.2V external potential relative to the OCP, resulting in a flat line in the curve. The adsorption of Cl^- ions caused the OCP of the bare substrate to gradually approach its lowest level. On the other hand, the creation of metastable pits and repassivation caused the possibility of TiAlN/steel and WC-NiBSi/steel specimens to exhibit fluctuating behaviour [92].

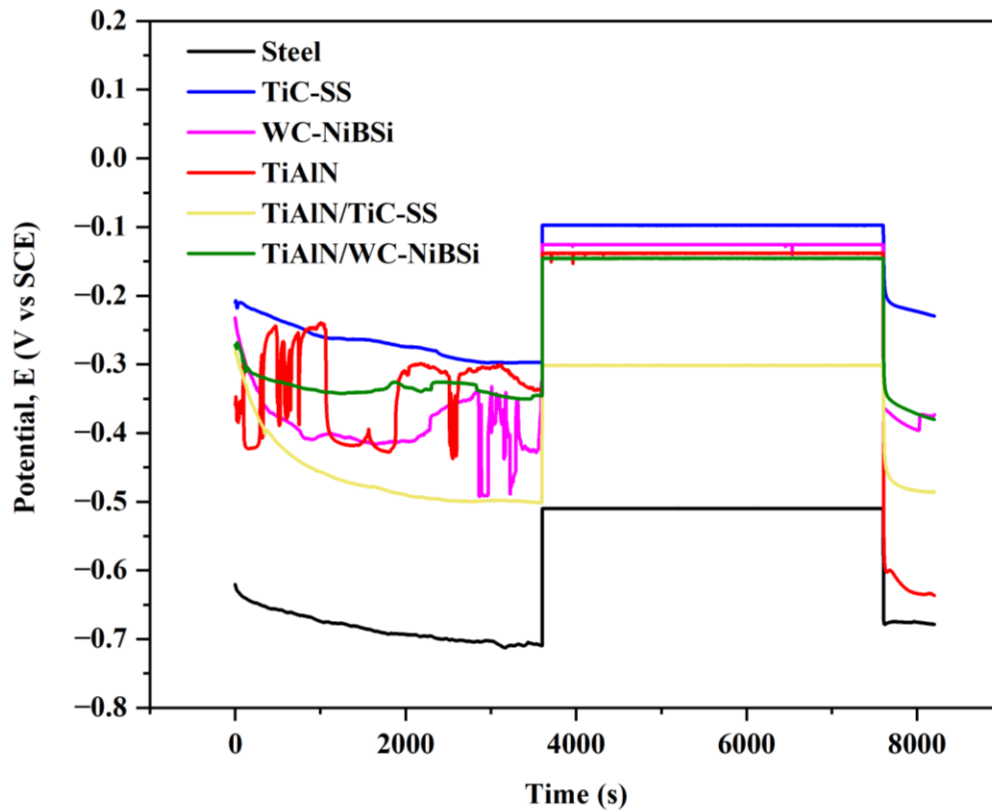


Fig. 37. OCP measurements during tribocorrosion tests under potentiostatic polarization at 2N, 2000 cycles/s.

Fig. 38. depicts the time-dependent behavior of the corrosion current during a tribocorrosion test with potentiostatic polarisation. The sliding wear tests at 2N and 2000 cycles/s were done under 3.5 wt.% NaCl aqueous solution where 0.2V vs OCP external potential was applied. For all coatings, no current was recorded for a period of 3600s during the OCP measurement. Before the start of the wear test, the corrosion current for TiAlN/steel coating was fluctuating (up to 2 mA) because chloride ions in NaCl were trying to reach the substrate through the defects that TiAlN coating surface had. Similar results were obtained for the WC-NiBSi/steel coating, where the corrosion current increased to 3.5 mA during 1000s. In contrast to WC-NiBSi and TiAlN coatings, an addition of TiAlN layer on WC-NiBSi/steel coating results in a negligible current increase. For the case of TiC-SS/steel coating in **Fig. 38(b)**, an entirely flat line except for some fluctuations in current was observed during the same period with a corrosion current of 10 μ A, whereas a higher value (actually decreasing from 60 μ A to 50 μ A) of corrosion current was recorded when TiAlN coating was added to TiC-SS coating compared to single layer TiC-SS coating. Based on this observation, it can be concluded that alumina oxide layer was formed during the OCP measurements to protect the surface of the pure TiAlN/steel coating and then the protective layer was broken. For WC-NiBSi/steel coating, the oxide layer is gradually broken down. A passive layer, on the other hand, protects the surface of the single TiC-SS/steel coating and the duplex coatings of TiAlN/TiC-SS/steel and TiAlN/WC-NiBSi/steel.

When rubbing began, the current for the TiAlN coating gradually increased until the wear test ended. This is because the TiAlN coatings are worn away as can be seen from the SEM micrographs (see **Fig. 41.**) as a result of the continuous loading and unloading with alumina ball and the infiltration of chloride ions toward the fresh steel through the worn part. In the case of

WC-NiBSi coating, the corrosion current steadily rises until 3.5 mA as the passive film deteriorates. After that, the corrosion current dropped until the wear test was completed. Three assumptions can be made to favour this evolution which is as follow: i) the passivation of the WC-NiBSi surface, which occurred as a result of the formation of aluminum oxide that was transferred from the Al_2O_3 counterpart, ii) the closure of pores as a result of the mechanical action of the counter body, and iii) the oxidation of the substrate, which occurred after significant infiltration of the electrolyte into the coating to the substrate. However, the aluminium oxide tribolayer was broken down as the current increased very rapidly during the last 1000 cycles when the wear tests stopped, causing further material degradation. For the duplex TiAlN/WC-NiBSi/steel coating, an increase in current was observed throughout the wear cycle for 2000s, which could be due to the gradual removal of the TiAlN layer and exposure of fresh WC-NiBSi layer caused by the continuous rubbing action. As soon as rubbing ceased, the current leveled off gradually, possibly because an aluminium oxide tribolayer formed to further protect the WC-NiBSi coating from the attack of chloride ions. Among all of the coatings, the TiC-SS coating demonstrated the best performance when subjected to the synergistic effect of wear and corrosion. The recorded corrosion current is low compared to the corrosion current of all other coatings. Although TiAlN coating cannot improve the corrosion and wear further when it is applied on top of TiC-SS coating, the overall performance of duplex TiAlN/TiC-SS/steel coating is higher than the single TiAlN coating. In the absence of any delamination of the TiAlN layer, the corrosion current is low (60 μ A), but once the layer is worn off due to constant rubbing, the current spikes to 140 μ A. This delamination of the TiAlN layer occurred after 1600 cycles of rubbing, which can be explained by the sudden rise in current shown in **Fig. 38.** and the drop in friction value shown in **Fig. 39.** However, after the removal of the TiAlN layer, the fresh TiC-SS coating was then exposed to the

wear and corrosive medium at which point corrosion current decreased, and a steady current was observed when the wear stopped. This may be related to the decrease of active areas on the surface as a result of re-passivation. Finally, it can be said that although further improvement was not achieved with the duplex TiAlN/TiC-SS/steel coating compared to TiC-SS/steel coating, TiAlN improved the performance when a harder intermediated layer was added than the soft steel substrate.

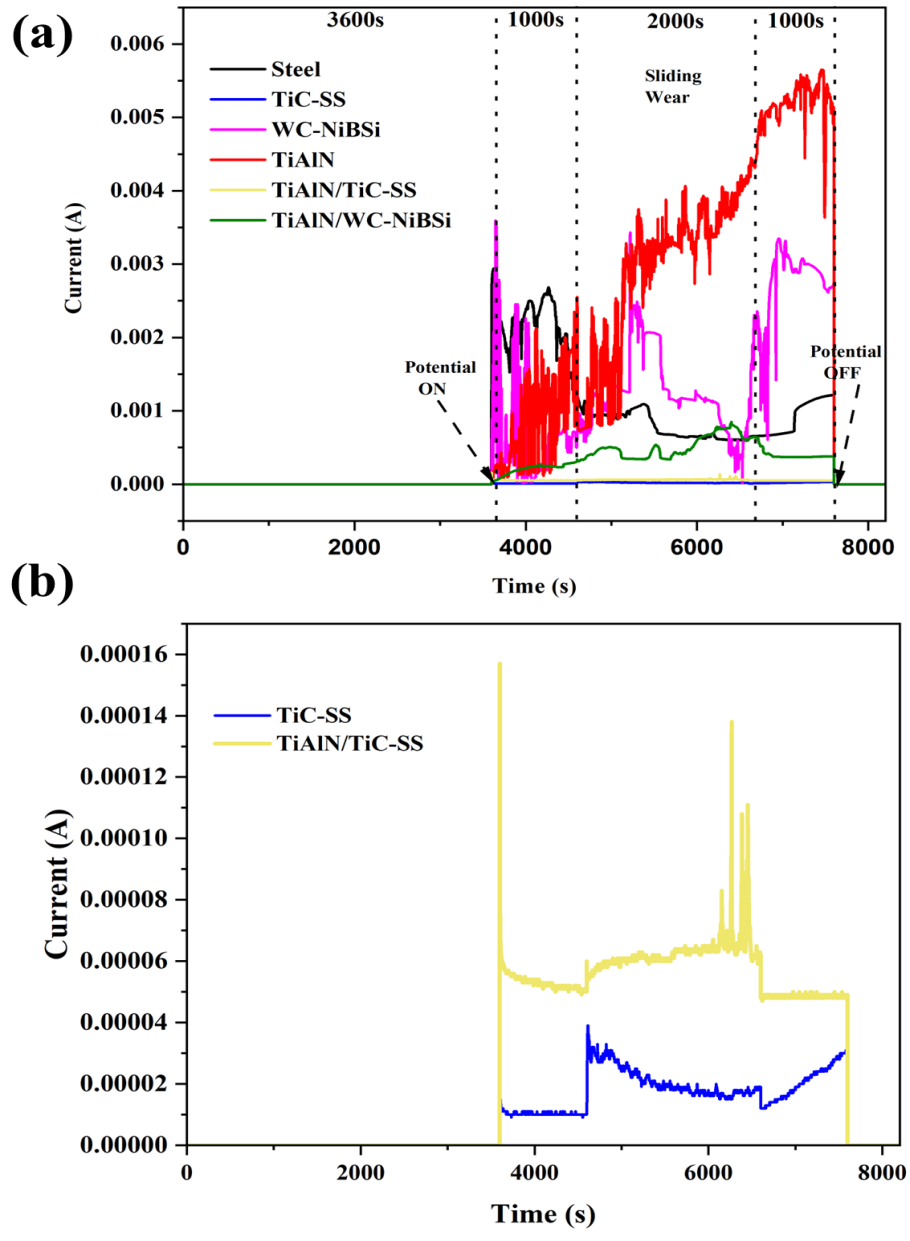


Fig. 38. Corrosion current measurements after the tribocorrosion at potentiostatic polarization for (a) steel, TiC-SS/steel coating, WC-NiBSi/coating, TiAlN/steel coating, TiAlN/TiC-SS/steel duplex coating, and TiAlN/WC-NiBSi/steel duplex coatings and (b) zoomed-in image for TiC-SS/steel coating and TiAlN/TiC-SS/steel duplex coating with 2N, 2000 cycles/s load and 0.2V external applied potential.

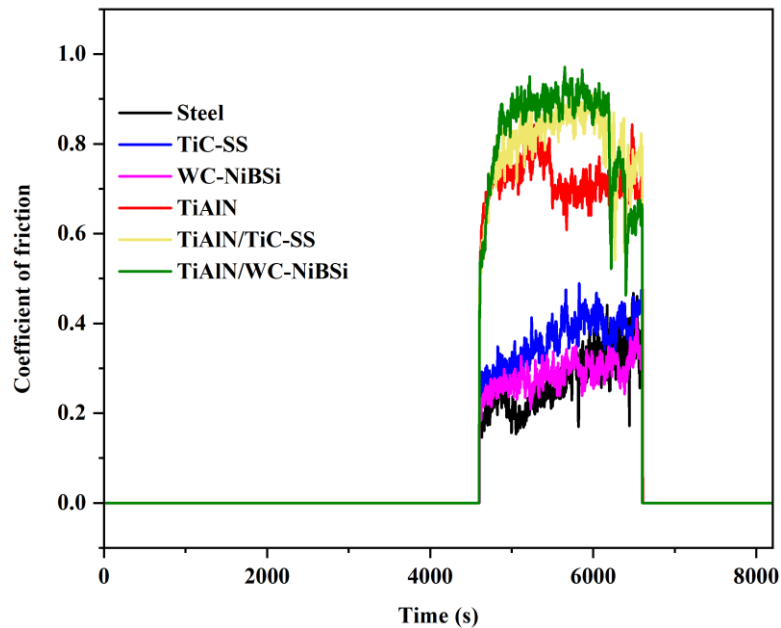


Fig. 39. Coefficient of friction obtained during tribocorrosion tests at potentiostatic polarization.

Fig. 40. depicts the wear rate after the tribocorrosion tests under potentiostatic polarization. Compared to the results of all other tests (dry sliding, corrosion, tribocorrosion at OCP conditions), the wear rate increased for each sample in this case. This is because increasing the environment's severity by adding external potential and the imposed load damages the coating's surface more. For TiAlN/steel coating, the wear rate rose by nearly 2.5 times compared to dry sliding tests at 2N, 2000 cycles. Due to the applied external potential and the load, the coating's surface underwent severe torturing. SEM micrographs of the TiAlN surface show the rupture, fractures, and large pores that were caused by that torture on the surface. The WC-NiBSi coating had the lowest wear rate, however, the surface suffered severe damage in tribocorrosion. The addition of TiAlN layer accelerated the wear rate by the formation of a galvanic cell between TiAlN and WC-NiBSi. On

the other hand, TiC-SS/steel coating also performed well under the torture with a relatively low wear rate. Despite the absence of galvanic cell formation, the wear rate was greater than that of TiC-SS/steel coating due to the elimination of the TiAlN layer. When compared to TiAlN/steel, TiAlN/TiC-SS/steel performed better, demonstrating the load-bearing capacity of the intermediate hard TiC-SS coating.

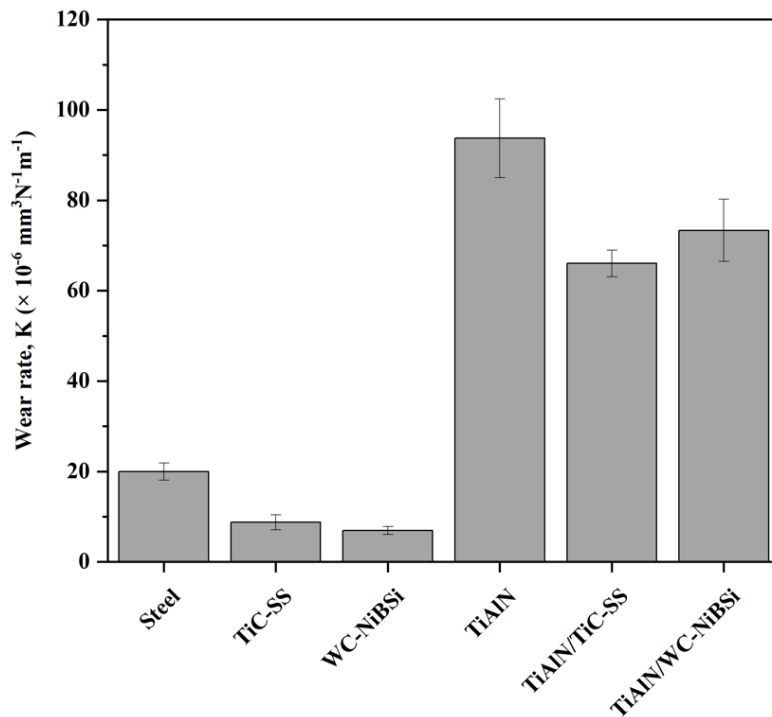


Fig. 40. Wear rate during tribocorrosion tests under potentiostatic polarization for 2N load for 2000 cycles and 3.5 wt.% NaCl solution.

4.6 Degradation Mechanism

4.6.1 During Dry Sliding

SEM micrographs of tribological behaviour under dry sliding conditions of 2N load with 2000 cycles of reciprocating movement by an alumina ball are presented in **Fig. 41**. for the bare substrate (steel), single layer coatings on steel (TiAlN/steel, WC-NiBSi/steel, and TiC-SS/steel), and duplex coatings on steel (TiAlN/WC-NiBSi/steel and TiAlN/TiC-SS/steel). For the bare steel substrate in **Fig. 41(a)**, the formation of oxides occurred in different regions in the wear track. The surface developed fractures because of the oxides being broken down by the continuous loading and unloading of the sliding movement, suggesting oxidative wear occurred on the surface of the steel. This resulted in more wear when the newly exposed steel contacted the counter body. On the wear track, sticky patches were seen, indicating an adhesive form of wear. Evidence of delamination within the wear track was seen by inspecting the top surface of the worn area of the steel. During the wear test, the hard Al_2O_3 ball subjected the sample's surface to alternating tensile and compressive stresses, which likely resulted in the formation of fractures in the vicinity of the contact region. The appearance of cracks and debris in SEM image of the void indicates that the material was removed by delamination. Abrasive wear is evident by the appearance of cracks, micro-cutting on the surface, and dispersed wear debris. In contrast, the hard thin film of TiAlN in **Fig. 41(d)** on the soft steel substrate showed lower tribological performance. The wear track of the TiAlN/steel coating displays curved cracks usually at 45° to the sliding direction, which can be attributed to the brittle nature of the nitride and the soft nature of the steel substrate. The cracks can initiate at the interface between the soft substrate and hard TiAlN during the loading and unloading and then propagate throughout the surface [13].

As demonstrated by the reciprocating sliding wear test, the WC-NiBSi coating offers superior wear resistance to any other coating tested. The micrograph of the WC-NiBSi/steel coating in **Fig. 41(c)** clearly shows some oxidation because the sliding movement raises the temperature of the track and promotes oxidation on the track [1]. This oxide acts as a lubricant reducing wear significantly at lower sliding cycles. Micro-cracks and deformation of WC particles, on the other hand, can be seen where some cracks propagated towards the relatively softer NiBSi matrix. Even though some of the oxides are broken and some cracks are propagated, no debris from those broken oxides or fragmented WC particles were found in the wear track, which could act as a third body to deteriorate the wear further. P. Niranatlumpong and H. Koiprasert [37] investigated the microstructure of NiCrBSi–WC and NiBSi–WC coatings prepared by electric arc spraying. During their dry sliding tests, they found that the main reason for higher wear depth for NiCrBSi–WC coating is the detachment of the carbide particles which allowed the softer matrix to expose under loading and unloading causing more rapid wear. Interestingly, no craters due to the WC particles delamination can be seen from the NiBSi matrix during the dry sliding of Al₂O₃ ball in this study due to the strong metallurgical bonding between WC and NiBSi matrix during the alloying process of carbides into the matrix. Therefore, because WC was effectively dissolved into the NiBSi matrix, WC-NiBSi/steel coating exhibited enhanced wear resistance. **Fig. 41(b)** shows the micrograph of TiC-stainless steel coating on steel after dry sliding of 2000 cycles under 2N load. As like WC carbides, TiC also exhibits micro-cracks and propagates toward a softer SS matrix when subjected to sliding under an alumina ball. In addition, some of the TiC particles had partly delaminated, leaving behind traces of wear debris that contributed to more wear. Because of this, the wear rate of the TiC-SS/steel coating was somewhat greater than that of the WC-NiBSi/steel coating. Delamination wear and abrasive wear are the major types of wear mechanism for TiC-

SS/steel coating, as shown by the presence of parallel grooves and plastic deformation on the wear track.

Hard coatings on soft substrates can protect the surface, but if an interlayer is added to strengthen the surface, the coating can protect the surface even better. To further enhance the wear performance, a hard thin layer of TiAlN was placed on the top of thick WC-NiBSi/steel and TiC-SS/steel to produce duplex coating. The wear mechanisms of TiAlN/WC-NiBSi/steel and TiAlN/TiC-SS/steel duplex coatings were comparable, with smooth scratch lines parallel to the reciprocation suggesting a moderate abrasive mechanism of wear. It was also found that the TiAlN/TiC-SS/steel wear track in **Fig. 41(e)** had a patchy structure of TiAlN, suggesting an adhesive wear process. Delamination of the TiAlN coating caused by contact stresses generated by the alumina ball may lead to the appearance of large and tiny voids in the case of TiAlN/TiC-SS/steel, while some smaller voids can be observed in the case of TiAlN/WC-NiBSi/steel duplex coating in **Fig. 41(f)**. In addition, the number of craters on the surface of the TiAlN/TiC-SS/steel coating is higher than that of the surface of the TiAlN/WC-NiBSi/steel coating. These craters were revealed spontaneously as a consequence of TiAlN detachments that occurred during the wear testing. Because of the greater wear depth caused by the bigger voids, the wear rate of the TiAlN/TiC-SS/steel duplex coating is greater than that of the single layer of TiAlN/steel coating or the duplex layer of TiAlN/WC-NiBSi/steel. Additionally, the wear rate of duplex TiAlN/WC-NiBSi coating is higher than the single WC-NiBSi coating but lower than TiAlN coating. Poor adhesion between the thick layer and the thin layer of TiAlN, attributable to either increased roughness of the thick coatings or insufficient optimization of parameters during TiAlN layer fabrication, is responsible for the increased wear rate of duplex coatings.

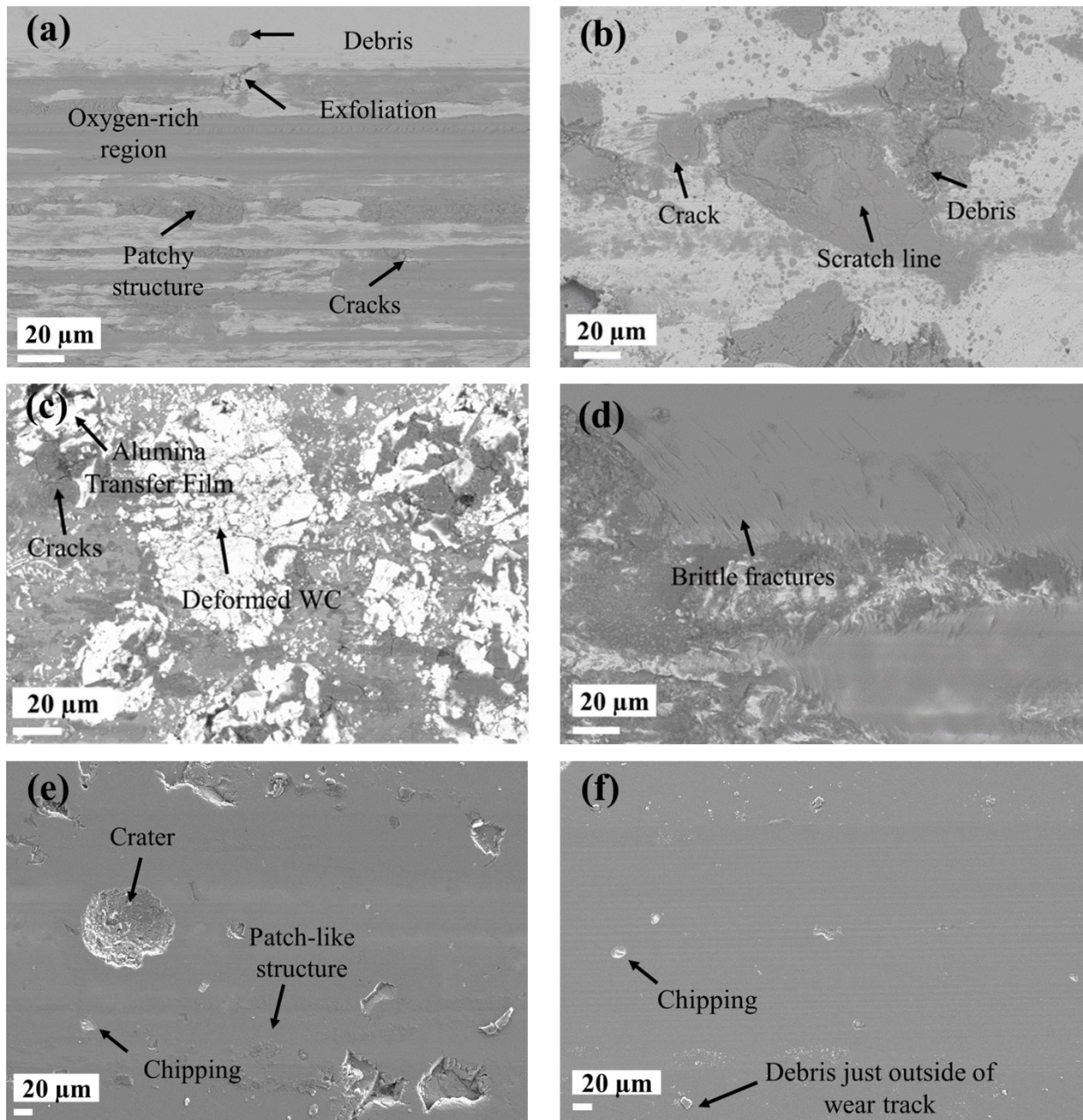


Fig. 41. Worn surfaces of (a) steel, (b) TiC-SS/steel coating, (c) WC-NiBSi/steel coating, (d) TiAlN/steel coating, (e) TiAlN/TiC-SS/steel duplex coating, and (f) TiAlN/WC-NiBSi/steel duplex coating under reciprocating sliding motion of 2N and 2000 cycles/s against alumina ball.

4.6.2 During Corrosion

Fig. 42. displays SEM micrographs of the surfaces of the steel substrate, the PTA/steel coatings, and PVD/PTA/steel coatings after the corrosion tests under 3.5 wt.% NaCl aqueous solution. Corrosion pits and craters can be seen in the substrate's surface morphology (**Fig. 42a**). These pits typically developed because of the breakdown of the passive oxide layer, whereby chloride ions (Cl^-) diffused into the layer and started material dissolution. The surface morphology shows that corrosion products are randomly distributed all over the steel surface. The extent and distribution of corrosion products suggest that the passive film cannot protect the surface of the steel. Because the passive layer that developed on the steel was unable to adequately separate the metal from the corrosive environment, it can be said that untreated steel is incapable of providing effective corrosion protection. For thin TiAlN coating deposited on steel by PVD method (see **Fig. 42(d)**), localized pitting is the corrosion mechanism expected for the failure of the coatings as TiAlN coatings present some defects. Pitting can be initiated by the passage of Cl ions through defects in the protective layer and these ions congregate around the weak points and cause the protective layer to rupture. Local chemical dissolution results from complexes formed by Cl^- anions with the precipitated oxide during this process [93,94]. The cracks generate at the weak points of pits propagate to the surface. TiC is typically well passivated and has a high barrier to electrochemical reactions, whereas stainless steel has superior corrosion properties. As a result, the combination of these two materials provides excellent resistance to corrosion which can be easily seen from the micrographs of TiC-SS/Steel coating in **Fig. 42(b)**. The TiC-SS/steel coating's surface is relatively fresh after the corrosion tests, with no significant matrix dissolution which makes it the best coating for preventing corrosion amongst all the coatings. Additionally, the well-distributed TiC particles in the SS matrix increase pitting resistance by increasing charge transfer resistance [94,95].

However, when TiAlN thin layer is formed on the top of TiC-SS/steel **Fig. 42(e)** some level of surface oxidation occurred on the TiAlN surface, but no pitting or cracks can be seen. For WC-NiBSi/steel in **Fig. 42(c)**, it is obvious that the pits grew bigger because of the dissolution of the WC particles. When the TiAlN is added **Fig. 42(f)**, it prevented the infiltration of chloride ions to seal the pores of WC-NiBSi which enhanced the corrosion resistance of TiAlN/WC-NiBSi/steel compared to single WC-NiBSi coating.

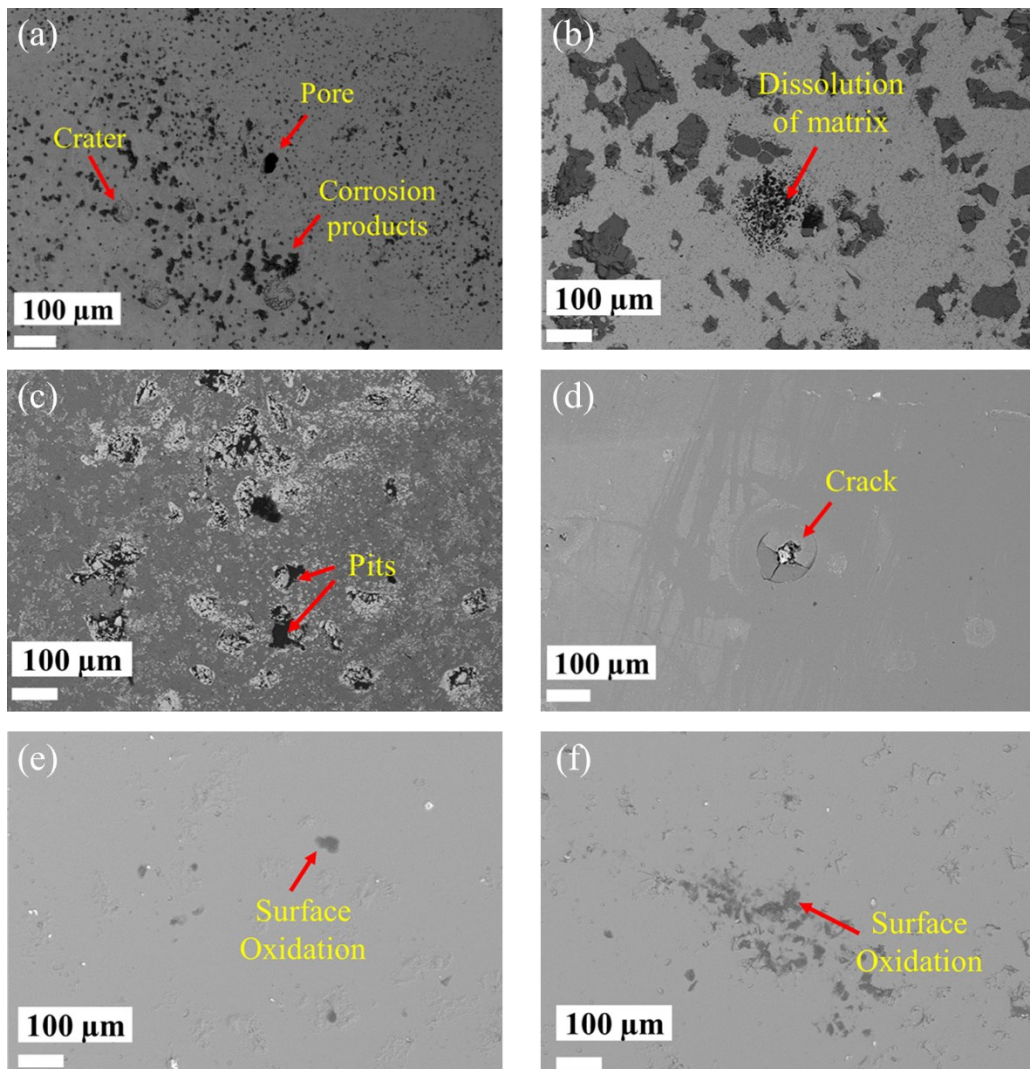


Fig. 42. SEM micrographs for corrosion behaviour of different single-layer and duplex coatings under 3.5 wt.% NaCl solution: (a) steel, (b) TiC-SS/steel coating, (c) WC-NiBSi/steel coating, (d) TiAlN/steel coating, (e) TiAlN/TiC-SS/steel duplex coating, and (f) TiAlN/WC-NiBSi/steel duplex coating.

4.6.3 During Tribocorrosion

Images of typical wear scars by scanning electron microscopy are presented for all samples (steel, TiAlN/steel, WC-NiBSi/steel, TiC-SS/steel, TiAlN/WC-NiBSi/steel, and TiAlN/TiC-SS/steel) subjected to tribocorrosion under OCP conditions in **Fig. 43**. and under potentiostatic polarization conditions in **Fig. 44**. Under OCP conditions, plastic shearing marks on uncoated steel were visible and were oriented in the direction of reciprocating motion of the Al₂O₃ ball counter body in **Fig. 43(a)**. On the wear track and the sides of the wear track, some debris and/or oxide scale formation were seen. However, the frequent loading and unloading caused oxide films to easily crack in the wear track, and eventually, they delaminate, making the steel more vulnerable to corrosion and wear during the tribocorrosion process. For PTA deposited thick TiC-SS/coating in **Fig. 43(b)**, plastic deformation, and crack from hard TiC to softer SS matrix was evident due to the severe interactions with alumina ball. However, these cracks are not through the thickness of the coating. Through-thickness fractures offer quick routes for O₂ and Cl⁻ ions to diffuse inside and penetrate, potentially enhancing oxidation [41]. Furthermore, the tribocorrosion tests with close inspection of the wear track revealed no further fractures in the wear track and no dissolution of the SS matrix, making the TiC-SS/steel coating the best of all the coatings. However, the other thick layer coating, WC-NiBSi/steel in **Fig. 43(c)** cannot show good performance in tribocorrosion under OCP. Pits were seen at the interface of the WC and NiBSi matrix, and corrosion development occurred in

the NiBSi matrix when chloride ions penetrated via the surface defects in the WC-NiBSi coating. Although the surface of the WC-NiBSi/steel coating underwent surface oxidation, it demonstrated higher load support [96,97]. Interestingly, the aluminum transfer occurred during the loading of the alumina ball, and tribo-film of alumina was formed in different regions on the wear track, especially on the valley of the hard WC phase and the deformed area with the alumina ball. Because of the tribo-film formation and the lubrication during the wet wear, the coefficient of friction for WC-NiBSi/steel was low.

On the other hand, for thin TiAlN/steel coating fabricated by PVD in **Fig. 43(d)** for tribocorrosion studies, damaged TiAlN coating in the center of the wear track with pores, cracks, and delamination and some parallel grooves in the direction of reciprocating movement away from the center are characteristic of TiAlN/steel coating's wear under OCP. During the rubbing action, cracks were initiated due to the high contact stresses induced by the alumina ball and propagated to the subsurface, and as a result, the TiAlN was removed via delamination because of this repeated loading and unloading. Because tribocorrosion is the simultaneous action of wear and corrosion, as soon as the wear initiates a surface crack, chloride ions from the aqueous solution congregate near the crack and induce high interfacial stresses, which promotes further cracks and further corrodes the surface.

For TiAlN/TiC-SS/steel duplex coating in **Fig. 43(e)**, the addition of a TiAlN top layer cannot help the TiC-SS/steel coating to increase its wear or tribocorrosion resistance. Complete removal of TiAlN layer can be seen from the SEM images. Wear debris and microcracks can also be observed. As the TiAlN degraded earlier, the broken TiAlN particles interacted with the surface of the

coating and alumina ball via a three-body abrasion mechanism, resulting in a higher wear rate. Interestingly, no rupture or cracks, or brittle fracture due to the interaction of chloride ions and under repetitive load can be observed, indicating an improved fracture strength of TiAlN due to the hard TiC-SS interlayer. No galvanic coupling occurred despite the removal of the top layer. For the TiAlN/WC-NiBSi/steel duplex coating **Fig. 43(f)**, TiAlN coating sustained on the WC-NiBSi/steel coating due to the high bearing capacity of WC-NiBSi under tensile and compressive stress. No cracks were observed from the TiAlN surface. Some parallel groves can be seen along the reciprocating direction. Complete removal towards the end of the wear track and no or partial removal of TiAlN in the middle of the wear track can be observed.

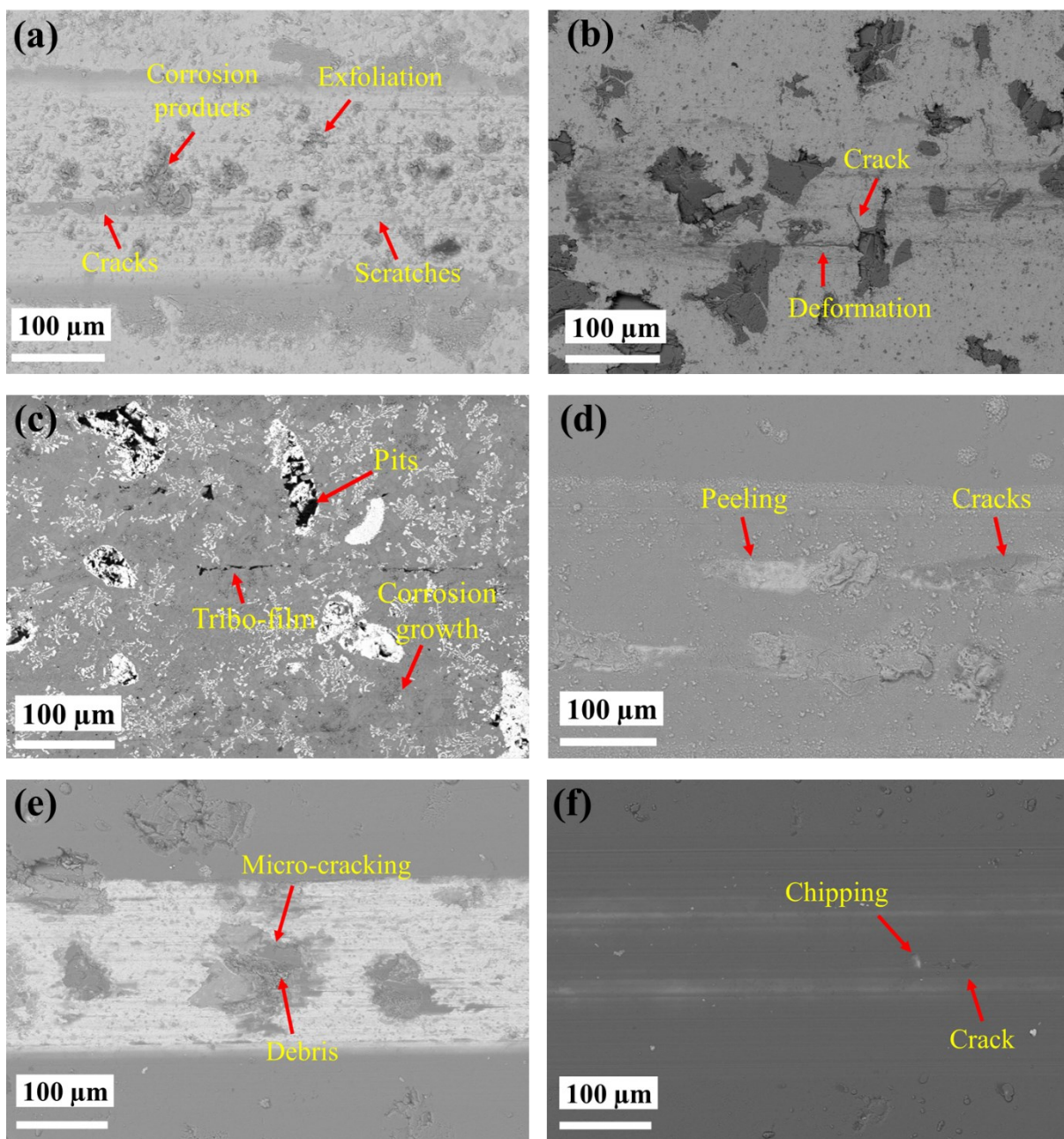


Fig. 43. SEM micrographs for tribocorrosion under OCP conditions at 2N, 2000 cycles load, and 3.5 wt.% NaCl: (a) steel, (b) TiC-SS/steel coating, (c) WC-NiBSi/steel coating, (d) TiAlN/steel coating, (e) TiAlN/TiC-SS/steel duplex coating, and (f) TiAlN/WC-NiBSi/steel duplex coating.

Under potentiostatic polarization conditions in **Fig. 44.**, the degradation of the uncoated steel surface was more pronounced under the action of wear and corrosion where an external potential of 0.2 V was also applied. There were few scratch marks as seen in **Fig. 44(a)** since the wear track was primarily covered by corrosion products. The oxide clusters can be observed on the surface of the steel. Pits and craters of varying sizes could be seen all over the surfaces, indicating that pitting had occurred under the aqueous NaCl medium. Furthermore, wear had weakened the surface near the pits, allowing the pits to grow and leave craters. Under tribocorrosion tests with the applied potential, the TiC-SS/steel coating **Fig. 44(b)**, displayed a very stable performance. Although very few microcracks are visible, they are unable to cause the surface to deteriorate further when wear and corrosion are acting simultaneously due to the excellent corrosion and wear resistance of TiC and stainless steel. In the contrary, WC-NiBSi/steel coating **Fig. 44(c)**, cannot perform well under the corrosive medium while being the best coating under wear studies. The surface of the corroded WC-NiBSi/steel displayed large pits as a result of the continuous growth of pits caused by the interaction of chloride ions. For TiAlN/steel coating, the synergistic mass loss for TiAlN/steel coating is substantially more than the mass loss due to wear or corrosion alone. This could be well understood by the wear rate and careful inspection of the SEM images of the surface of TiAlN/steel after tribocorrosion. The wear rate caused by synergy under potentiostatic polarization is more than twice the rate of dry wear (see **Table 4**) or wear under OCP at 2N, 2000 cycles load and in an aqueous NaCl solution (see **Fig. 36.**). The SEM images for TiAlN/steel coating in **Fig. 44(d)**, displayed cracks, growth of cracks and larger pits on the surface of TiAlN/steel coating. In the case of duplex coating, the wear process accelerated the corrosion process of the TiAlN/WC-NiBSi/steel duplex coating, as shown in the SEM picture in **Fig. 44(f)**, where the TiAlN is completely removed in the center of the wear track but not on the sides. This is because the duplex

coating's surface develops strong galvanic couplings between TiAlN and WC-NiBSi during tribocorrosion testing. Rubbing removes the oxide layer that formed on the surface by repeated sliding motions, leaving a clean surface that is exposed to the electrolyte and stimulates electrochemical activity, resulting breaking down of TiAlN layer. Furthermore, due to the breaking down of the TiAlN coating, TiAlN particles as wear debris inside the wear track acted as abrasive material which accelerated wear more. As a result, more chloride ions accumulated in the center of the wear track to reach the substrate, resulting in a strong galvanic coupling between TiAlN and WC-NiBSi. In contrast, no galvanic coupling was seen in the case of TiAlN/TiC-SS/steel duplex coating in **Fig. 44(e)**, making TiAlN/TiC-SS/steel an acceptable choice for applications involving concurrent wear and corrosion. Pure mechanical removal of TiAlN happened from the surface where corrosion has less of an influence on the surface of the TiAlN/TiC-SS/steel duplex coating's degradation.

In summary, steel is the worst material to be used under tribocorrosion studies where TiAlN addition on steel could not help steel to protect it further from the simultaneous effect of wear and corrosion. When TiAlN layer was added on top of WC-NiBSi/steel coating, no galvanic coupling was seen under tribocorrosion tests at OCP, but strong galvanic cells formed between TiAlN and WC-NiBSi under potentiostatic polarization where external potential was applied which resulted in a huge material loss from the TiAlN/WC-NiBSi/steel duplex coating. However, TiAlN/TiC-SS/steel exhibited better tribocorrosion results without forming any galvanic couples. In this study, TiC-SS/steel by PTA technique stands out to be the best coating for tribocorrosion applications.

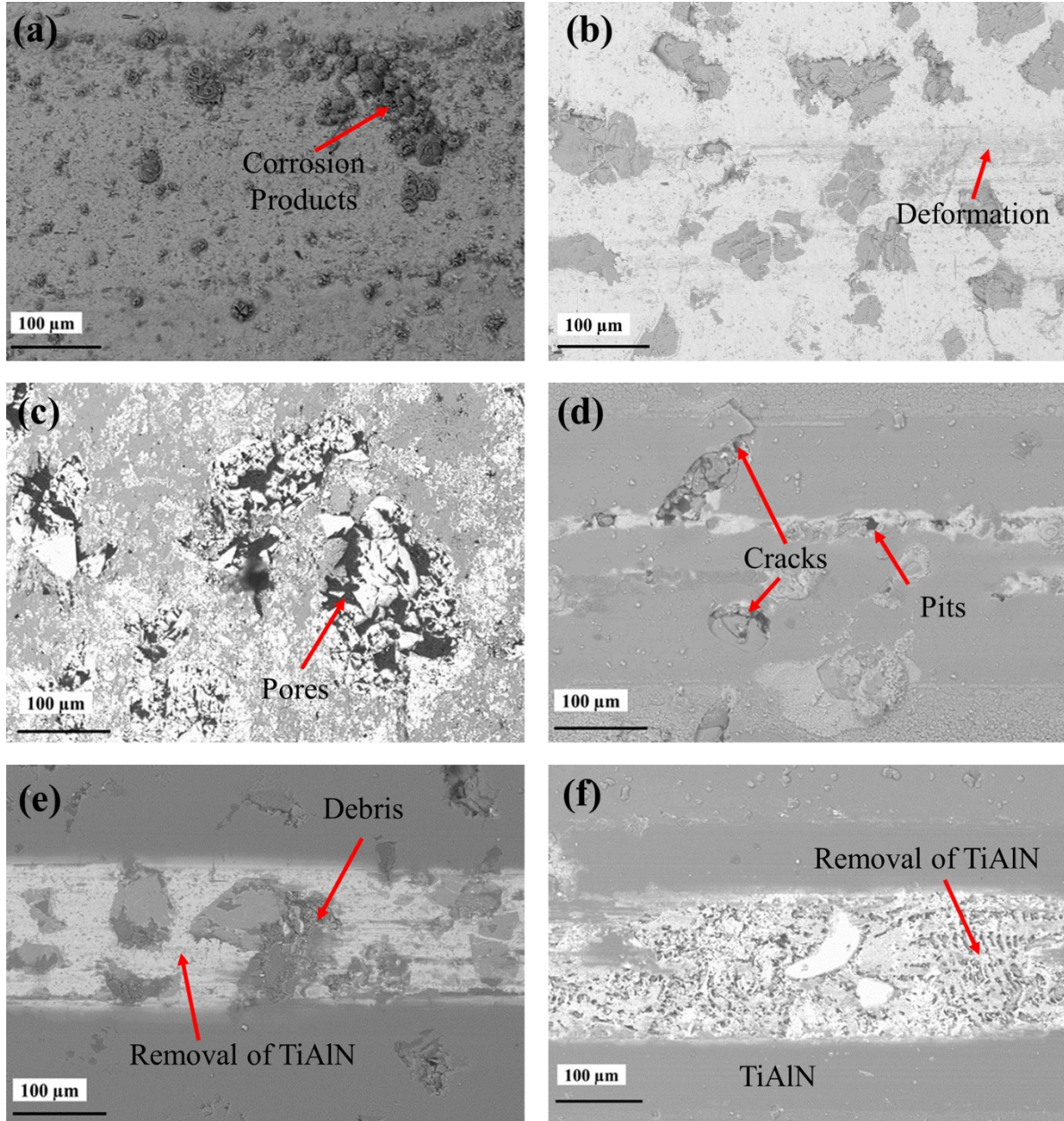


Fig. 44. SEM micrographs for tribocorrosion under potentiostatic polarization at 2N, 2000 cycles load, and 3.5 wt.% NaCl: (a) steel, (b) TiC-SS/steel coating, (c) WC-NiBSi/steel coating, (d) TiAlN/steel coating, (e) TiAlN/TiC-SS/steel duplex coating, and (f) TiAlN/WC-NiBSi/steel coating.

5 Conclusions

In conclusion, the material deterioration caused by tribocorrosion, which is a combined effect of wear and corrosion, has a significant impact on production and the economy in a variety of industrial sectors. An innovative noble duplex coatings system has been designed and developed in this study to solve tribocorrosion concerns in industries. The main objective of this research is to improve tribological, corrosion, and tribocorrosion characteristics using a duplex coating system. Thin-on-thick TiAlN/TiC-SS and TiAlN/WC-NiBSi duplex coatings on steel were fabricated using two distinct deposition processes, plasma transferred arc (PTA) for the thick layer (TiC-SS/steel and WC-NiBSi/steel coatings; thickness ~ 3 mm) and physical vapor deposition (PVD) for the thin layer (TiAlN layer; thickness ~ 2 μm). The prepared duplex coatings were used to conduct wear tests in corrosion environments and then the tribocorrosion properties were evaluated and compared with the results of substrate and single-layer coatings.

A series of dry sliding tests were carried out using a ball-on-flat tribo-system with 2N and 5N applied load against alumina to investigate the tribological performance of the single and duplex coatings. At 5N load, the wear rate of PVD-coated TiAlN/steel was very high, and the coefficient of friction was also high (~ 0.9) which is the typical value for TiAlN in dry conditions. The TiAlN coating on ductile steel broke down so quickly—less than 50 cycles under dry sliding and was totally eliminated during the experiments at 1000 cycles per second as evidenced by optical microscope images. The poor wear resistance of TiAlN/steel is because of the brittle nature of nitride coatings. However, the addition of the TiAlN layer greatly improved the wear resistance of TiC-SS/steel and WC-NiBSi/steel when compared with TiAlN/steel, for example decreasing the wear rate from $71.1 \pm 6.33 \times 10^{-6} \text{ mm}^3\text{N}^{-1}\text{m}^{-1}$ for TiAlN/steel to $30.98 \pm 3.24 \times 10^{-6} \text{ mm}^3\text{N}^{-1}\text{m}^{-1}$

for TiAlN/TiC-SS/steel and $20.35 \pm 4.56 \times 10^{-6} \text{ mm}^3\text{N}^{-1}\text{m}^{-1}$ for TiAlN/WC-NiBSi/steel, respectively. This is because of the high load-bearing capacity of steel as the H , H/E^* , and H^3/E^{*2} values are significantly higher for coatings than steel. As seen from the optical images, partial or complete delamination for TiAlN/TiC-SS/steel duplex coating and no delamination for TiAlN/WC-NiBSi/steel at 1000 cycles/s; however, when the sliding cycles increased the TiAlN was removed completely for WC-NiBSi/steel as well. Nonetheless, the single-layer coatings showed a very low wear rate for all the sliding cycles. Moreover, WC-NiBSi/steel coating exhibited an exceptionally low wear rate, which may be because of the uniformly distributed WC hard particles inclusion into the NiBSi matrix.

At 2N load, no substantial influence of the intermediate layer was observed. The wear rates for TiAlN/steel, TiAlN/TiC-SS/steel, and TiAlN/WC-NiBSi/steel were comparable which may be due to the stress field generated at low load was confined only in the top TiAlN coatings having limited influence from the intermediate layer. Although TiAlN showed the highest hardness, literature explained that the harder nitride coating on ductile substrate exhibited brittle nature. Single-layer of TiC-SS/steel and WC-NiBSi/steel showed very good performance under sliding wear where WC-NiBSi exhibited superior wear resistance compared to all coatings utilized in this study.

Electrochemical measurements including open circuit potential (OCP), electrochemical impedance spectroscopy (EIS), and potentiodynamic polarization were performed under 3.5 wt.% aqueous NaCl solution. The corrosion performance of duplex TiAlN/TiC-SS/steel and TiAlN/WC-NiBSi/steel coatings were compared with the single TiAlN/steel, TiAlN/TiC-SS/steel, and WC-NiBSi/steel coatings and bare steel substrate. The bare steel cannot show any protection in 3.5 Wt.% NaCl solution as indicated by the decrease in corrosion potential from -0.42 V to -0.72 V

for 1h, a very low polarization resistance, and a very high corrosion current. SEM micrographs showed pits, craters, and corrosion products on the surface of the steel. The addition of a TiAlN layer to steel cannot significantly increase its corrosion resistance with a similar corrosion current (2.4×10^{-6} A for TiAlN and 2.8×10^{-6} A for steel) and slightly higher polarization resistance for TiAlN. Pitting is the characteristic form of corrosion where Cl⁻ ions infiltrate through defects and congregate around the weak points and cause the protective layer to rupture. On the other hand, the thick WC-NiBSi/steel layer also showed relatively poor corrosion resistance because of pores in the microstructure whereas TiC-SS/steel showed the best corrosion performance amongst all coatings with excellent corrosion properties (corrosion potential: -0.04 V, corrosion current: 2×10^{-8} A, polarization resistance: $2123000 \Omega \text{ cm}^2$). The addition of the TiAlN layer on TiC-SS/steel cannot further improve the corrosion resistance but higher corrosion resistance than TiAlN/steel was achieved. It is interesting to note that the addition of a TiAlN layer increased the corrosion resistance of the WC-NiBSi/steel coating because the top layer sealed the pores of the WC-NiBSi coatings.

All tribocorrosion tests were done at 2N and 2000 sliding cycles. A sliding ball-on-flat configuration was immersed in the corrosive medium of 3.5 wt.% NaCl solution for the tribocorrosion studies. This makes it feasible to access both the individual wear and corrosion-related deterioration of material as well as the interaction of the two in the overall degradation of materials. The coating acted as the working electrode in a three-electrode cell electrochemical system. Under OCP conditions, mechanical wear accelerated the corrosion of bare steel. For TiAlN/steel, pores, cracks, delamination, and parallel grooves can be observed after SEM studies. The wear rate was higher and a higher μ value was obtained that indicates no lubrication effect for

TiAlN. The low wear rate of WC-NiBSi/steel indicates mechanical wear has less effect on the corrosion behavior, and the friction coefficient is low due to the lubrication effect under an aqueous solution. Although the wear rate is higher than WC-NiBSi/steel, the addition of the TiAlN layer improved the corrosion behavior of WC-NiBSi coatings. On the other hand, the TiAlN layer on TiC-SS/steel degrades the coating's ability to resist corrosion.

Under potentiostatic polarization where external potential was applied, the corrosion current and wear rate suddenly increased when the TiAlN was removed because of the constant loading and unloading. Because the TiAlN layer was no longer providing protection when the rubbing stopped, the current for TiAlN/steel increased further. While TiC-SS/steel showed an entirely flat line of corrosion current, demonstrating excellent tribocorrosion, the corrosion current for the WC-NiBSi/steel coating increased during the rubbing, indicating poor tribocorrosion of the WC-NiBSi/steel coating. On the other hand, due to the formation of galvanic cells between the TiAlN and WC-NiBSi layers, the duplex coating of TiAlN/WC-NiBSi/steel demonstrated exceptionally poor corrosion resistance when the TiAlN layer was continuously removed by rubbing.

In conclusion, it can be said that the TiC-SS/steel coating showed superior corrosion and tribocorrosion behavior, whereas the WC-NiBSi/steel coating demonstrated outstanding wear resistance. In contrast, for the duplex coatings, the addition of a harder intermediate layer improved the TiAlN/steel coating's brittleness, while the deposition of TiAlN as the top layer increased the WC-NiBSi/steel coating's tribocorrosion resistance for tribocorrosion under OCP but deteriorated under potentiostatic polarization.

6 Future Works and Recommendations

In order to achieve optimal performance of the duplex coatings, the following recommendations can be made:

1. Different PVD coatings should be fabricated and studied, for example TiC or TiSiC.
2. The parameters for the preparation of the coatings should be further optimized to reduce the presence of microdefects in the coatings.
3. The mixing ratio for all the powder blends can be varied to obtain proper material properties for the application in wear, corrosion, and tribocorrosion.
4. The synergistic tribocorrosion interactions occurring on the surface of the coatings need to be fully understood.

7 References

- [1] R. Rebak, Uhlig's Corrosion Handbook, Third Edition, in: 2011: pp. 503–516.
<https://doi.org/10.1002/9780470872864.ch36>.
- [2] Y. Sun, R. Bailey, Improvement in tribocorrosion behavior of 304 stainless steel by surface mechanical attrition treatment, *Surf Coat Technol.* 253 (2014) 284–291.
<https://doi.org/10.1016/J.SURFCOAT.2014.05.057>.
- [3] A. Neville, F. Reza, S. Chiovelli, T. Revega, CORROSION SCIENCE SECTION Assessing Metal Matrix Composites for Corrosion and Erosion-Corrosion Applications in the Oil Sands Industry, 2006.
- [4] J.R. Davis, Surface Engineering for Corrosion and Wear Resistance, ASM International. (2001). <https://doi.org/10.31399/ASM.TB.SECWR.9781627083157>.
- [5] L. Cunha, M. Andritschky, L. Rebouta, R. Silva, Corrosion of TiN, (TiAl)N and CrN hard coatings produced by magnetron sputtering, *Thin Solid Films.* 317 (1998) 351–355.
[https://doi.org/10.1016/S0040-6090\(97\)00624-X](https://doi.org/10.1016/S0040-6090(97)00624-X).
- [6] R.M. Souto, H. Alanyali, Electrochemical characteristics of steel coated with TiN and TiAlN coatings, *Corros Sci.* 42 (2000) 2201–2211. [https://doi.org/10.1016/S0010-938X\(00\)00057-3](https://doi.org/10.1016/S0010-938X(00)00057-3).

- [7] F. Pougoum, J. Qian, L. Martinu, J. Klemberg-Sapieha, Z. Zhou, K.Y. Li, S. Savoie, R. Lacasse, E. Potvin, R. Schulz, Study of corrosion and tribocorrosion of Fe₃Al-based duplex PVD/HVOF coatings against alumina in NaCl solution, *Surf Coat Technol.* 357 (2019) 774–783. <https://doi.org/https://doi.org/10.1016/j.surfcoat.2018.10.060>.
- [8] R. Chetcuti, P.A. Dearnley, A. Mazzonello, J. Buhagiar, B. Mallia, Tribocorrosion response of duplex layered CoCrMoC/CrN and CrN/CoCrMoC coatings on implant grade 316LVM stainless steel, *Surf Coat Technol.* 384 (2020) 125313. <https://doi.org/https://doi.org/10.1016/j.surfcoat.2019.125313>.
- [9] Tribocorrosion - Wikipedia, (n.d.). <https://en.wikipedia.org/wiki/Tribocorrosion> (accessed June 8, 2023).
- [10] Y. Sun, V. Rana, Tribocorrosion behaviour of AISI 304 stainless steel in 0.5 M NaCl solution, *Mater Chem Phys.* 129 (2011) 138–147. <https://doi.org/10.1016/J.MATCHEMPHYS.2011.03.063>.
- [11] M. Khadem, O. V. Penkov, H.K. Yang, D.E. Kim, Tribology of multilayer coatings for wear reduction: A review, *Friction.* 5 (2017) 248–262. <https://doi.org/10.1007/S40544-017-0181-7/METRICS>.
- [12] M.A.M. Ibrahim, S.F. Korablov, M. Yoshimura, Corrosion of stainless steel coated with TiN, (TiAl)N and CrN in aqueous environments, *Corros Sci.* 44 (2002) 815–828. [https://doi.org/10.1016/S0010-938X\(01\)00102-0](https://doi.org/10.1016/S0010-938X(01)00102-0).

- [13] F. Pougoum, J. Qian, M. Laberge, L. Martinu, J. Klemberg-Sapieha, Z. Zhou, K.Y. Li, S. Savoie, R. Schulz, Investigation of Fe₃Al-based PVD/HVOF duplex coatings to protect stainless steel from sliding wear against alumina, *Surf Coat Technol.* 350 (2018) 699–711. <https://doi.org/https://doi.org/10.1016/j.surfcoat.2018.07.070>.
- [14] W.M. Zhao, Y. Wang, L.X. Dong, K.Y. Wu, J. Xue, Corrosion mechanism of NiCrBSi coatings deposited by HVOF, *Surf Coat Technol.* 190 (2005) 293–298. <https://doi.org/10.1016/J.SURFCOAT.2004.04.057>.
- [15] H. Kovacı, Y.B. Bozkurt, A.F. Yetim, Baran, A. Çelik, Corrosion and tribocorrosion properties of duplex surface treatments consisting of plasma nitriding and DLC coating, *Tribol Int.* 156 (2021). <https://doi.org/10.1016/J.TRIBOINT.2020.106823>.
- [16] Y. Zhang, F. Chen, Y. Zhang, M. Liu, Y. Pang, C. Du, Enhanced corrosion and tribocorrosion properties of duplex TiN-MAO coating prepared on TC17 alloys, *Surf Coat Technol.* 444 (2022) 128662. <https://doi.org/10.1016/J.SURFCOAT.2022.128662>.
- [17] Y. Sun, P.A. Dearnley, Tribocorrosion Behavior of Duplex S/Cr(N) and S/Cr(C) Coatings on CoCrMo Alloy in 0.89 % NaCl Solution, *J Bio Tribocorros.* 1 (2015). <https://doi.org/10.1007/S40735-014-0002-8>.
- [18] D.H. Kang, H.W. Lee, Study of the correlation between pitting corrosion and the component ratio of the dual phase in duplex stainless steel welds, *Corros Sci.* 74 (2013) 396–407. <https://doi.org/10.1016/J.CORSCI.2013.04.033>.

- [19] S.K. Saha, Y.J. Park, J.W. Kim, S.O. Cho, Self-organized honeycomb-like nanoporous oxide layer for corrosion protection of type 304 stainless steel in an artificial seawater medium, *J Mol Liq.* 296 (2019). <https://doi.org/10.1016/J.MOLLIQ.2019.111823>.
- [20] Y. Wang, G. Cheng, W. Wu, Q. Qiao, Y. Li, X. Li, Effect of pH and chloride on the micro-mechanism of pitting corrosion for high strength pipeline steel in aerated NaCl solutions, *Appl Surf Sci.* 349 (2015) 746–756. <https://doi.org/10.1016/J.APSUSC.2015.05.053>.
- [21] Q. Chen, Y. Cao, Z. Xie, T. Chen, Y. Wan, H. Wang, X. Gao, Y. Chen, Y. Zhou, Y. Guo, Tribocorrosion behaviors of CrN coating in 3.5 wt% NaCl solution, *Thin Solid Films.* 622 (2017) 41–47. <https://doi.org/10.1016/J.TSF.2016.12.023>.
- [22] J. Martin, K. Akoda, V. Ntomprougkidis, O. Ferry, A. Maizeray, A. Bastien, P. Brenot, G. Ezo'o, G. Henrion, Duplex surface treatment of metallic alloys combining cold-spray and plasma electrolytic oxidation technologies, *Surf Coat Technol.* 392 (2020) 125756. <https://doi.org/10.1016/J.SURFCOAT.2020.125756>.
- [23] W. Tillmann, L. Hagen, D. Stangier, M. Krabiell, P. Schröder, J. Tiller, C. Krumm, C. Sternemann, M. Paulus, M. Elbers, Influence of etching-pretreatment on nano-grained WC-Co surfaces and properties of PVD/HVOF duplex coatings, *Surf Coat Technol.* 374 (2019) 32–43. <https://doi.org/10.1016/J.SURFCOAT.2019.05.054>.
- [24] F. Sourani, K. Raeissi, M.H. Enayati, P.K. Chu, H.R. SalimiJazi, Mechanical, corrosion, and tribocorrosion behavior of biomedical ZrO₂ ceramic coatings prepared by thermal

- oxidation, *J Mater Sci.* 58 (2023) 4115–4136. <https://doi.org/10.1007/S10853-023-08211-1/FIGURES/16>.
- [25] A.Z. Ait Djafer, N. Saoula, N. Madaoui, A. Zerizer, Deposition and characterization of titanium carbide thin films by magnetron sputtering using Ti and TiC targets, *Appl Surf Sci.* 312 (2014) 57–62. <https://doi.org/10.1016/J.APSUSC.2014.05.084>.
- [26] M. Yasir, C. Zhang, W. Wang, P. Xu, L. Liu, Wear behaviors of Fe-based amorphous composite coatings reinforced by Al₂O₃ particles in air and in NaCl solution, *Mater Des.* 88 (2015) 207–213. <https://doi.org/10.1016/J.MATDES.2015.08.142>.
- [27] B. Huang, C. Zhang, G. Zhang, H. Liao, Wear and corrosion resistant performance of thermal-sprayed Fe-based amorphous coatings: A review, *Surf Coat Technol.* 377 (2019) 124896. <https://doi.org/10.1016/J.SURFCOAT.2019.124896>.
- [28] N. Ahledel, R. Schulz, M. Gariepy, H. Hermawan, H. Alamdari, Electrochemical corrosion behavior of Fe₃Al/TiC and Fe₃Al-Cr/TiC coatings prepared by HVOF in nacl solution, *Metals (Basel).* 9 (2019). <https://doi.org/10.3390/MET9040437>.
- [29] Y. Chen, H.M. Wang, Microstructure and wear resistance of laser clad TiC reinforced FeAl intermetallic matrix composite coatings, *Surf Coat Technol.* 168 (2003) 30–36. [https://doi.org/10.1016/S0257-8972\(02\)00881-2](https://doi.org/10.1016/S0257-8972(02)00881-2).
- [30] A. Rokanopoulou, G.D. Papadimitriou, Titanium carbide/duplex stainless steel (DSS) metal matrix composite coatings prepared by the plasma transferred arc (PTA) technique:

- Microstructure and wear properties, *J Coat Technol Res.* 8 (2011) 427–437.
<https://doi.org/10.1007/S11998-010-9283-0/FIGURES/11>.
- [31] Y.F. Liu, J.S. Mu, X.Y. Xu, S.Z. Yang, Microstructure and dry-sliding wear properties of TiC-reinforced composite coating prepared by plasma-transferred arc weld-surfacing process, *Materials Science and Engineering A.* 458 (2007) 366–370.
<https://doi.org/10.1016/j.msea.2006.12.086>.
- [32] L. Bourithis, A. Milonas, G.D. Papadimitriou, Plasma transferred arc surface alloying of a construction steel to produce a metal matrix composite tool steel with TiC as reinforcing particles, *Surf Coat Technol.* 165 (2003) 286–295. [https://doi.org/10.1016/S0257-8972\(02\)00744-2](https://doi.org/10.1016/S0257-8972(02)00744-2).
- [33] H. Wang, H. Lu, X. Song, X. Yan, X. Liu, Z. Nie, Corrosion resistance enhancement of WC cermet coating by carbides alloying, *Corros Sci.* 147 (2019) 372–383.
<https://doi.org/10.1016/J.CORSCI.2018.11.028>.
- [34] P. Pereira, A.M.F. Rocha, J. Sacramento, F.J. Oliveira, A.M.R. Senos, L.F. Malheiros, A.C. Bastos, Corrosion resistance of WC hardmetals with different Co and Ni-based binders, *Int J Refract Metals Hard Mater.* 104 (2022) 105799.
<https://doi.org/10.1016/J.IJRMHM.2022.105799>.
- [35] K. Shahzad, A.B. Radwan, O. Fayyaz, R.A. Shakoor, M. Uzma, M.A. Umer, M.N. Baig, A. Raza, Effect of concentration of TiC on the properties of pulse electrodeposited Ni–P–TiC

- nanocomposite coatings, *Ceram Int.* 47 (2021) 19123–19133.
<https://doi.org/10.1016/J.CERAMINT.2021.03.259>.
- [36] C. Navas, R. Colaço, J. de Damborenea, R. Vilar, Abrasive wear behaviour of laser clad and flame sprayed-melted NiCrBSi coatings, *Surf Coat Technol.* 200 (2006) 6854–6862.
<https://doi.org/10.1016/J.SURFCOAT.2005.10.032>.
- [37] P. Niranatlumpong, H. Koiprasert, Phase transformation of NiCrBSi–WC and NiBSi–WC arc sprayed coatings, *Surf Coat Technol.* 206 (2011) 440–445.
<https://doi.org/10.1016/J.SURFCOAT.2011.07.057>.
- [38] P. Sheppard, H. Koiprasert, Effect of W dissolution in NiCrBSi–WC and NiBSi–WC arc sprayed coatings on wear behaviors, *Wear.* 317 (2014) 194–200.
<https://doi.org/10.1016/J.WEAR.2014.06.008>.
- [39] T. Haque, A. Morina, A. Neville, R. Kapadia, S. Arrowsmith, Effect of oil additives on the durability of hydrogenated DLC coating under boundary lubrication conditions, *Wear.* 266 (2009) 147–157. <https://doi.org/10.1016/J.WEAR.2008.06.011>.
- [40] M. Azzi, J.E. Klemberg-Sapieha, Effect of microstructure on the corrosion behavior of TiN coatings, in: *Adv Mat Res*, 2012: pp. 1911–1916.
<https://doi.org/10.4028/www.scientific.net/AMR.415-417.1911>.

- [41] M. Zhang, Y. Cheng, L. Xin, J. Su, Y. Li, S. Zhu, F. Wang, Cyclic oxidation behaviour of Ti/TiAlN composite multilayer coatings deposited on titanium alloy, *Corros Sci.* 166 (2020) 108476. <https://doi.org/10.1016/J.CORSCI.2020.108476>.
- [42] M.M. Khrushchov, Principles of abrasive wear, *Wear.* 28 (1974) 69–88. [https://doi.org/10.1016/0043-1648\(74\)90102-1](https://doi.org/10.1016/0043-1648(74)90102-1).
- [43] F. Sun, H. Xu, A review of biomimetic research for erosion wear resistance, *Biodes Manuf.* 3 (2020) 331–347. <https://doi.org/10.1007/s42242-020-00079-3>.
- [44] E.F. Finkin, Adhesive wear: a general review of the state of experimental knowledge and theory, (n.d.).
- [45] M.X. Wei, K.M. Chen, S.Q. Wang, X.H. Cui, Analysis for wear behaviors of oxidative wear, *Tribol Lett.* 42 (2011) 1–7. <https://doi.org/10.1007/s11249-010-9741-y>.
- [46] S.H. Teoh, Fatigue of biomaterials: a review, *Int J Fatigue.* 22 (2000) 825–837. [https://doi.org/10.1016/S0142-1123\(00\)00052-9](https://doi.org/10.1016/S0142-1123(00)00052-9).
- [47] Z. Khulief, Tribological, Electrochemical, and Tribocorrosion Behaviour of New Titanium Biomedical Alloys, (2018).
- [48] J. Rituerto Sin, Investigation of the corrosion and tribocorrosion behaviour of metallic biomaterials, (2015).

- [49] W.S. Tait, Controlling corrosion of chemical processing equipment, Handbook of Environmental Degradation Of Materials: Third Edition. (2018) 583–600. <https://doi.org/10.1016/B978-0-323-52472-8.00028-9>.
- [50] G.S. Frankel, Pitting Corrosion of Metals: A Review of the Critical Factors, J Electrochem Soc. 145 (1998) 2186–2198. <https://doi.org/10.1149/1.1838615/XML>.
- [51] I.L. ROSENFELD, I.K. MARSHAKOV, Mechanism of Crevice Corrosion, Corrosion. 20 (1964) 115t–125t. <https://doi.org/10.5006/0010-9312-20.4.115T>.
- [52] C. Vargel, Fretting corrosion, Corrosion of Aluminium. (2020) 273–278. <https://doi.org/10.1016/B978-0-08-099925-8.00021-1>.
- [53] D. Li, Microstructure and corrosion and tribo-corrosion behaviors of Si-based and Ti-based aerospace coatings produced by PECVD, (2010). <https://escholarship.mcgill.ca/concern/theses/3f4625866?locale=en> (accessed June 11, 2023).
- [54] R.J.K. Wood, Tribo-corrosion of coatings: A review, J Phys D Appl Phys. 40 (2007) 5502–5521. <https://doi.org/10.1088/0022-3727/40/18/S10>.
- [55] D. Thierry, A. Nazarov, D. Persson, Mechanical and chemical coupling in tribocorrosion: In situ and ex situ characterization techniques, Mechanical and Electro-Chemical Interactions under Tribocorrosion: From Measurements to Modelling for Building a

- Relevant Monitoring Approach. (2021) 29–66. <https://doi.org/10.1016/B978-0-12-823765-6.00003-1>.
- [56] S. Hassani, J.E. Klemberg-Sapieha, L. Martinu, Mechanical, tribological and erosion behaviour of super-elastic hard Ti-Si-C coatings prepared by PECVD, *Surf Coat Technol.* 205 (2010) 1426–1430. <https://doi.org/10.1016/J.SURFCOAT.2010.07.098>.
- [57] M. Azzi, M. Benkahoul, J.E. Klemberg-Sapieha, L. Martinu, Corrosion and mechanical properties of duplex-treated 301 stainless steel, *Surf Coat Technol.* 205 (2010) 1557–1563. <https://doi.org/10.1016/J.SURFCOAT.2010.08.155>.
- [58] P. Jedrzejowski, J.E. Klemberg-Sapieha, L. Martinu, Relationship between the mechanical properties and the microstructure of nanocomposite TiN/SiN_{1.3} coatings prepared by low temperature plasma enhanced chemical vapor deposition, *Thin Solid Films.* 426 (2003) 150–159. [https://doi.org/10.1016/S0040-6090\(03\)00028-2](https://doi.org/10.1016/S0040-6090(03)00028-2).
- [59] S. Islak, C. Özorak, Ö. Küçük, M. Akkaş, C.T. Sezgin, Microstructure and Hardness Properties of high velocity oxygen fuel (HVOF) Sprayed WCCo-SiC Coatings, (2015).
- [60] L. Łatka, P. Biskup, Development in PTA Surface Modifications – A Review, *Advances in Materials Science.* 20 (2020) 39–53. <https://doi.org/10.2478/ADMS-2020-0009>.
- [61] L. Baiamonte, M. Tului, C. Bartuli, D. Marini, A. Marino, F. Menchetti, R. Pileggi, G. Pulci, F. Marra, Tribological and high-temperature mechanical characterization of cold sprayed

- and PTA-deposited Stellite coatings, *Surf Coat Technol.* 371 (2019) 322–332.
<https://doi.org/10.1016/J.SURFCOAT.2019.04.032>.
- [62] Q.Z. Cao, L. Fan, H.Y. Chen, Y.R. Xu, L.H. Dong, Corrosion behavior of WC-Co coating by plasma transferred arc on EH40 steel in low-temperature, *High Temperature Materials and Processes.* 41 (2022) 191–205. <https://doi.org/10.1515/HTMP-2022-0010/MACHINEREADABLECITATION/ENDNOTE>.
- [63] E.J. Herrera-Jimenez, A. Raveh, T. Schmitt, E. Bousser, J.E. Klemberg-Sapieha, L. Martinu, Solid solution hardening in nanolaminate ZrN-TiN coatings with enhanced wear resistance, *Thin Solid Films.* 688 (2019). <https://doi.org/10.1016/J.TSF.2019.137431>.
- [64] Ohring, M. (1992) *The Materials Science of Thin Films.* Academic Press, New Jersey. -
References - Scientific Research Publishing, (n.d).
<https://scirp.org/reference/referencespapers.aspx?referenceid=1369254> (accessed July 17, 2023).
- [65] A. Baptista, F.J.G. Silva, J. Porteiro, J.L. Míguez, G. Pinto, L. Fernandes, On the Physical Vapour Deposition (PVD): Evolution of Magnetron Sputtering Processes for Industrial Applications, in: *Procedia Manuf*, Elsevier B.V., 2018: pp. 746–757.
<https://doi.org/10.1016/j.promfg.2018.10.125>.

- [66] W.C. Oliver, G.M. Pharr, An improved technique for determining hardness and elastic modulus using load and displacement sensing indentation experiments, *J Mater Res.* 7 (1992) 1564–1583. <https://doi.org/10.1557/JMR.1992.1564>.
- [67] F. Pougoum, L. Martinu, J.E. Klemberg-Sapieha, S. Savoie, R. Schulz, Wear properties of Fe₃Al-based HVOF coatings strengthened with in-situ precipitated nitride and boride particles, *Surf Coat Technol.* 307 (2016) 109–117. <https://doi.org/10.1016/J.SURFCOAT.2016.08.049>.
- [68] F. Pougoum, T. Schmitt, L. Martinu, J.E. Klemberg-Sapieha, S. Savoie, R. Schulz, Wear behavior of Fe₃Al-TiN-TiB₂ HVOF coatings: A comparative study between in situ and ex situ powder processing routes, *Ceram Int.* 43 (2017) 8040–8050. <https://doi.org/10.1016/J.CERAMINT.2017.03.122>.
- [69] M. Azzi, M. Benkahoul, J.A. Szpunar, J.E. Klemberg-Sapieha, L. Martinu, Tribological properties of CrSiN-coated 301 stainless steel under wet and dry conditions, *Wear.* 267 (2009) 882–889. <https://doi.org/10.1016/j.wear.2009.01.027>.
- [70] S. K C, S. Adhikari, R.L. Jackson, AN INVESTIGATION OF THE FRICTION AND WEAR PROPERTIES OF HIGH OLEIC VEGETABLE-BASED AND MINERAL OILS, *International Journal of Agriculture, Environment and Bioresearch.* 06 (2021) 01–20. <https://doi.org/10.35410/ijaeb.2021.5679>.

- [71] K. Zakowski, M. Narozny, M. Szocinski, K. Darowicki, Influence of water salinity on corrosion risk - The case of the southern Baltic Sea coast, *Environ Monit Assess.* 186 (2014) 4871–4879. <https://doi.org/10.1007/s10661-014-3744-3>.
- [72] Galvanic series - Wikipedia, (n.d.). https://en.wikipedia.org/wiki/Galvanic_series (accessed June 15, 2023).
- [73] Z. Huang, *An Integrated Study of Tribocorrosion in a Duplex Stainless Steel*, (2015). <https://oaktrust.library.tamu.edu/handle/1969.1/156166> (accessed June 15, 2023).
- [74] Marwan. Azzi, Role of synergy between wear and corrosion in degradation of materials, (2008). <https://escholarship.mcgill.ca/concern/theses/4f16c606r?locale=en> (accessed June 15, 2023).
- [75] M. Azzi, M. Paquette, J.A. Szpunar, J.E. Klemberg-Sapieha, L. Martinu, Tribocorrosion behaviour of DLC-coated 316L stainless steel, *Wear.* 267 (2009) 860–866. <https://doi.org/10.1016/j.wear.2009.02.006>.
- [76] S. Guruvenket, M. Azzi, D. Li, J.A. Szpunar, L. Martinu, J.E. Klemberg-Sapieha, Structural, mechanical, tribological, and corrosion properties of a-SiC:H coatings prepared by PECVD, *Surf Coat Technol.* 204 (2010) 3358–3365. <https://doi.org/10.1016/j.surfcoat.2010.03.031>.
- [77] S. Deshpande, A. Kulkarni, S. Sampath, H. Herman, Application of image analysis for characterization of porosity in thermal spray coatings and correlation with small angle

- neutron scattering, *Surf Coat Technol.* 187 (2004) 6–16.
<https://doi.org/10.1016/J.SURFCOAT.2004.01.032>.
- [78] Y.X. Ou, H.Q. Wang, B. Liao, M.K. Lei, X.P. Ouyang, Tribological behaviors in air and seawater of CrN/TiN superlattice coatings irradiated by high-intensity pulsed ion beam, *Ceram Int.* 45 (2019) 24405–24412. <https://doi.org/10.1016/J.CERAMINT.2019.08.162>.
- [79] Y.X. Ou, H. Chen, Z.Y. Li, J. Lin, W. Pan, M.K. Lei, Microstructure and tribological behavior of TiAlSiN coatings deposited by deep oscillation magnetron sputtering, *Journal of the American Ceramic Society.* 101 (2018) 5166–5176.
<https://doi.org/10.1111/JACE.15769>.
- [80] B.D. Beake, The influence of the H/E ratio on wear resistance of coating systems – Insights from small-scale testing, *Surf Coat Technol.* 442 (2022) 128272.
<https://doi.org/10.1016/J.SURFCOAT.2022.128272>.
- [81] J. Musil, Hard nanocomposite coatings: Thermal stability, oxidation resistance and toughness, *Surf Coat Technol.* 207 (2012) 50–65.
<https://doi.org/10.1016/J.SURFCOAT.2012.05.073>.
- [82] E. Bousser, M. Benkahoul, L. Martinu, J.E. Klemberg-Sapieha, Effect of microstructure on the erosion resistance of Cr–Si–N coatings, *Surf Coat Technol.* 203 (2008) 776–780.
<https://doi.org/10.1016/J.SURFCOAT.2008.08.012>.

- [83] S. Hassani, M. Bielawski, W. Beres, L. Martinu, M. Balazinski, J.E. Klemberg-Sapieha, Predictive tools for the design of erosion resistant coatings, *Surf Coat Technol.* 203 (2008) 204–210. <https://doi.org/10.1016/j.surfcoat.2008.08.050>.
- [84] D. Li, S. Guruvenket, S. Hassani, E. Bousser, M. Azzi, J.A. Szpunar, J.E. Klemberg-Sapieha, Effect of Cr interlayer on the adhesion and corrosion enhancement of nanocomposite TiN-based coatings deposited on stainless steel 410, *Thin Solid Films.* 519 (2011) 3128–3134. <https://doi.org/10.1016/J.TSF.2010.12.020>.
- [85] H.J. Noh, H. Jang, Friction instability induced by iron and iron oxides on friction material surface, *Wear.* 400–401 (2018) 93–99. <https://doi.org/10.1016/J.WEAR.2017.12.025>.
- [86] F. Ilie, G. Ipate, F.C. Manaila, Tribological Properties Study of Solid Lubrication with TiO₂ Powder Particles, *Materials.* 15 (2022). <https://doi.org/10.3390/ma15207145>.
- [87] M.H. Sulaiman, R.N. Farahana, K. Bienk, C. V. Nielsen, N. Bay, Effects of DLC/TiAlN-coated die on friction and wear in sheet-metal forming under dry and oil-lubricated conditions: Experimental and numerical studies, *Wear.* 438–439 (2019) 203040. <https://doi.org/10.1016/J.WEAR.2019.203040>.
- [88] T. Zapletal, P. Sperka, I. Krupka, M. Hartl, The effect of surface roughness on friction and film thickness in transition from EHL to mixed lubrication, *Tribol Int.* 128 (2018) 356–364. <https://doi.org/10.1016/J.TRIBOINT.2018.07.047>.

- [89] Y. Zhou, H. Zhu, W. Zhang, X. Zuo, Y. Li, J. Yang, Influence of surface roughness on the friction property of textured surface, *Advances in Mechanical Engineering*. 7 (2015) 1–9. https://doi.org/10.1177/1687814014568500/ASSET/IMAGES/LARGE/10.1177_1687814014568500-FIG6.JPEG.
- [90] L. Du, C. Huang, W. Zhang, T. Li, W. Liu, Preparation and wear performance of NiCr/Cr₃C₂–NiCr/hBN plasma sprayed composite coating, *Surf Coat Technol*. 205 (2011) 3722–3728. <https://doi.org/10.1016/J.SURFCOAT.2011.01.031>.
- [91] O. Fayyaz, A. Khan, R.A. Shakoor, A. Hasan, M.M. Yusuf, M.F. Montemor, S. Rasul, K. Khan, M.R.I. Faruque, P.C. Okonkwo, Enhancement of mechanical and corrosion resistance properties of electrodeposited Ni-P-TiC composite coatings, *Sci Rep*. 11 (2021). <https://doi.org/10.1038/S41598-021-84716-6>.
- [92] F. Borgioli, E. Galvanetto, T. Bacci, Corrosion behaviour of low temperature nitrided nickel-free, AISI 200 and AISI 300 series austenitic stainless steels in NaCl solution, *Corros Sci*. 136 (2018) 352–365. <https://doi.org/10.1016/J.CORSCI.2018.03.026>.
- [93] S. Bull, *Materials Degradation and its Control by Surface Engineering*; by A.W. Batchelor, L.N. Lam and M. Chandrasekaran; Imperial College Press, 1999, *Tribol Int*. 33 (2000) 144–146. [https://doi.org/https://doi.org/10.1016/S0301-679X\(00\)00017-7](https://doi.org/https://doi.org/10.1016/S0301-679X(00)00017-7).

- [94] J. Nie, F. Wang, Y. Chen, Q. Mao, H. Yang, Z. Song, X. Liu, Y. Zhao, Microstructure and corrosion behavior of Al-TiB₂/TiC composites processed by hot rolling, *Results Phys.* 14 (2019). <https://doi.org/10.1016/j.rinp.2019.102471>.
- [95] Z. Li, C. Li, Z. Gao, Y. Liu, X. Liu, Q. Guo, L. Yu, H. Li, Corrosion behavior of Al-Mg₂Si alloys with/without addition of Al-P master alloy, *Mater Charact.* 110 (2015) 170–174. <https://doi.org/10.1016/j.matchar.2015.10.028>.
- [96] P.A. Dearnley, G. Aldrich-Smith, Corrosion–wear mechanisms of hard coated austenitic 316L stainless steels, *Wear.* 256 (2004) 491–499. [https://doi.org/10.1016/S0043-1648\(03\)00559-3](https://doi.org/10.1016/S0043-1648(03)00559-3).
- [97] RM Pilliar, *Biomedical materials*, Springer US, 2009. <https://doi.org/10.1007/978-0-387-84872-3>.

Appendix A – SEM Images and EDS analysis of Coatings

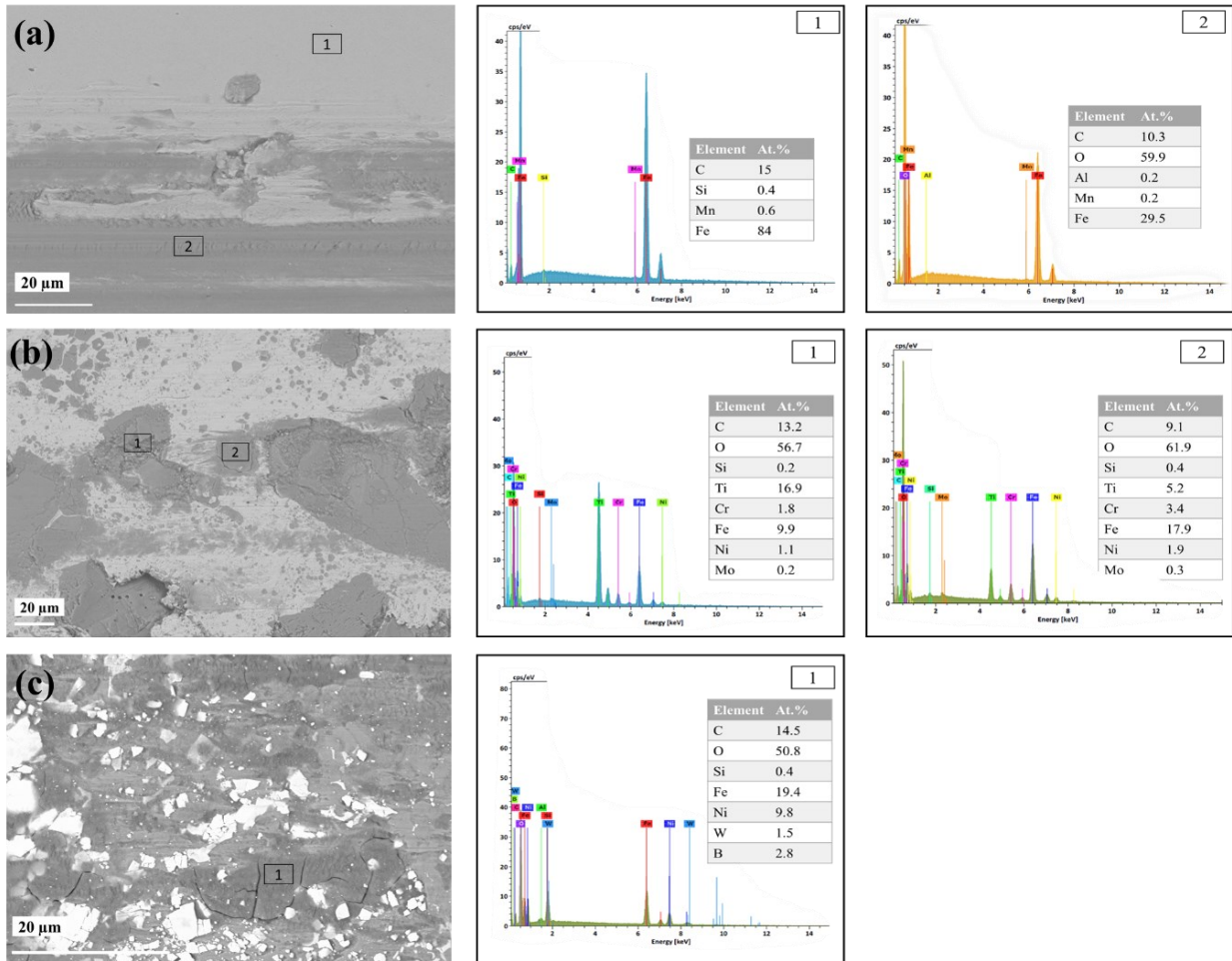


Fig. A1. SEM micrographs for (a) steel, (b) TiC-SS/steel coatings, and (c) WC-NiBSi/steel coating under dry sliding tests at 2N and 1000 sliding cycles.

Appendix B – Wear, corrosion, and tribocorrosion behavior

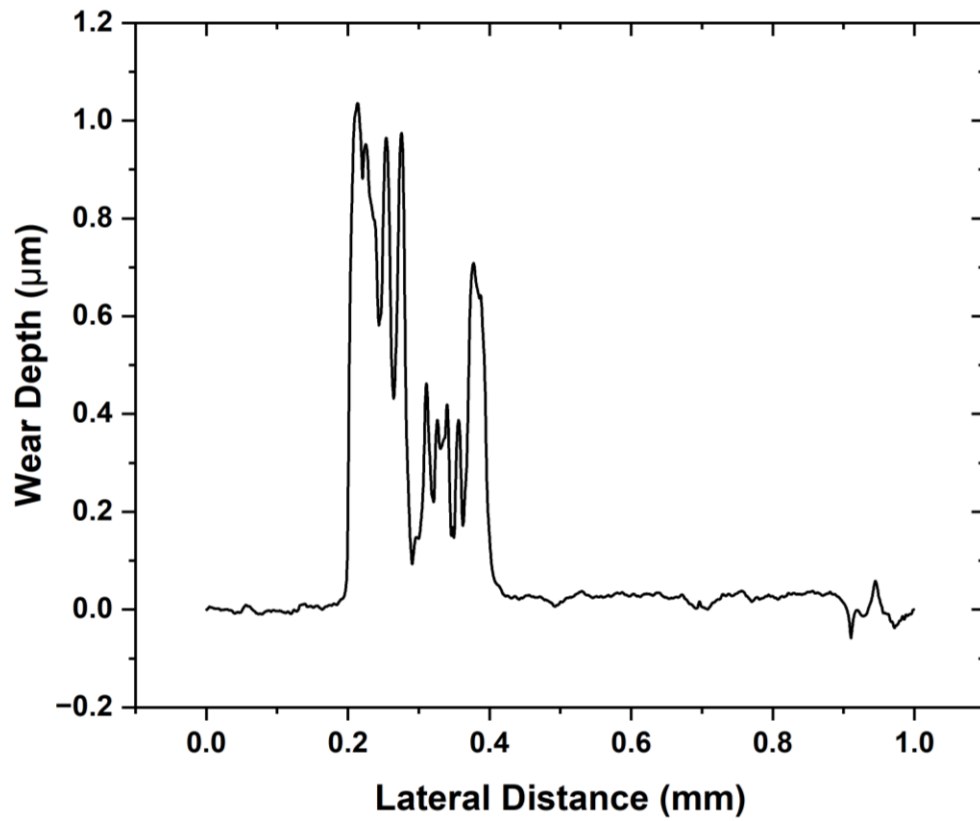


Fig. B1. Line profile from profilometer for showing positive wear depth or positive volume region for steel under the dry sliding wear tests conditions against alumina at 5 N load and 1000 sliding cycles.